Phase Coherent Transport Phenomena in HgTe Quantum Well Structures

Dissertation zur Erlangung des
naturwissenschaftlichen Doktorgrades der
Bayerischen Julius-Maximilians-Universität
Würzburg

vorgelegt von

VOLKER DAUMER

aus Würzburg

Würzburg

2005

Eingereicht am: 29.06.2005

bei der Fakultät für Physik und Astronomie

1. Gutachter: Priv. Doz. Dr. H. Buhmann
2. Gutachter: Prof. Dr. L.W. Molenkamp

der Dissertation.

1. Prüfer: Priv. Doz. Dr. H. Buhmann
2. Prüfer: Prof. Dr. L.W. Molenkamp
3. Prüfer: Prof. Dr. R. Oppermann

im Promotionskolloquium

Tag des Promotionskolloquiums: 10.10.2005

Doktorurkunde ausgehändigt am:

Contents

Introduction **5**

1 Basic Transport Theory **9**

1.1 Classical Transport Theory 10

1.2 Semiclassical Transport Theory and Quantum Transport 11

1.3 Analysis of Shubnikov-de Haas Oscillations 15

1.4 Quantum Hall Effect 15

1.5 Ballistic Transport 18

1.6 Monte-Carlo Simulations 21

1.7 Summary 22

2 Phase Coherence **25**

2.1 Phase in Physics 26

2.2 Aharonov-Bohm Effect 26

2.3 Aharonov-Casher Effect 27

2.4 Berry Phase 28

2.5 Spin-orbit Berry Phase 29

2.6 Aharonov-Anandan Phase 30

2.7 Universal Conductance Fluctuations 31

2.8 Weak Localisation and Weak Anti-Localisation 32

2.9 Summary 32

3 Hg Based Heterostructures 35

3.1 Band Structure of $Hg_{1-x}Mn_xTe$ Quantum Wells 36

3.2 Giant Zeeman Splitting 39

3.3 Antiferromagnetic Temperature and Effective Spin in HgMnTe . . 40

3.4 Bychkov-Rashba Spin-Orbit Splitting 44

3.5 Spin Glass 47

3.6 Summary 50

4 Measurements of Nanostructures 53

4.1 Process Development for Nanostructures on HgTe QWs 54

4.2 Quasi-Ballistic Transport 55

4.3 Transport in Rings 64

4.4 Summary 69

5 Measurements on $Hg_{1-x}Mn_xTe$ Quantum Wells 73

5.1 Interplay of Rashba, Zeeman and Landau Splitting 74

5.2 Filling factor $\nu = 1$ 80

5.3 Phase Transition into Spin-Glass Phase? 85

5.4 Summary 97

Summary and Outlook 99

Zusammenfassung 103

List of Figures 107

Bibliography 109

List of Publications 119

Acknowledgements 121

Introduction

Microelectronic based on semiconductors is present in almost all parts of life. Most of the integrated circuits are realised with the element silicon, whereas for optical application compound semiconductors are necessary. In this field, the III-V heterostructures are dominant. Due to the technological problems in the production and microstructuring II-VI semiconductors play a minor role on the market for electronic components. The only exception are infrared photodiodes which are commercially produced on the basis of HgCdTe. Traditionally these diodes are fabricated by means of liquid phase epitaxy. Such photodiodes are commercially available for one of the two atmospheric windows. But this method can not fabricate a double diode which is sensitive in both windows at once because of the impossibility to grow a crystal with two different, sharply separated cadmium contents. Recently several research centres, mainly in the USA, started intense research on the development of such structures by means of molecular beam epitaxy. Also at the chair of experimental physics three at Würzburg University successful studies of the feasibility of such structures were done in the framework of this thesis in cooperation with AEG Infrarot Module company. These studies resulted in a research project granted by the German ministry of defence. Due to nondisclosure reasons these results will not be presented here.

Since the seminal paper of Datta and Das, where they proposed a field effect transistor which is toggled not by the electronic charge but by the electronic spin, a revolutionary new field in the applied semiconductor physics was opened. This field now called spintronics, attracted huge attention in solid state physics and as a consequence fundamental research activities on the behaviour of the electronic spin raised. A mercury based heterostructure is a very good template for such investigations. Asymmetric HgTe quantum wells (QWs) due to their structure inversion asymmetry exhibit a giant spin-orbit splitting, known as Rashba spin-orbit splitting, which is at least four to five times larger as in III-V semiconductors. Furthermore it is possible to incorporate manganese isoelectrically into these crystals and form a diluted magnetic semiconductor (DMS). Such DMS have been, among others in Würzburg, successfully used to demonstrate the injection of spin-polarised carriers into a semiconductor device, which was a milestone in the development of spintronics. A next step is the control over spin coherence of the carriers to maintain spin-polarised transport. Hence, giant spin-orbit splitting and giant Zeeman splitting, which are both tunable in HgMnTe QWs, are important effects and therefore have been studied in the framework of this thesis.

Demonstration of spin coherent transport could be equivalent to the observation of the spin-orbit Berry phase. Hence, this phase recently aroused much attention. Although there exist many theoretical descriptions and proposals for experimental realisation, up until now it has not been directly observed. One major goal of this thesis is the investigation of phase coherence transport, which is the basis for the observation of the spin-orbit Berry phase. Theoretical considerations suggest that HgTe QWs are a good candidate to observe the Berry phase, but many technological problems have to be solved. A nanostructuring technology has to be developed, which overcomes the material specific problems. Furthermore, the successful realisation of nanostructured devices allows a new method of measuring the magnetic ordering of a sample. Usually this is performed by means of magneto-optical or SQUID[1] measurements. However, here the two-dimensional electron gas is used as a sensor of the magnetic ordering.

To present the above mentioned aspects this thesis is organised as follows: At the beginning the relevant transport theory for the experiments is summarised. The next chapter is dedicated to the theory of phase coherent effects. Then particular properties of mercury based heterostructures are presented. Herein, the experiments to deduce sample specific parameters are introduced. The development and the realisation of nanostructures on HgTe QWs are presented in chapter 4. Measurements on these nanostructures are focused on ballistic effects and phase coherence, here. Finally QWs consisting of HgMnTe are investigated. The interplay of Rashba, Zeeman and Landau splitting will be clarified. Phase coherent measurement on micro Hall bars demonstrate the possibility to use the magnetic two-dimensional electron gas as a sensor for the magnetic ordering in the sample. In the last chapter a summary of the results is given and an outlook for further research is presented.

---

[1] **s**uperconducting **q**uantum **i**nterference **d**evice

Chapter 1

Basic Transport Theory

Based on the design and the electronic properties of a sample, magneto-transport can be divided into different transport regimes. In macroscopic or low mobility samples the electronic transport can be described with the classical Drude formula [Dru00a; Dru00b]. When the device dimensions are reduced and the mobility is increased, such that the mean free path becomes the order of the device dimensions, ballistic and coherent phenomena have been observed. The theories of classical, semi-classical and quantum transport can be found in modern standard textbooks of solid state and semiconductor physics such as [AM76; Hel88; See91; Dat95; Dav98]. Moreover, they have been summarised in several Ph.D. thesis, e.g., [Ger97; Zha01; Liu03]. Here, only a short summary of their main aspects will be given. The last two sections of this chapter are an introduction to ballistic transport phenomena and its simulation. An introduction to phase coherent phenomena will be given in chapter 2.

1.1 Classical Transport Theory

In the kinetic theory of gases, the molecules are assumed to be incompressible spheres, which move with constant velocity in a straight line except for short collisions with other molecules or the boundaries. Drude adapted this model in order to describe electronic transport in metals [Dru00a; Dru00b].

Analogous to the theory of an ideal gas he made some simplifying assumptions:

- Between collisions with other electrons or ion cores, the electrons move independently in a straight line with the same velocity, i.e., without interactions. In the presence of an external field they move according to Newton's equations of motion.
- The collisions are instantaneous and velocity is altered abruptly. Scattering happens mainly with the ion cores.
- Irrespective of their velocity or location, the relaxation or collision time τ is defined as the average time between two collisions. The collision probability in an infinitesimal time interval $\mathrm{d}t$ amounts to $\mathrm{d}t/\tau$.
- The thermal equilibrium of the electrons with the environment is reached through these collisions. After several collisions the electron has a randomly oriented velocity with an absolute value according to the local temperature.

In an applied electric field $\vec{E}$, the electrons attain after a short initial period an average drift velocity

$$\vec{v_d} = -\mu \vec{E}, \tag{1.1}$$

where $\mu = (e\tau)/m$ is the mobility and e and m are the electron charge and mass, respectively. According to Ohm's law the current density $\vec{j}$ is

$$\vec{j} = \sigma \vec{E}, \tag{1.2}$$

where σ represents the conductivity tensor. The resistivity ρ, an observable variable in a transport experiment, is the inverse of the conductivity, i.e., $\rho = \sigma^{-1}$. In absence of an external magnetic field, σ is a scalar and can be written as

$$\sigma_0 = en\mu = \frac{ne^2\tau}{m}, \tag{1.3}$$

where n is the electron density. When a magnetic field $\vec{B}$ is applied perpendicular to the current density $\vec{j}$ is applied, i.e., in the z-direction, the Hall effect has to be taken into account and the conductivity tensor can be written as

$$\sigma = \begin{pmatrix} \sigma_{xx} & \pm\sigma_{xy} & 0 \\ \mp\sigma_{xy} & \sigma_{xx} & 0 \\ 0 & 0 & \sigma_0 \end{pmatrix},$$

$$with\ \sigma_{xx} = \frac{\sigma_0}{1+(\mu B)^2} = -\frac{\sigma_{xy}}{\mu B}. \tag{1.4}$$

The upper sign is valid for electrons, the lower one for holes. Hence, the resistivity can be calculated to be:

$$\begin{aligned} \rho_{xx} &= \frac{\sigma_{xx}}{\sigma_{xx}^2+\sigma_{xy}^2} \text{ and } \rho_{xy} = \frac{\sigma_{xy}}{\sigma_{xx}^2+\sigma_{xy}^2} && (1.5) \\ \rho_{xx} &= \rho_0 = \frac{1}{en\mu} = \frac{m}{e^2 n\tau} && (1.6) \\ \rho_{xy} &= R_H \cdot B = \pm\frac{B}{ne}, && (1.7) \end{aligned}$$

where R_H is the Hall coefficient.

1.2 Semiclassical Transport Theory and Quantum Transport

The limitations of the Drude theory are obvious with regard to its inherent simplifying assumptions. For a better description of the electronic transport in a solid state material several improvements have to be made. The Bloch formula [Hel88] introduces the effective mass approximation into the solution of the Schrödinger equation for the wave function of an electron in a periodic lattice potential of a crystal. The effective mass depends on the curvature of the dispersion of the energy band. Therefore, band structure calculations are essential in order to understand magneto-transport measurements (s. sec. 3.1 and ref. [PJ00]).

In contrast to Drude's assumption of uniformity of the electron velocities, the semiclassical transport theory requires, that they obey the Fermi-Dirac distribution f:

$$f = \frac{1}{\exp[(E_k-\mu_F)/(k_B T)]+1} \tag{1.8}$$

The distribution function f also indicates the probability of an electron occupying a band state with energy E_k at temperature T. Here, μ_F is the chemical potential (in the case of $T = 0$ K, μ_F is the Fermi energy) and k_B is the Boltzmann constant. Since the difference between μ_F and the Fermi energy is small at low temperatures, especially for metals, the notation is often used synonymously. Taking the Pauli exclusion principle and the Heisenberg uncertainty relation into account, the density of states (DOS), $D_i(E)$, can be calculated by integrating over the allowed $\vec{k}$ vectors in the energy range between E_i and $E_i + dE$:

$$D_i(E)dE = \frac{2}{V}\int\frac{d\vec{k}}{\Delta\vec{k}}, \tag{1.9}$$

where V is volume of the allowed $\vec{k}$ space and the factor 2 is included because of the twofold spin degeneracy. The integration over the density of states $D_i(E)$ multiplied by the occupation probability $f(E)$ for all possible energies provides the number n of electrons per unit volume in the energy band E_i.

$$n_i(E) = \int_0^\infty D_i(E) f(E) dE \tag{1.10}$$

This equation can be used to calculate the Fermi energy E_F, if one has already obtained the carrier concentration e.g., from a Hall measurement (s. eq. (1.7)). The Fermi surface separates the occupied ($E \leq E_F$) from the unoccupied ($E > E_F$) states in the $\vec{k}$ space.

Due to the complicated scattering processes, with their different origins, the distribution function has to be approximated. Widely used is the relaxation time approximation. Within this approximation, the microscopic scattering processes are described by a macroscopic, energy dependent quantity $\tau(\vec{k})$. For further details the reader is referred to the corresponding section in [Ger97] and the references therein.

If one replaces the charge carrier mass m with the effective mass m^* and the relaxation time τ with $\tau(\vec{k})$, the equations (1.3)-(1.7) remain valid. Thus, the Hall mobility μ_H can be calculated with:

$$\mu_H = |R_H(\vec{B}=0) \cdot \sigma_{xx}(\vec{B}=0)|, \tag{1.11}$$

where $\sigma_{xx}(\vec{B}=0)$ is the zero magnetic field longitudinal conductivity. In a magneto-transport experiment resistances or the corresponding voltages and currents are usually measured. Thus, equation (1.11) has to be transformed using equations (1.3)-(1.7) and the relation $R_{xx} = \rho_{xx}\frac{l}{w}$ for the resistance of a sample with length l and width w. Thus, the Hall mobility is given by

$$\mu_H = |\frac{1}{neR_{xx}(\vec{B}=0)} \cdot \frac{l}{w}|, \tag{1.12}$$

where n is the carrier concentration, that can be derived directly from the Hall coefficient (eq. (1.7)), i.e., the slope of the straight line in a low field R_{xy} vs. B plot.

When the temperature is reduced and the applied magnetic field is increased, new phenomena have to be considered. In a perpendicular magnetic field (z-direction) the electrons are deflected on circular trajectories in the x-y-plane due to the Lorentz force, where they circulate with the cyclotron frequency given by $\omega_c = |\frac{eB}{m^*}|$ and the cyclotron radius[1] by $r_c = \frac{\sqrt{2m^*E}}{|eB|}$. In the above mentioned limit of high magnetic fields and low temperatures[2], when r_c is of the order of the

---

[1] E is the kinetic energy; electron charge e and effective mass m^*, as used before.

[2] Typical values for our samples are $B \geq 1$ T and $T \leq 40$ K

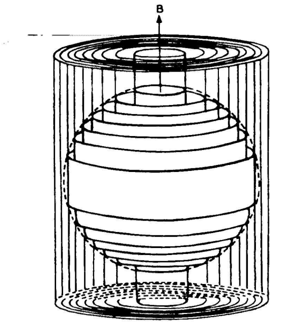

Figure 1.1: Landau quantisation of a spherical surface of constant energy in $\vec{k}$-space into discrete, concentric Landau cylinders oriented parallel to the applied magnetic field (taken from [See91].

de Broglie wave length the electrons are quantised in the Landau levels [Lan30]. In other words, the condition that the cyclotron energy[3] $\hbar\omega_c$ is much larger than the thermal energy k_BT must be fulfilled. A schematic diagram of the concentric Landau cylinders in the 3D case is shown in Figure 1.1. The electron motion in the x-y-plane is quantised, but along the magnetic field direction is not affected. If the motion of the electrons is additionally confined in a quantum well (2DEG) in the z-direction their energy eigenvalues are completely quantised and the energy states condense onto Landau circles, which are the intersection of the Landau cylinders with the x-y-plane. Then the energy eigenvalues are given by

$$E_{i,N} = E_i + \left(N + \frac{1}{2}\right) \cdot \hbar\omega_c, \tag{1.13}$$

where $N = 0, 1, 2, 3, ...$ is the Landau quantum number and the index i indicates the particular energy level. Thus, the density of states $D(E)$ is discrete and can be obtained by summation of the δ-functions for all i and N according to

$$D(E) = \frac{1}{2\pi l_B^2} \cdot \sum_{i,N} \delta(E - E_{i,N}). \tag{1.14}$$

The magnetic length l_B is given by $l_B = \sqrt{\hbar/eB}$. In the case of spin degeneracy the equation above has to be multiplied by a factor of 2.

With increasing magnetic field, the cyclotron energy and consequently the radii of the circles or cylinders become larger and eventually cross the Fermi surface. Hence, the density of state near the surface oscillates, which results, e.g., in oscillations of the longitudinal magneto-resistance, the Shubnikov-de Haas (SdH) effect. The parameter ν, called the filling factor, specifies the number of fully occupied Landau levels, i.e., the number of them lying within the volume enclosed by the Fermi surface. It is defined as

$$\nu = \frac{h}{eB} n, \tag{1.15}$$

---

[3] $\hbar$ is the Planck constant divided by 2π

where n is the total electron density. According to equation (1.14) the filling factor provides the ratio of electrons per flux quantum h/e.

In the presence of a magnetic field the Landau levels are split due to the Zeeman effect. This leads to an additional term in the Hamiltonian for an electron in a QW. Hence, the energy eigenvalues can be calculated using

$$E_{i,N,s} = E_i + \left(N + \frac{1}{2}\right) \cdot \hbar\omega_c + S \cdot g^* \mu_B B, \tag{1.16}$$

where $S = \pm\frac{1}{2}$ is the spin quantum number, g^* the effective g-factor, and μ_B the Bohr magneton. In addition to the Zeeman effect, the level splitting can be enhanced due to the spin-orbit coupling (Rashba [BR84] and Dresselhaus [Dre55] effect, s. sec. 3.4), which leads again to an additional term in the Hamiltonian.

In a real system the Landau levels have not the shape of δ-functions but are broadened. The main reasons for this are the Heisenberg uncertainty relation and especially the different scattering processes. Several approaches have been made to calculate the density of states with a consideration of scattering events. See, for example, the article by Ando *et al.* [AFS82] and the references therein. For an overview of these theories the reader is referred to [Ger97; Liu03].

Apart from low temperature T and high magnetic field B, which ensure a high energy-spacing $\hbar\omega_c$, and low thermal broadening $k_B T$ of the individual Landau levels, the observation of SdH oscillations also require a minimum broadening due to scattering processes, Γ (as shown in Figure 1.2).

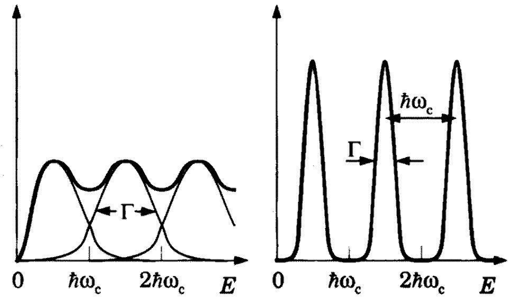

Figure 1.2: When the Landau level broadening is larger than the Landau level separation (left), the SdH effect can not be observed. The density of states (y-axis) between the Landau levels must approach zero and they should not overlap (right).

Evidently, one or more Landau levels must lie within the Fermi sphere due to the already mentioned origin of the SdH oscillations. The analysis of the SdH oscillations is a powerful tool for the characterisation of our samples. By using this technique, characteristic sample parameters could be extracted [GLO+01; ZPJO+01] and the interplay of Rashba, Zeeman and Landau level splitting has been clarified [GBL+04].

1.3 Analysis of Shubnikov-de Haas Oscillations

Under the above mentioned conditions, SdH oscillations could be observed. The expression for the normalised amplitude usually used to extract sample specific parameter is [AH59; RA66; SS91]

$$\frac{\Delta\rho}{\rho_0} = \sum_{R=1}^{\infty} \frac{5}{2}\sqrt{\left(\frac{RP}{2B}\right)} \frac{\beta' T m' \cos(R\pi\nu)}{\sinh(R\beta' T m'/B)} \exp\left(\frac{-R\beta' T_D m'}{B}\right)$$

$$\times \cos\left[2\pi\left(\frac{R}{PB} - \frac{1}{8} - R\gamma\right)\right], \tag{1.17}$$

which takes spin splitting and the non-parabolicity of the bands into consideration. Here $\Delta\rho$ is the longitudinal resistivity without background, ρ_0 the zero field resistivity, $P = \hbar e/E_F m^*$, the period of the SdH oscillations (in T^{-1}), B the transverse magnetic field, $\beta' = 2\pi^2 k_B m_0/\hbar e = 14.707\ \mathrm{TK}^{-1}$ summarises some constants, T the temperature, $m' = m^*/m_0$, the ratio of the effective to the free electron mass, $\nu = \frac{1}{2}m' g^*$, with g^*, the effective g-factor, T_D the Dingle temperature and γ the Onsager phase factor. The first term of the sum ($R = 1$) usually describes the temperature dependence of the amplitude sufficiently. It has to be mentioned, that equation (1.17) was derived originally for the three-dimensional case. Since the oscillations are observed in the two-dimensional (2D) case due to the same reason, the equation is also used for the analysis of the 2D case. A comparison with complex numerical calculations provides the justification for this procedure.

According to Seiler [SS91] the derivations of equation (1.17) provide the sample parameters such as the Fermi energy E_F and the carrier concentration, the effective mass m^*, the Dingle temperature T_D, and the effective g-factor g^*, in case the spin splitting is resolved.

In the SdH oscillations of our samples beating patterns are often observed because of the existence of two closely spaced frequency components with similar amplitudes due to level splitting. The shift of the node position of this beating by variation of temperature and applied gate-voltage is analysed to determine, on one hand, the exchange interaction of the manganese ions with the carriers (s. section 3.3) and, on the other hand, the Rashba and Zeeman effect as described in section 5.1.

1.4 Quantum Hall Effect

More than 20 years after its discovery [vKDP80], the quantum Hall effect (QHE) is still a challenge for theory and experiment. The importance of the research on the QHE can be recognised in the number of papers which have been published on the subject. Up to now about 6100 papers have been published, more than 400 per year since 1995 (INSPEC). A historical overview of the discovery and the first theoretical interpretations has been given by Landwehr [Lan03].

As a consequence of the Landau quantisation the Hall resistivity in two-dimensional (2D) systems is quantised in units of h/e^2:

$$\rho_{xy} = \frac{1}{\nu} \cdot \frac{h}{e^2}, \tag{1.18}$$

where ν is the integer filling factor from equation (1.15). In 2D systems the Hall resistivity is equal to the Hall resistance and thus, the quantum Hall plateaus occur at integer fractions of the von Klitzing constant, $R_K = h/e^2 = 25812.807\ \Omega$. The theoretical description of the QHE is more complex than that of the SdH effect. Solely, the transit of Landau levels through the Fermi sphere with increasing magnetic field can not explain the existence of plateaus with finite width. Hence, in the initial paper [vKDP80] itself the existence of localised states was taken into account. Among others, Aoki and Ando [AA81], as well as, Laughlin [Lau81] put this consideration on a more quantitative basis. Earlier numerical calculations already showed, that around the centre of the Landau levels, delocalised (extended) states exist and that the states in the tails of the DOS at the borders of the Landau levels are localised [Aok77]. Following the review article of Aoki [Aok87], the QHE can be described in terms of a transition between localised and delocalised states and vice versa. In the case that the Fermi energy E_F falls in the range of localised states between two Landau levels, the number of delocalised states below E_F, which are responsible for the Hall voltage, is constant and the Hall resistance shows a plateau. Furthermore, the absence of delocalised states near E_F, which could contribute to a dissipative longitudinal current, leads to a minimum in the longitudinal resistance. If the centre of the next Landau level with delocalised states approaches E_F, the Hall resistance increases and the longitudinal resistance has a maximum.

For a microscopic description of the QHE, Büttiker [Büt88] developed in 1988 the so called edge channel model based on the Landauer-Büttiker (LB) formula [Lan57; Büt86]. The LB formula will be explained more in detail in the next section, due to its relevance in the description of (quasi-)ballistic transport phenomena.

A laterally structured 2DEG (e.g., a Hall bar) has at the sample boundaries an additional confinement potential. In a magnetic field applied perpendicular to the plane of movement, the electrons move in semi-classical cyclotron orbits. Near the sample boundary the circles are truncated and the electrons propagate along the edge in skipping orbits, the edge channels. They develop on both sides of the sample and the electrons propagate in opposite direction for the left and right hand side channels. For every Landau, level below E_F exists one quantised, quasi one-dimensional channel. Thus, in this model the number of edge channels is given by the filling factor ν. With increasing field, the edge channels move to the centre of the sample, are open and form localised cyclotron orbits in the bulk. While this transition, backscattering from one side of the sample to the other is possible due to the spatial vicinity of the states that are otherwise separated. In Figure 1.3 the transition from filling factor $\nu = 3$ to $\nu = 2$ is illustrated. The final situation ($\nu = 2$, not shown in the Figure) looks like the initial one (upper part) with only two edge channels left. This possibility of backscattering is the origin of a non-zero longitudinal resistance.

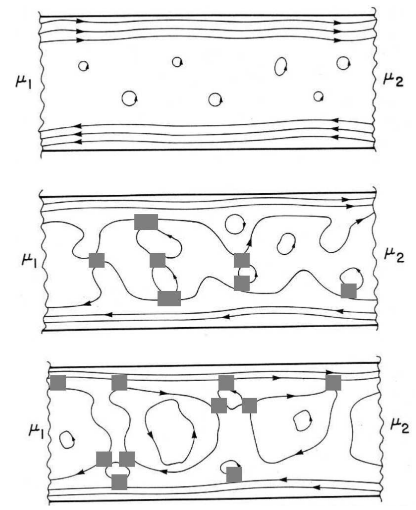

Figure 1.3: Edge channels in a 2D sample at transition from $\nu = 3$ to $\nu = 2$. In the upper part one can see the situation, where the edge channels are separated on both sides of the sample. Transition from one side to the other is not possible and all electrons injected at μ_1 reach μ_2. Thus, the longitudinal resistance is zero. With increasing field, the edge channels move to the centre of the sample and backscattering (grey regions in the middle part) is possible. Consequently, the resistance rises. Increasing the field further, the inner one form closed loops with decreasing radii and the backscattering possibility decreases (lower part). Figure taken from [Buh04].

One can distinguish between extended states near the sample boundaries, those which form the edge channels and localised states, encircling potential maxima and minima in the bulk. Hence, the QHE can be described by the combination of the existence of localised states and edge currents. A first experimental proof for the existence of edge channels was given by Fontein *et al.* [FKH$^+$91].

Only two years after the discovery of the integer QHE, Tsui *et al.* [TSG82] measured a Hall plateau corresponding to the filling factor $\nu = 1/3$. Whereas the phenomenon of the integer QHE can be explained in terms of a single particle effect, as done in the section above, the fractional QHE requires a many particle theory. An interpretation of Laughlin's wave function [Lau83] is the composite fermion concept introduced by Jain *et al.* [Jai92]. Here, every electron is coupled with $2n$ flux quanta. In the case of $n = 1$, the effective field for the composite fermion is zero at $B_{\nu=1/2}$ and the plateaus occur at the corresponding values of the effective integer QHE of the composite fermion.

1.5 Ballistic Transport

In the previous section we discussed the semiclassical extension to the Drude transport theory, which essentially means that Fermi-Dirac statistics was taken into account, but the dynamics of electrons at the Fermi level was assumed to be classical. In connection with the Landau quantisation, this description is satisfactory for many transport experiments. In contrast, a different theory is necessary, if the device dimensions are on the order of the mean free path $l = v_F \tau$, where v_F is the Fermi velocity and τ the scattering time. Therefore the Landauer-Büttiker (LB) theory, that will be explained in this section, can be used. Phenomena related to the phase coherence length, which is usually much larger than l, will be analysed in chapter 2 separately. A comprehensive review related to the quantum transport in semiconductor nanostructures is given by Beenakker and van Houten in their treatise with the same name [BvH91].

In the LB theory the electron transport is described in terms of transmission probabilities. The following derivation is taken from a lecture given by R.R. Gerhardts at Würzburg university in the spring term 2000. Assume we have a sample with four contacts, which are connected via one-dimensional leads, as show in Figure 1.4. The sample scatters incoming electrons elastically into outgoing channels. The leads are quasi one-dimensional conductors, which means that the energy is quantised in n modes. For lead i, the energy values are given by

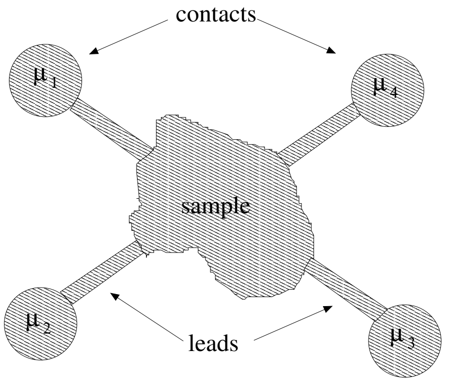

Figure 1.4: Sample connected via one-dimensional leads with the contacts. The contacts have the chemical potential μ_i. Incoming electrons are scattered elastically into outgoing channels.

$$E_n + \frac{\hbar^2 k_n^2}{2m} = E_F. \tag{1.19}$$

If $E_n < E_F$ we have two states $k_{i,n}^{\pm}$, where $k_{i,n}^{-}$ is from contact i towards the sample and $k_{i,n}^{+}$ vice versa. The number of modes in lead i is called N_i. The contacts are systems in equilibrium with chemical potential μ_i. They act as source and drain of carriers and energy (reservoirs). In the contacts themselves the electrons are in thermal equilibrium due to inelastic scattering events therein. The work to be done in order to bring an electron from reservoir i to j is $\mu_i - \mu_j = e(V_i - V_j)$, where e is the electron charge e and $V_i - V_j$ the Voltage between these contacts.

At equilibrium $\mu_i = \mu_0$ is valid for all contacts. We assume $\mu_i = \mu_0 + \Delta\mu_i$. Then the contact i injects the current $\frac{e}{h}N_i\Delta\mu_i$ into lead i and the current reflected into this lead is $-R_{ii}\frac{e}{h}\Delta\mu_i$. Additionally, the current $-\frac{e}{h}T_{ij}\Delta\mu_i$, which is injected into lead i from another contact j has to be considered. Thus, this provides us with the Büttiker equation for the current in lead i:

$$I_i = \frac{e}{h}\left[(N_i - R_{ii})\mu_i - \sum_{j\neq i} T_{ij}\mu_j\right] \tag{1.20}$$

Current conservation requires $N_i - R_{ii} = \sum_{j\neq i} T_{ji}$ and the Casimir-Onsager relations, which are obvious from microscopic arguments are now

$$R_{ii}(\vec{B}) = R_{ii}(-\vec{B}) \tag{1.21}$$

$$T_{ij}(\vec{B}) = -T_{ji}(-\vec{B}) \tag{1.22}$$

Defining the resistance $R_{mn,kl} = \frac{\mu_k - \mu_l}{eI_{nm}}$, directly gives us the van der Pauw condition: $R_{12,34}(\vec{B}) = R_{34,12}(-\vec{B})$.

Now we shall focus our attention on a four terminal probe with a cross shaped geometry, as we have investigated in section 4.2. In order to demonstrate that the transport properties are dominated by ballistic effects, nonlocal transport measurements were performed, because the results in this setup are in contrast to those expected, if the transport were dominated by diffusive scattering. The nonlocal resistance measurement setup is as follows: The current is driven through adjacent contacts (from contact 1 to contact 2 in Figure 1.5) while the voltage is measured between the other adjacent contacts (contacts 3 and 4). After long calculations [Ger00], or as often written in a textbook, as you can easily see, the nonlocal resistance (NLR) $R_{12,34} = \frac{V_{34}}{I_{12}}$ is derived, using the LB theory, to be

$$R_{12,34} = \frac{V_{34}}{I_{12}} = \frac{h}{2e^2}\frac{T^2 - t_r t_l}{(t_r + t_l)(2T^2 + 2(t_r + t_l)T + t_r^2 + t_l^2)}, \tag{1.23}$$

where in our notation, T is the transmission probability of electrons from contact 1 into contact 3, and t_l and t_r are the transmission probabilities from contact 1 to contacts 2 and 4 respectively. In the diffusive case, no voltage signal would be expected to appear between contacts 3 and 4 in this geometry, whereas in the ballistic regime, electrons injected from contact 1 into the cross reach the opposite channel before they are scattered. This leads to charge accumulation at contact area 3 and thus to the NLR signal. Application of a small magnetic field perpendicular to the 2DEG plane deflects the ballistic electrons due to the Lorentz force and therefore the voltage signal between 3 and 4 decreases. Due to multiple specular reflections at the rounded cross boundaries, the electrons then can be scattered

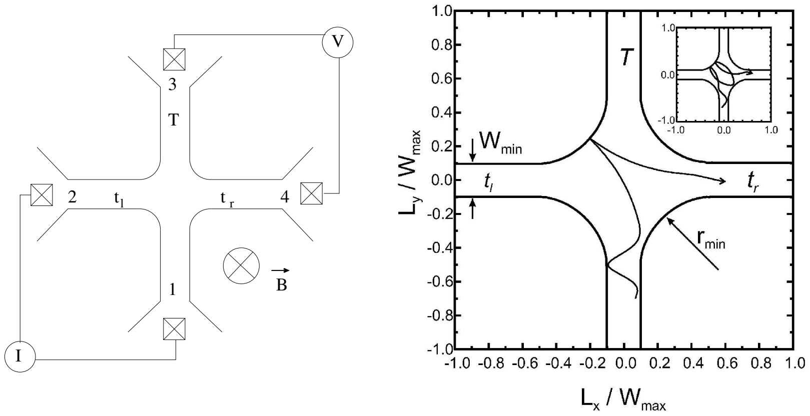

Figure 1.5: Left: Setup to measure the nonlocal resistance. The current is driven from contact 1 to contact 2, while the relative charging of contacts 3 and 4 is measured with a voltmeter. Right: Classical rebound trajectories in a cross shaped geometry with rounded borders: In a small magnetic field, the electrons can be scattered elastically into the opposite contact. Figure taken from [HBGM98]

elastically into the opposite contact 4. Two classical trajectories of this case are shown in Figure 1.5. Thus, the product of the transmission probabilities t_l and t_r can exceed T^2 and the NLR, calculated in equation (1.23), becomes negative. Enlarging the magnetic field further, such that the cyclotron radius becomes smaller than the curvature of the corners, all electrons will be *guided* into one of the side contacts. Hence, T^2 and either t_l or t_r become zero, and therefore, the numerator in equation (1.23) is zero and consequently also the NLR.

An alternative measurement to the four-terminal configuration introduced above is a three-terminal configuration. Hereby, the contact configuration is the same as before but the contacts 2 and 4 (Fig. 1.5) are now grounded. According to LB, the measured signal in that case is

$$R_{12,34} = \frac{V_{34}}{I_{12}} = \frac{h}{2e^2}\frac{T}{(t_r+t_l)(2T+t_r+t_l)}. \tag{1.24}$$

A comparison with equation (1.23) shows that in the three terminal geometry again a maximum around $B = 0$ is expected in the ballistic case but the negative dips should be absent.

In the Hall geometry, which means that the current is driven from contact 1 to contact 3 and the voltage is measured between contacts 2 and 4, the Hall resistance can be calculated to

$$R_{13,24} = \frac{V_{24}}{I_{13}} = \frac{h}{2e^2}\frac{t_r-t_l}{(2T^2+2(t_r+t_l)T+t_r^2+t_l^2)}. \tag{1.25}$$

Here, an anomalous Hall effect is expected in an intermediate magnetic field range, when the transmission probabilities for contact 2 and 4 (t_l, t_r) are in the same order of magnitude.

1.6 Monte-Carlo Simulations

To compare the results of transport experiments in the ballistic regime with the LB theory, classical electron trajectories can be calculated. One of the most commonly used methods is the simulation with Monte-Carlo (MC) techniques. The application of this method to the above situation has been successfully demonstrated [BvH89; BvH90; HBGM98; DGG$^+$03]. The program code, used in this thesis, was originally written by C.W.J. Beenakker and adapted by E.G. Novik.

For the numerical calculation of the corresponding transmission probabilities in a cross shaped structure, we assume, that the electrons are injected through contact 1 into the cross with Fermi velocity v_F and an arbitrary angle distribution. According to this model the electrons are subsequently specularly reflected at the sample boundaries. The electrons reaching contact 2, 3 or 4 are counted and provide directly the transmission probabilities, correspondingly. The only initial parameter, besides the sample geometry, is v_F, which is derived from the carrier density. In order to simulate a sample with a mean free path of the same magnitude as the device dimensions, we vary the scattering time τ. This means, that the probability of the electron being scattered in the time Δt ($\Delta t \ll \tau$) is $\Delta t/\tau$. After each scattering process, the direction of motion is altered. Several scattering mechanisms have been assumed and simulated as described in detail in section 4.2. Figure 1.6 shows some typical trajectories for different scattering times τ, which are normalised with $\tau_0 = W_{max}/v_F$. The boundary potential is assumed to be parabolic, and the radius of the boundary curvature is $r = (1 - W_{min})/2$ with the parameters W_{max} and $W_{min} = W_{max}/2$ from the sample geometry. Measurements on cross shaped

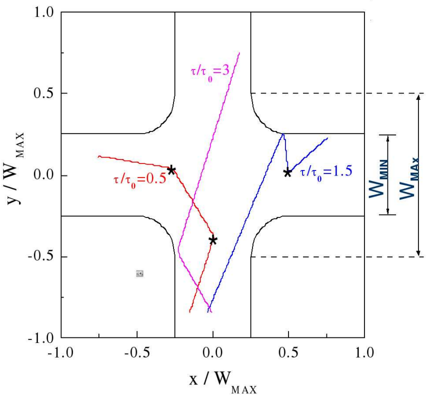

Figure 1.6: Monte-Carlo simulation of classical electron trajectories in a cross shaped structure with rounded borders. The scattering time τ is normalised with $\tau_0 = W_{max}/v_F$. The maximum and minimum widths, W_{max} and W_{min},respectively, are determined from the sample geometry, e.g., SEM photographs, as shown in Figure 4.1.

structures on HgTe QWs in the ballistic transport regime and the associated MC simulations will be presented in section 4.2.

1.7 Summary

In this chapter a short outline of the transport theory was given. Starting with the classical Drude model, semiclassical extensions to it have been made, such as the inclusion of Fermi-Dirac statistic, the effective mass approximation and the Landau quantisation. Effects of the Landau quantisation, since they are important for the understanding of the measurements in the following chapters, have been explained in more detail. Thus, the Shubnikov-de Haas and the quantum Hall effect have been analysed.

In the frame work of this thesis, the first nanostructures on Hg-based quantum well structures have been realised. Hereby ballistic transport phenomena were observed and therefore, the Landauer-Büttiker theory has been introduced. With this theory the magneto-transport experiments on such structures can be described. Finally, the calculation of classical electron trajectories using Monte-Carlo simulations has been presented. Herewith, a comparison of experimental data with the LB theory will be presented in the corresponding section 4.2.

Chapter 2

Phase Coherence

Magneto-transport experiments often require the quantum mechanical [Mes69; Sak95] description of the carriers, especially, when the device dimensions are on the order of the phase coherence length. For our samples this is the case for a length-scale of a few tens of micrometer. Examples of these effects, that will be discussed later in this chapter in detail, are the universal conductance fluctuations, anti-localisation due to strong spin-orbit coupling and geometric phases such as Berry phases.

2.1 Phase in Physics

In quantum mechanics, the wave functions Ψ and $\Psi' = \Psi e^{i\Phi}$, where Φ is an arbitrary phase difference, represent the same state of a physical system, and are, therefore, equivalent. A simple demonstration of the equivalence is given by the calculation of the expectation value of an observable A, as follows:

$$\begin{aligned} \langle A \rangle \Psi &= \langle \Psi | A | \Psi \rangle = \int \Psi^* A \Psi \\ \langle A \rangle \Psi' &= \langle \Psi' | A | \Psi' \rangle = \int \Psi^* e^{-i\Phi} A \Psi e^{i\Phi} = \langle A \rangle \Psi. \end{aligned}$$

The reason for this is the gauge invariance of the quantum mechanical theory. On the other hand, the phase contains information about the temporal evolution of the system, i.e., a shift in the time axis. Thus, the phase is irrelevant for an isolated wave function. But if the wave function is a superposition of two functions, the relative phase difference cannot be neglected. This is illustrated in the following example. If we assume that $\Psi_1 = c_a \Psi_a + c_b \Psi_b$ and $\Psi_2 = c_a \Psi_a e^{i\Phi} + c_b \Psi_b$, then the corresponding expectation values are

$$\begin{aligned} \langle A \rangle \Psi_1 &= \langle \Psi_1 | a | \Psi_1 \rangle = \\ &= |c_a|^2 \langle A \rangle \Psi_a + |c_b|^2 \langle A \rangle \Psi_b + c_a^* c_b \langle \Psi_a | A | \Psi_b \rangle \\ &+ c_b^* c_a \langle \Psi_a | A | \Psi_b \rangle \end{aligned}$$

$$\begin{aligned} \langle A \rangle \Psi_2 &= |c_a|^2 \langle A \rangle \Psi_a + |c_b|^2 \langle A \rangle \Psi_b + c_a^* c_b e^{-i\Phi} \langle \Psi_a | A | \Psi_b \rangle \\ &+ c_b^* c_a e^{i\Phi} \langle \Psi_a | A | \Psi_b \rangle. \end{aligned}$$

Because the non-diagonal elements in the matrix are complex conjugated they can be written as

$$\begin{aligned} \mathrm{A_{nd}} &= 2\mathrm{Re}\{c_a^* c_b e^{-i\Phi} \langle \Psi_a | A | \Psi_b \rangle\} \\ &= 2\mathrm{Re}\{c_a^* c_b \langle \Psi_a | A | \Psi_b \rangle\} \cos\Phi + 2\mathrm{Im}\{c_a^* c_b \langle \Psi_a | A | \Psi_b \rangle\} \sin\Phi. \end{aligned}$$

Here it can be seen, that the relative phase of the components plays an important role. This leads to interference effects such as amplification and annihilation.

2.2 Aharonov-Bohm Effect

A well known example illustrating the relevance of phase in physics is the Aharonov-Bohm effect [AB59]. In their article, Aharonov and Bohm describe the *significance of electromagnetic potentials in the quantum theory*. The effect was first described eleven years earlier by Ehrenberg and Siday [ES49], but their article went unnoticed.

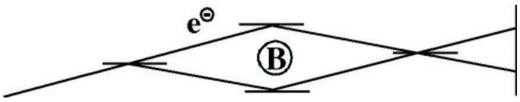

Figure 2.1: Schematic setup of the Aharonov-Bohm effect: an electron wave packet surrounds an isolated magnetic flux line and interferes on the screen.

To explain their idea, Aharonov and Bohm suggested the following thought experiment: Assume that an electron wave packet surrounds an isolated magnetic field line. Then, from the classical point of view, this will not influence the electron, because there is no field on the path. Aharonov and Bohm showed that in the quantum mechanical description, the phase of the electron depends on the enclosed magnetic flux, i.e., $d\varphi = \vec{A}d\vec{s}$. Although the flux on the electron path is zero, the vector potential is not zero and the phase shift can be calculated using Stoke's theorem for the closed loop integral of the enclosed vector potential. The first experimental proof was provided by Chambers one year later with a modified electron microscope [Cha60]. He divided an electron beam with an electrostatic Al biprism, inserted a thin magnetic iron needle and then observed the interference pattern on a screen. Another possibility is the definition of two separate paths by electron lithographical patterning of a semiconducting crystal, e.g., in a ring shaped structure. Magneto-transport experiments on such structures will be shown later in this work. Applying a magnetic field perpendicular to the plane of motion results in periodic oscillations of the conductance. The phase can be calculated using

$$\Phi/\Phi_0 = \pi r^2 B/(h/e), \tag{2.1}$$

where Φ/Φ_0 is the enclosed magnetic flux divided by the flux quantum, r is the radius of the ring, B the applied magnetic flux, h the Planck constant and e the electron charge. The period for a ring with radius 1 μm is 1.3 mT. An example is given in the following chapter 4 in Figure 4.11.

2.3 Aharonov-Casher Effect

According to the Maxwell equations, symmetric effects are observed in many systems. For the Aharonov-Bohm (AB) effect the corresponding effect is called the Aharonov-Casher (AC) effect [AC84]. Previously, we discussed the motion of an electric monopole, which encircles a magnetic dipole in the stationary reference

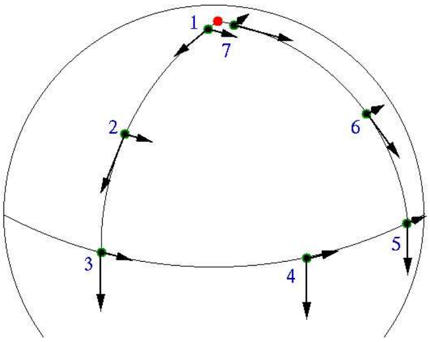

Figure 2.2: Parallel transport of two orthogonal vectors on a sphere, i.e., translation without twisting them around the local vertical axis.

frame of the magnetic dipole. From the stationary reference frame of the electron, we see a magnetic dipole surrounding the electric monopole. In three dimension this can be translated in a cyclic motion of the magnetic dipole around an electrostatic charged wire and is therefore the analogon to the magnetic flux line in the AB effect.

The first demonstration of the pure AC effect without the superimposed Coulomb effect was carried out with neutral particles with a magnetic moment, i.e., neutrons [COK$^+$89]. Later this effect was observed with other neutral particles that have a magnetic dipole moment [GSW95; ZZRH95].

In our experiments with electrons the AC phase can be investigated by applying a gate voltage perpendicular to the plane of movement. In the measurement results (Fig. 4.13), presented in the following chapter 4, one can see these oscillations with an amplitude of the order of the conductance quantum.

2.4 Berry Phase

The phase effects described in sections 2.2 and 2.3 can be summarised and generalised as geometric phase effects. The first extensive description of these effects in the adiabatic limit was given by Berry [Ber84b]. Thereby adiabatic means, that a time dependent Hamiltonian evolves slowly with time and an eigenstate of the system does not change into another eigenstate [Mes69]. For example when an electron moves slowly through an inhomogeneous magnetic field and the spin of the electron retains its alignment along the local field direction, i.e., continously changes its orientation adiabatically to coincide with the local field direction. In other words, the spin part of the state evolves as an instantaneous eigenstate of the local Zeeman interaction. Geometric phase effects can be explained using an analogon in differential geometry. In Euclidean geometry parallel transport, e.g., of a vector, can be described by translating the vector without rotating it. On a continuously differentiable surface, parallel transport is defined as parallel transport in the actual tangential plane. In a strict sense, this is the definition for infinitesimal motion, but connecting a path of such neighbouring points is also called parallel transport. Parallel transport along a closed path in Euclidean geometry will not result in any phase shift. In contrast, consider an in-plane vector at the north pole of a sphere pointing towards the south pole. We move it along a meridian to the equator, and then change the direction of motion and travel along the equator a quarter of its length to the east without twisting the vector around the local normal axis. Now, we move it along a meridian back to the north pole. The result is, that the vector is still pointing towards south, however, the vector is rotated 90° with respect to the initial orientation, in spite of the fact that local parallel transport was carried out. Detailed considerations show, that the phase shift results solely due to the curvature of the surface, which is the same reason that the sum of the inner angles of a triangle may be more than 180°, e.g, in our example 270°. A detailed overview of the theory of Berry phase and experimental realisations is given in the review article of Resta [Res00]. For further reading the nearly 100 citations therein can be used.

2.5 Spin-orbit Berry Phase

Recently, a special manifestation of Berry phase aroused much interest in semiconductor physics: the spin-orbit (SO) Berry phase. Potential applications of spintronics require the sustainance of electron spin coherence. The observation of SO Berry phase can be a milestone on the way to spin-coherent quantum circuits in semiconductors. Although there exist many theoretical descriptions and proposals for experimental realisation [LGB90; ALG93; Res00; EL00], till now it has not been directly observed. Some groups [MHK$^+$98; NKT02; YPS02] have reported evidence for SO Berry phase, but due to the complexity of the indirect derivation of the data, these results are not commonly accepted. For example, Morpurgo *et al.* analysed the Fourier spectra of ensemble averages of AB oscillations and concluded, in their own words, that the splitting in the peak of the h/e oscillations "may be a manifestation of the geometric phase induced on the spin of an electron traversing the ring" [MHK$^+$98]. Furthermore, Yau *et al.* analysed Fourier spectra of averaged AB oscillations, where they found side peaks near the central peak which occurred at $\pi r^2/(h/e)$. By means of a comparison with simulation data they claim to have evidence for the Berry phase, although they admit discrepancies between their experimental data and the simulation [YPS02]. Moreover, they do not require the adiabaticity criterion be fulfilled.

One possible experimental setup, in which the SO Berry phase can be explored, are Aharonov-Bohm rings in semiconductors with a strong Rashba spin splitting [ALG93; EL00]. As described in section 2.2, charged particles aquire an additional phase of $2\pi\Phi/\Phi_0$ after traversing a closed circuit, due to the AB-effect. The Rashba SO splitting can be expressed as a Zeeman like radial magnetic field (B_{eff} in Fig2.3). The angle Θ between the external magnetic field (B_{ext}) and the resulting magnetic field is the half angle of the cone.

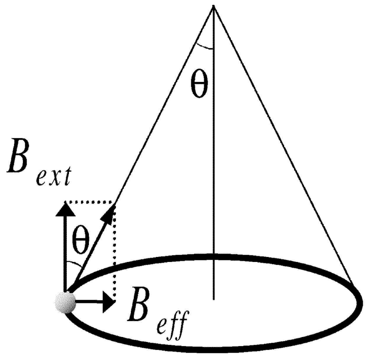

Figure 2.3: Experimental setup to identify the SO Berry phase: motion of an electron in an AB ring in a material with Rashba SO splitting leads to an additional radial effective magnetic field (B_{eff}). Applying a perpendicular external magnetic field (B_{ext}) leads to a resultant field with angle Θ.

For particles with spin 1/2 the SO Berry phase can be calculated to be $\pi(1-\cos\Theta)$ [Sak95]. In the calculation of the SO Berry phase in Fig. 2.4 the amplitude of the AB conductance is plotted as function of the external (x-axis) and the internal (y-axis) magnetic fields in a contour plot. Cross section lines parallel to the x-axis in this plot are AB conductance oscillations for a particular value of the Rashba splitting. The SO Berry phase can be identified by the typical cross-over from minimum (dark regions) to maximum (bright regions) and vice versa in the conductance, that occur when the internal field is increased (y-direction).

2.6 Aharonov-Anandan Phase

In a fundamental generalisation of Berry's idea, Aharonov and Anandan (AA) lifted the adiabatic restriction and examined the geometric phase for the non-adiabatic cyclic evolution [AA87]. By removing the dynamic part from the total phase acquired in the cyclic evolution, Aharonov and Anandan were able to define a non-adiabatic geometric phase, now called the Aharonov-Anandan (AA) phase. The AA phase can be calculated to be $\Phi_{\text{AA}} = \pm\pi(1-\cos\alpha)$, where α is, in contrast to the above introduced Θ, the resulting angle of the not fully oriented, tilted spin and the plane of movement. Here, not fully oriented means that the time of the spin precession is smaller or equal to the time of travel in the ring, i.e.,

$$\frac{2\pi}{\omega_L} \leq \frac{2\pi r}{v_F},$$

where ω_L is the Lamour frequence, r the radius of the ring and v_F the Fermi velocity. Qian and Su demonstrated the existence of the AA phase in the AC effect [QS94]. Choi *et al.* investigated the non-adiabatic AC phase in mesoscopic rings embedded in criss-crossing electric fields [CYRK97]. In the adiabatic limit this AA phase becomes the SO Berry phase suggested by Aronov and Lyanda-Geller [ALG93]

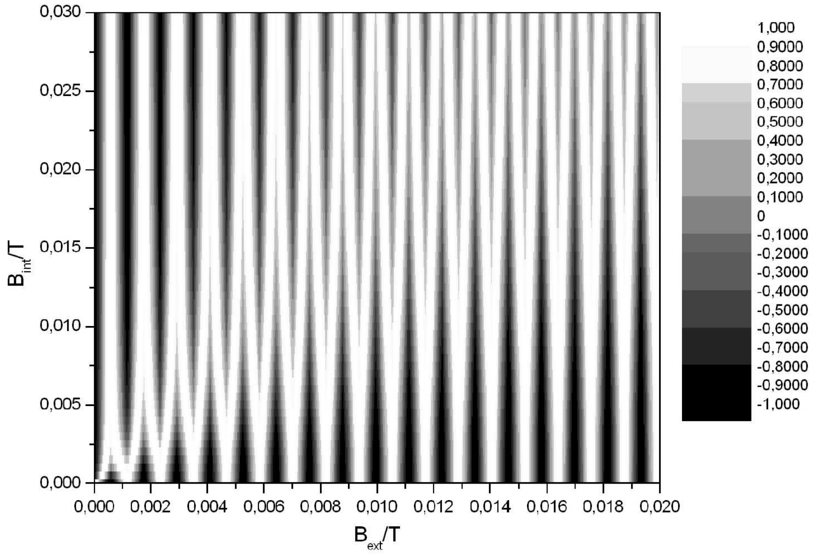

Figure 2.4: Calculation of the AB-oscillations depending on the internal (B_{int}) and external (B_{ext}) magnetic field in a contour plot. Cross section lines parallel to the x-axis are AB conductance oscillations for a particular value of the Rashba SO splitting.

2.7 Universal Conductance Fluctuations

The realisation of a two dimensional electron gas (2DEG) in a HgTe, quantum well (QW) exhibits, in contrast to an ideal system, deviations in the periodicity of the lattice. This may originate from defects in the crystal structure such as vacancies, dislocations, impurities or from lattice vibrations (phonons). Phonon scattering is inelastic, which means that the electron eigenstate changes, but in elastic scattering events the momentum parallel to the scattering centre and the phase of the wavefunction is conserved. Similar to the AB effect an electron wave packet propagates on different paths through the 2DEG which leads to constructive or destructive interferences [FH65]. With the application of a perpendicular magnetic field the electrons are deflected and hence completely new paths are chosen by them. This results in a conductance pattern, called universal conductance fluctuations (UCF) [LS85; LSF87], which are stable in time and characteristic for a given sample in a given temperature cycle. The fluctuations disappear slowly and smoothly as temperature is increased. When the temperature is decreased again, another pattern appears due to a different local potential landscape due to impurities and hence due to different possible paths. Because of this characteristic, the UCF were called “magneto-fingerprints” of the sample in the original paper [LS85]. Following this idea, several groups have used the UCF as a magneto-fingerprint of a special frozen spin configuration in mesoscopic spin glasses [dVLF91; CBD95; JWK$^+$98]. $Hg_{1-x}Mn_xTe$ samples show a phase transition from the paramagnetic to the spin-glass phase at temperatures below 1 K (see Fig.3.8). A possible transition in the UCF will be discussed in section 5.3.

2.8 Weak Localisation and Weak Anti-Localisation

Additional effects related to phase coherence are weak localisation and weak anti-localisation. The origin of these two effects is similar, but the consequences on magneto-transport measurements are opposite. Starting with the weak localisation, both effects will be explained in this section.

In the case of phase coherent transport, the probability of finding an electron at its origin is four times higher than anywhere else in the sample, which leads to a localisation of the carriers and hence to an increase of the resistance. The result can be understood in terms of constructive and destructive interferences due to the time reversal invariance [Mes70] of the Schrödinger equation [AAR79; GLK79; Ber83; Ber84a]. The different possible paths can be calculated with the Feynman path integral method [FH65]. An applied magnetic field breaks the time reversal invariance and hence, the constructive interference vanishes. The possibility of backscattering decreases and so the resistance decreases with increasing magnetic field. The effect is called “weak” due to the relative weak fields (about 10 mT) necessary to destroy this effect. In the presence of strong spin-orbit coupling, as it exists in HgTe-QWs, the Hamiltonian is modified accordingly but the effect is the opposite effect, i.e., weak localisation becomes weak anti-localisation. At zero magnetic field electrons on the same paths interfere destructive, the possibility of backscattering is reduced and the resistance is lower (anti-localisation) [HLN80]. With increasing magnetic field the preference for destructive interference is reduced and the resistance rises. The observation of this effect will be presented in the following chapters.

2.9 Summary

When the device dimensions are reduced, quantum effects can be observed in magneto-transport experiments. In this chapter the relevance of the quantum mechanical phase of a wave function was elucidated. The consequences of this, for several magneto-transport interference experiments, were presented. The observation of Aharonov-Bohm, Aharonov-Casher, Aharonov-Anandan, Berry phase, and localisation effects are explained in detail in the following chapters.

Chapter 3

Hg Based Heterostructures

Mercury-based heterostructures are very different in comparison with group IV (Si, Ge) or III-V (GaAs) semiconductors. The samples investigated in this thesis are MBE[1] grown heterostructures. They consist of a $\mathrm{Hg_{1-x}Mn_xTe}$ quantum well (QW) embedded in barriers of $\mathrm{Hg_{1-x-y}Cd_xMn_yTe}$. The barriers are modulation doped, either on one or on both sides of the QW, with Iodine. Thus, the confinement potential of the QW is asymmetric or symmetric, respectively. The incorporation of typically 2% Manganese in the QW leads to a diluted magnetic semiconductor (DMS), which has additional properties, that are introduced here and discussed in detail in chapter 5.

---

[1] **m**olecular **b**eam **e**pitaxy

3.1 Band Structure of $Hg_{1-x}Mn_xTe$ Quantum Wells

In contrast to type-I QW e.g., consisting of a GaAs/AlGaAs heterostructure, type-III $Hg_{1-x}Mn_xTe$ narrow gap QWs with a well width of more than 6 nm and a manganese content less than 7% have an inverted band alignment. Whereas in type-I QWs the conduction band (CB) has Γ_6 and the valence band (VB) Γ_8 symmetry, in type-III QWs with an inverted band alignement the Γ_6 band is the VB and the Γ_8 band is the CB. Therefore, this alignment is also called an inverted band structure. Additionally, the degeneracy of the Γ_8 band is lifted. It splits into the heavy hole band, named $H1$, and the light hole band $L1$. The latter shifts to lower energies, and consequently, the $H1$ band is the CB. Thus, the subband wave functions for $k_{||} = 0$ are pure $|\Gamma_8, \pm 3/2\rangle$ states.

The actual situation is more complex. The band structure of a HgTe-QW depends on the confinement potential, i.e., the well width d_{HgTe}. To provide a quantitative

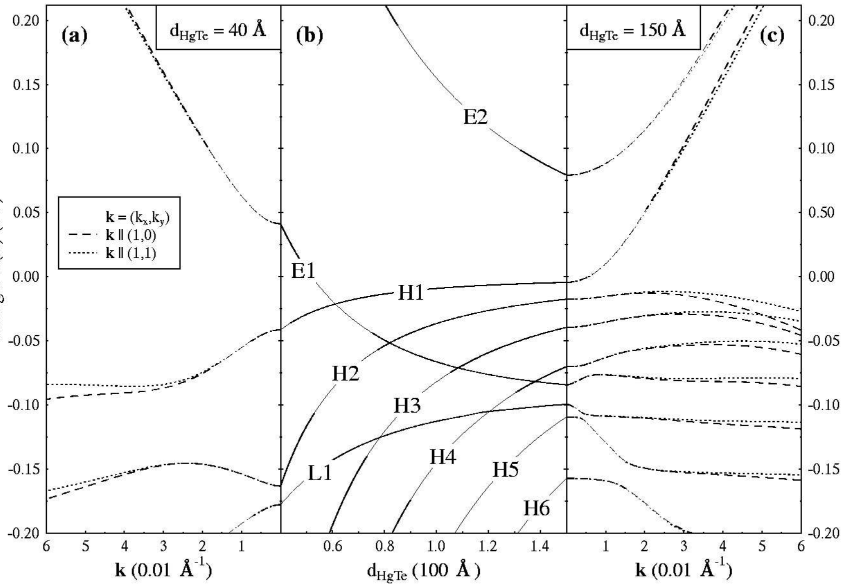

Figure 3.1: (a) Band structure of a $HgTe/Hg_{0.3}Cd_{0.7}Te$ QW with $d_{\mathrm{HgTe}} = 40\,\AA$ well width. (b) Dependence of the bands on the well width d_{HgTe}. (c) Band structure of a $HgTe/Hg_{0.3}Cd_{0.7}Te$ QW with $d_{\mathrm{HgTe}} = 150\,\AA$ well width. In (a) and (c) the dispersion of the particular subbands for $k_{||}||(1,0)$ and $k_{||}||(1,1)$ are shown [PJ00].

description, self-consistent Hartree calculations have been carried out. The band structure of HgTe QWs with $Hg_{0.3}Cd_{0.7}Te$ barrier is described by Kane's three-band 8×8 $\mathbf{k} \cdot \mathbf{p}$ model including second-order remote band contributions. The envelope function method has been used to calculate this band structure as shown in Figure 3.1 [PJ00].

As can be seen in Figure 3.1(b), narrow QWs with a well width less than 60 $\AA$ exhibit a normal band alignment. Around $d_{\mathrm{HgTe}} = 60\,\AA$, the electron band $E1$ crosses the heavy hole band $H1$ and the band structure is inverted, as mentioned above. All QWs, investigated in this thesis, have a well width of 120 $\AA$ and are therefore in the regime of inverted band structure. This type of heterostructure is indeed unique in II-VI semiconductor, because of the availability of the semimetallic HgTe as QW material.

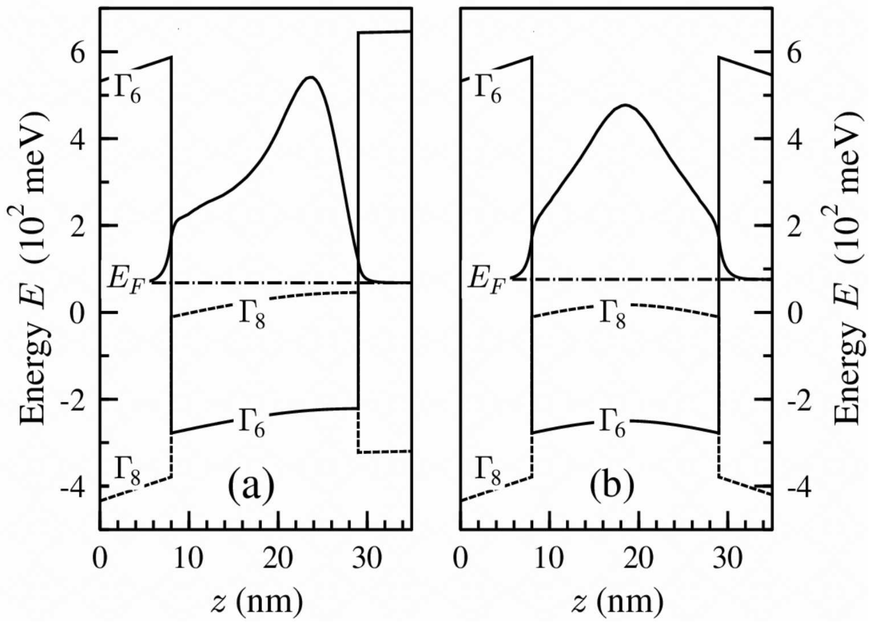

Figure 3.2: Band edge profiles of the Γ_6 (solid) and Γ_8 (dashed) band and the electron probability (thick solid line) of the $H1$ subband in an asymmetric (a) and symmetric (b) case.

Although the QWs investigated in this thesis are n-type, i.e., the charge carriers are electrons, their wave function corresponds to an eigenvalue equation for holes due to the heavy hole character of their states. This leads to an apriori surprising result. Usually, the maximum of the electron density distribution in an asymmetric QW is shifted to the minimum of the confinement potential. However, the heavy hole character shifts the maximum of the electron density towards the maximum of the confinement potential, as it is expected for holes. This situation is illustrated in Fig. 3.2(a). Here, the band edge potentials for the asymmetric (a) and symmetric (b) case of a QW with $d_{HgTe} = 12$ nm are plotted. The electron probability distribution for both cases together with the Fermi energy E_F is shown. The asymmetry of the charge distribution as well as the penetration of the wave function into the barrier can be clearly seen.

The incorporation of manganese atoms into the QW modifies the band structure. A schematic plot of the energy-band structure of $\mathrm{Hg_{1-x}Mn_xTe}$ for various Mn concentrations x is shown in Figure 3.3. For low Mn concentrations (x<7%), HgMnTe is as HgTe a zero gap material with inverted band structure (c.f. sec. 3.1). For higher Mn concentrations (x>7%), the Γ_6- and Γ_8-band change their roles and the fundamental energy gap becomes positive [BRG+81]. Recently, this model has been extended in order to take the influence of the $sp-d$ exchange interaction on the band structure of magnetic QWs into account [NPJJ+04]. Furthermore, the incorporation of magnetic ions causes a temperature and magnetic field dependent effective g-factor. For further details as, e.g., the matrix elements of H_{ex} in terms of the Bloch functions, the reader is referred to [NPJJ+04]. A comparison of such band structure calculations of magnetic QWs with magneto-transport experiments is given in section 5.2. A more detailed derivation of the description of the magnetic interaction is presented in the following section.

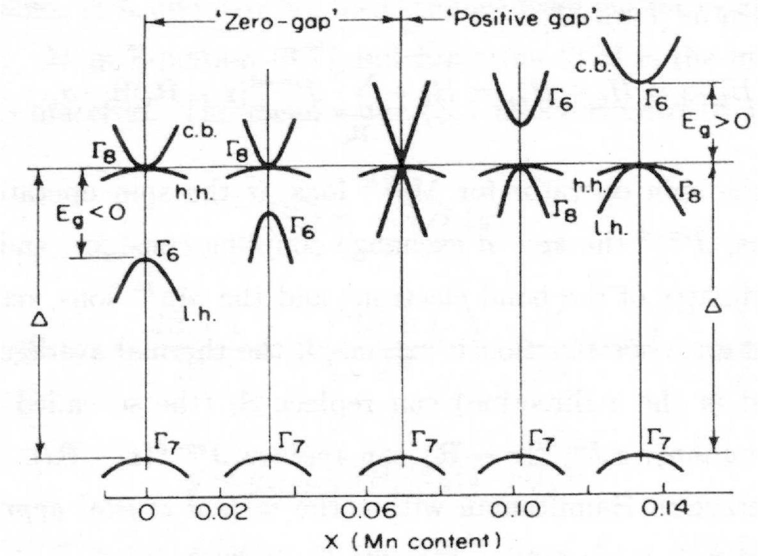

Figure 3.3: Schematic energy-band structure of $\mathrm{Hg_{1-x}Mn_xTe}$ for different Mn contents at the centre of the Brillouin zone (taken from [BRG+81]).

3.2 Giant Zeeman Splitting

For the description of the magnetic exchange interaction, an additional exchange term (H_{ex}) in the Hamiltonian (H) of the non-magnetic case is added. According to Winkler [Win03] and Furdyna [Fur88] the total Hamiltonian can now be written as

$$H + H_{ex} = H - \sum_{\mathbf{R}_n} J(\mathbf{r} - \mathbf{R}_n)\sigma \mathbf{S}_n, \tag{3.1}$$

where σ is the spin operator of the band electrons at position $\mathbf{r}$, $\mathbf{S}_n$ is the total spin operator of the nth Mn ion at the position $\mathbf{R}_n$, and $J(\mathbf{r} - \mathbf{R}_n)$ is the electron-ion exchange integral. Since the electron wave function is extended, the spin operator $\mathbf{S}_n$ can be replaced by the thermal average over all states of Mn moments $\langle S_z \rangle$ for a magnetic field in z-direction (mean field approximation). Moreover, within the virtual crystal approximation, $J(\mathbf{r} - \mathbf{R}_n)$ can be replaced by $yJ(\mathbf{r} - \mathbf{R}_n)$, where y is mole fraction of Mn, and the summation is now carried out over all cation sites. The exchange term in Eq. (3.1) then becomes [Fur88]

$$H_{ex} = -\sigma_z \langle S_z \rangle y \sum_{\mathbf{R}} J(\mathbf{r} - \mathbf{R}). \tag{3.2}$$

The average $\langle S_z \rangle$ of the z component of Mn spin in the approximation of non-interacting magnetic moments is determined in the following.

The Mn atom has a half filled $3d$ orbital, i.e., a spin quantum number $S = \frac{5}{2}$. Thus, the resulting magnetic moment of a Mn atom is

$$\vec{\mu} = -\vec{S} \cdot g_{Mn} \mu_B, \tag{3.3}$$

where $g_{Mn} = 2$ is the Landé factor of Mn and μ_B the Bohr magneton. For such a DMS, the above mentioned influence of the Mn on the charge carriers has to be considered. The $sp - d$ exchange interaction between the s and p band electrons with the $3d^5$ Mn states is described by an additional Kondo-like exchange integral in the Hamiltonian of the Mn free system. The eigenvalues of the Schrödinger equation (see eq.(1.16) in section 1.2) then contain an additional, spin-related term with the effective g-factor g^*. In DMS the g^* can be renormalised to [BRG$^+$81]

$$g^* = g_0 + \frac{x(\alpha N_0)\langle S_z \rangle}{\mu_B B} \tag{3.4}$$

for the Γ_6 band and to

$$g^* = g_0 + \frac{x(\beta N_0)\langle S_z \rangle}{3\mu_B B} \tag{3.5}$$

for the Γ_8 band. αN_0 and βN_0 are the exchange integrals for Γ_6 and Γ_8 bands, respectively. The mean value $\langle S_z \rangle$ is determined by the Brillouin function for $S = \frac{5}{2}$:

$$\langle S_z \rangle = -S_0 B_{\frac{5}{2}}(y) \tag{3.6}$$

where

$$B_{\frac{5}{2}}(y) = \frac{2S+1}{2S}\coth\left(\frac{2S+1}{2S}y\right) - \frac{1}{2S}\coth\left(\frac{1}{2S}y\right) \tag{3.7}$$

and

$$y = \frac{g_{Mn}\mu_B SB}{k_B(T+T_0)}. \tag{3.8}$$

Here, B is the magnetic field and k_B the Boltzmann constant. The empirical parameters S_0 and T_0 take into account the existence of clusters and an antiferromagnetic interaction[2] between the manganese ions, respectively.

The strong temperature-dependent and magnetic-field-dependent g^* factor gives rise to a modulation of the Shubnikov-de Haas (SdH) amplitude according to the $\cos(\pi\nu)$ term in equation (1.17), which has been discussed in section 1.2. We exploit these dependences in order to deduce the sample specific parameters S_0 and T_0, as shown in the next section.

The Zeeman splitting is not the only effect which influences the spin-dependent subband splitting. In zinc blende structures bulk inversion asymmetry and structure inversion asymmetry lead to a suppression of the $B = 0$ energy degeneracy (Rashba effect), which will be discussed in detail in section 3.4. However, these effects do not show a temperature dependence in contrast to Zeeman splitting. Therefore it is possible to separate the giant Zeeman splitting from the Rashba spin-orbit splitting by analysing the temperature dependence of the SdH amplitude as demonstrated in section 5.1.

3.3 Antiferromagnetic Temperature and Effective Spin in HgMnTe

For the common description with the Brillouin function (Eq. (3.4)-(3.8)) the antiferromagnetic temperature T_0 and effective spin S_0 in the effective g-factor are very important parameters. These empirical parameters take into account the antiferromagnetic interaction between the manganese ions, and the existence of pairs and clusters of them. The antiferromagnetic exchange interaction [LHEC88] reduces the alignment of the Mn ions in the same way as a higher lattice temperature would cause and therefore $T_0 > 0$ is expected. Pairs and clusters of N manganese ions, which are antiferromagnetic coupled, have in the sum a resulting spin, which is less than $N \cdot \frac{5}{2}$. Hence, the effective spin S_0 is expected to be less than $\frac{5}{2}$.

However, for epilayers and especially QWs like our $\mathrm{Hg_{1-x}Mn_xTe}$ samples with a typical manganese content of x=0.02, grown on thick CdZnTe substrates, it is difficult to measure directly the magnetisation of the magnetic layer. One may deduce the conduction band splitting from the Zeeman shifts in optical experiments, which

---

[2] $d-d$ exchange interaction [LHEC88]

are a combination of the heavy-hole and conduction band splitting. The knowledge of complicated effects such as the non parabolic band structure is required to determine the correct ratios between conduction band and heavy-hole spin splitting. Ignoring these effects may lead to erroneous estimations of the antiferromagnetic temperature and effective spin.

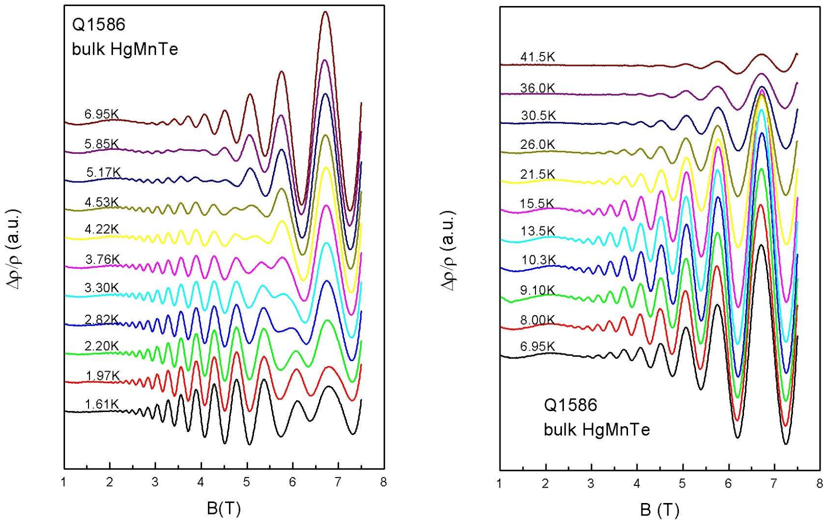

Figure 3.4: SdH oscillations measured at different temperatures for Q1586. The plots are offset for clarity.

An alternative method to deduce these parameters is an analysis of the anomalous SdH behaviour in such materials. Usually, in the non magnetic case with one occupied subband, the maxima and minima of the SdH oscillations are determined by the density of states as described in section 1.3. The amplitude of these oscillations decreases monotonous with increasing temperature according to the relation $\chi/\sinh(\chi)$, where $\chi = \beta' T m'/B$. This is the important relation of the normalised amplitude of the SdH oscillations given in Eq. (1.17). There all the parameters are defined. In the case of a magnetic sample discussed here, the situation is different. The temperature dependent effective g-factor (Eq. (3.4) and (3.5)) causes an oscillatory SdH amplitude with distinct nodes. The node position is not fixed and shifts towards lower magnetic fields with increasing temperature. The dependence of the amplitude from the effective g-factor g^* can be found in the $\cos(\pi\nu)$ term in Eq. (1.17), where $\nu = \delta/\hbar\omega_c = \frac{1}{2}m'g^*$, with the Landau level splitting δ and the Landau level separation $\hbar\omega_c$. Nodes in the oscillations would occur, if the amplitude is zero, $\cos(\pi\nu) = 0$, which means at half-integer values of ν. In Fig. 3.4 SdH oscillations at different temperatures for a $Hg_{0.95}Mn_{0.05}Te$ epilayer are plotted.

While the positions of the maxima and minima are fixed, the amplitudes vary with temperature. In the neighbourhood of nodes they are drastically decreased and their phase change by π after passing the nodal point. If the temperature is high enough, the Brillouin function $B_{\frac{5}{2}}(y)$ approaches $(S+1)y/(3S)\,(y << 1)$ and g^* is magnetic-field independent and only changes slightly with temperature. Then, the effective masses and Dingle temperatures can be deduced by means of the relationships for nonmagnetic semiconductors at temperatures given by 35 K $<$ $T <$ 45 K. Hereby, the effective mass is deduced, using the relation

$$\frac{A(T_1,B)}{A(T_2,B)} = \frac{T_1 \sinh(\beta T_2 m'/B)}{T_2 \sinh(\beta T_1 m'/B)}, \tag{3.9}$$

where A is the amplitude of the SdH oscillations at certain temperature and field, and the other parameters as defined in Eq. (1.17). This was done for different pairs of temperature (T_1,T_2) at a certain B, and then repeated at different fields. In the case of the samples discussed here, the values of m' are significantly enhanced by the high electron concentration.

Parameter	Sample	
	Q1585	Q1586
x	0.0075 ± 0.005	0.05 ± 0.005
d_{epilayer} (μm)	1.8	1.8
n_{electron} (cm^{-3})	1.07×10^{18}	1.37×10^{18}
μ_{Hall}(cm^2/Vs)	1.84×10^4	2.00×10^4
T_0 (K)	2.63	3.35
T_D (K)	28.6	19.5
S_0/S	0.16	0.25
$m' = m^*/m_0$	0.04	0.05

Table 3.1: Summary of sample characteristics for two $Hg_{1-x}Mn_xTe$ epilayers.

The Dingle temperature can be deduced from the magnetic field dependence of the SdH-amplitude at a constant temperature, i.e.,

$$\frac{A(T,B_1)}{A(T,B_2)} \approx \sqrt{\frac{B_1}{B_2}} \exp\left[-\beta T_D m' \left(\frac{1}{B_1} - \frac{1}{B_2}\right)\right]. \tag{3.10}$$

In the Dingle plot, ln $\left[A\sqrt{B}x/\sinh(x)\right]$ (with $x = \beta T m'/B$) versus B^{-1}, the resulting straight line has the slope $-\beta T_D m'$. The parameters obtained for our samples are listed in Table 3.1. The value of T_0 can be easily deduced from fitting the temperature dependent node position using Eq. (3.4) or (3.5), where the values of $\langle S_z \rangle / B$ should be kept constant. Such fits, agree well with the experimental data,

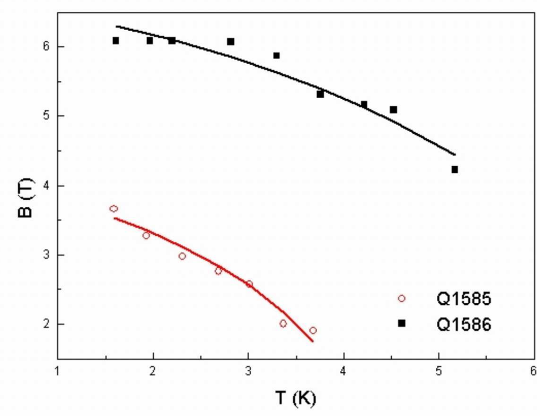

Figure 3.5: Temperature dependent node position. Points are the experimental data and lines are the fitting results.

as shown in Fig. 3.3. From the fits, we obtain $T_0 = 2.63$ K for sample Q1585 and $T_0 = 3.35$ K for sample Q1586. According to Bastard and Lewiner, T_0 is nearly proportional to x(1-x) [BL80]. Using their data, T_0 for a sample with x=0.015 at 2 K, the corresponding values for Q1585 and Q1586 are 4.8 and 5.2 K, respectively. Our experimental values are less than those of Bastard but increasing with x. The actual value of T_0 may be much less than the estimated value for x≥0.05.

Once the value of T_0 is known, the effective spin S_0 can be obtained from the node position, where the value ν must be equal to half of an odd integer. The number of nodes is very sensitive to the choice of ν. We found $\nu = -3/2$ and 1/2 are the only suitable values for Q1586 and Q1585, respectively; otherwise four or more nodes should appear in our magnetic field range. As expected, g^* is negative for the sample with inverted band structure (x=0.05) and positive for the sample with normal band structure (x=0.075). The values for the exchange integrals multiplied with the number of cations per unit volume, $\alpha N_0 = -0.4$ eV and $\beta N_0 = 1.5$ eV, are taken from [BM84] and therewith, the corresponding values of S_0/S are 0.16 and 0.25 for Q1585 and Q1586, respectively. The value of S_0/S proves to be less than 1, presumably due to cluster formation. The S_0 behaviour shows that cluster formation in $\mathrm{Hg_{1-x}Mn_xTe}$ is more likely when the manganese concentration increases. The probability of isolated $\mathrm{Mn^{2+}}$ ions in $\mathrm{Hg_{1-x}Mn_xTe}$ (x=0.06) has been estimated to be only 2%, which is much less than the probabilities of 30%, 10%, and 40% in a cluster for pair, closed-triangle, and open-triangle types, respectively [NRGA+80].

With our deduced sample parameters (Tab. 3.1) we have calculated the normalised SdH amplitude according to Eq. (1.17). These calculated amplitudes for different magnetic fields agree very well with the experimental data, as demonstrated in Fig. 3.6. One can clearly see the effect of the cosine term. As the tempera-

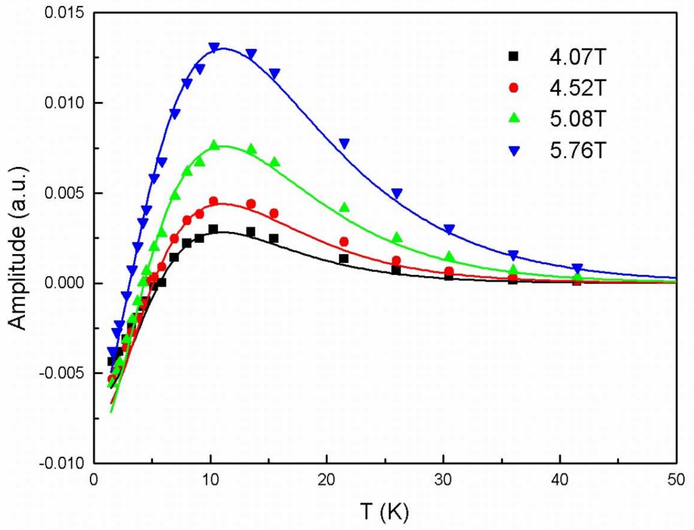

Figure 3.6: Normalised SdH amplitudes at different magnetic fields for sample Q1586. The lines represent calculated values and the points are experimental data.

ture is decreased, the amplitude of the oscillations at first increases in the normal (nonmagnetic) fashion, but as the temperature continues to decrease, the amplitude decreases to zero, and reemerges at still lower temperature with an opposite phase.

3.4 Bychkov-Rashba Spin-Orbit Splitting

Whereas Zeeman splitting of the two spin levels of a conduction band is caused by an external magnetic field, spin-orbit splitting may appear at zero magnetic field due to inversion asymmetry. Two different reasons for this zero field splitting are known: The bulk inversion asymmetry (BIA) of the crystal structure, e.g., zinc blende, can remove the spin degeneracy of electrons in the absence of a magnetic field [Dre55], and also the structure inversion asymmetry (SIA) known as Rashba spin-orbit (SO) splitting such as that found in inversion layers or asymmetric QWs with an asymmetric confinement potential [BR84].

The Rashba effect usually dominates in two-dimensional structures while in particular, the influence of BIA has been shown to be negligible in HgTe based narrow-gap heterostructures discussed here [RML89]. For electrons this spin-splitting is given by [BR84]

$$\varepsilon(k_{||}) = \pm\alpha k_{||}, \tag{3.11}$$

and for heavy-hole systems [Win00], as is the case in Hg-based QWs with an inverted band structure discussed here (s. sec. 3.1),

$$\varepsilon(k_{||}) = \pm\beta k_{||}^3, \tag{3.12}$$

where α and β are the SO coupling constants.

It has to be mentioned, that the SO spin-split states are circular polarised as illustrated in Figure3.7. They contain the same number of spin-up and spin-down spinor components. In a magnetic field the states are not additionally split, but the spins are aligned with respect to the magnetic field. In a simple theoretical model, which takes the Rashba effect and the *sp-d* exchange interaction into consideration, but neglects BIA and nonparabolicity of the band structure, the total splitting δ of the levels can be approximated by [DDR90; Pfe97; PZ99]

$$\delta \approx \sqrt{/\hbar\omega_c - g^*\mu_B B)^2 + \Delta_R^2} - \hbar\omega_c, \tag{3.13}$$

where $\hbar\omega_c$ is the Landau level, $g^*\mu_B B$ the Zeeman, and Δ_R the Rashba splitting energy. In section 5.1 we will show that this simplified model describes our experimental data quite well.

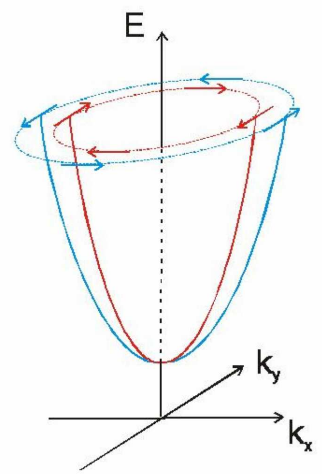

Figure 3.7: Schematic diagram of the Rashba SO splitting into opposite oriented, circular polarised states.

The Rashba SO splitting was first observed experimentally in p-type and n-type GaAs/GaAlAs heterostructures by Störmer *et al.* [SSC$^+$83] and Stein *et al.* [SvKW83], respectively. Zhang *et al.* and Gui *et al.* have shown that the Rashba SO splitting in HgTe QWs has values up to 30 meV and therewith at least four to five times as large as in III-V heterostructures [ZPJO$^+$01; GBD$^+$04]. This can be understood qualitatively because splitting for heavy-holes is proportional to $k_{||}^3$ (s. eq. (3.12)) and not linear with the in-plane wave vector $k_{||}$. According to Winkler [Win00] the carrier densities $N_\pm$ in the spin-split subbands of a heavy-hole band is

$$N_\pm = \frac{1}{2}N_s \pm \frac{\sqrt{2}m^*\beta N_s}{\hbar X}\sqrt{\pi N_s(6-4)/X} \tag{3.14}$$

with

$$X = 1 + \sqrt{1 - 4\pi N_s(2m^*\beta/\hbar^2)^2}. \tag{3.15}$$

From equations (3.14) and (3.15) one can easily show [ZPJO$^+$01] that

$$\beta = \frac{\hbar^2}{2m^*}\sqrt{\frac{X(2-X)}{4\pi N_s}}, \tag{3.16}$$

and

$$X = \frac{2(2+\sqrt{1-a^2})}{a^2+3}, \tag{3.17}$$

where N_s is the total carrier density[3] and $a = \Delta N_s/N_s$.

Although the prediction of the consequences of the Rashba effect shows good agreement with the experimental results, the theoretical description of its origin is still somewhat controversial. An overview of these descriptions is given following the discussion provided by Zhang *et al.* [ZPJO$^+$01]. When the influence of the interface electric fields is neglected, Ohkawa and Uemura have shown, that the spin splitting is proportional to $\langle dV/dz \rangle$, where V is the electrostatic potential energy and z the growth direction of the heterostructure [OU74]. However, Därr *et al.* argued, that the average value of the electric field of the bound states in the first approximation is negligibly small [Fum76]. On the other hand it has been pointed out by Lassnig [Las85] and Winkler and Rössler [WR93] that this conclusion is not correct because the spin splitting of the conduction band is determined by the electric field in the valence band. The importance of spin-dependent boundary conditions, as well as the penetration of the wave function into the barriers and its asymmetry at the interfaces has been emphasised by de Andrada e Silva *et al.* [dAeSlRB97] and Pfeffer and Zawadzki [PZ99], and has been demonstrated in a recent experiment on InGaAs QWs with both front and back gates [Gru00].

A widely used tool to investigate level splitting is the analysis of Shubnikov-de Haas (SdH) oscillations. In the case of spin-split Landau levels a beating pattern can be observed because of the existence of two closely spaced frequency components with similar amplitudes. The amplitude of the SdH oscillations is modulated according to

$$A \propto \cos(\pi\nu), \tag{3.18}$$

where ν is given by

$$\nu = \frac{\delta}{\hbar\omega_c}, \tag{3.19}$$

$\hbar\omega_c$ is the Landau level separation energy and δ is the total energy splitting of each Landau level. Nodes in the beating pattern in the SdH oscillations will occur at half-integer values of ν, where A is zero. In section 3.3 an analysis of the temperature dependence of the node position and in section 5.1 an analysis of the temperature and gate voltage dependences will be presented. The population of the spin-split subbands can be directly determined by a fast Fourier transformation (FFT) of the SdH oscillations as a function of B^{-1}.

---

[3] As the $H1$ band is the conduction band, N_{H1} is often written instead of N_s.

However, another phenomenon can lead to a beating pattern in the SdH oscillations, magneto-intersubband scattering (MIS) from a populated second electronic subband [RNSF01]. Zhang *et al.* have demonstrated, that MIS is absent in type-III HgTe QWs due to the strong non-parabolicity of the conduction bands [ZPJO$^+$02]. They compared temperature dependent SdH measurements of HgTe QWs with two occupied subbands with self-consistent band structure calculations based on an 8×8 $\mathbf{k} \cdot \mathbf{p}$ model (s. sec. 3.1). An important consequence of the absence of MIS is that the Rashba SO splitting can be properly identified from SdH oscillations in a perpendicular magnetic field and at a constant temperature, in contrast to the recent findings on InAs QWs [RNSF01].

3.5 Spin Glass

The DMS $\mathrm{Hg_{1-x}Mn_xTe}$ has two different magnetic ordering phases depending on the temperature T and the manganese concentration x. As shown in Figure 3.8, HgMnTe is in the paramagnetic phase for temperatures above the dashed line for the corresponding manganese content. In the paramagnetic phase, the Curie-Weiss law is obeyed. In the limit of low external magnetic fields or high temperatures, the magnetisation M is linear in an external field B and the magnetic susceptibility χ is defined by $M = \chi B$. Taking antiferromagnetic Heisenberg interaction in the DMS with randomly distributed magnetic moments into account, the expression for χ can be derived to be

$$\chi = \frac{C_0 \mathrm{x}}{T - \Theta(\mathrm{x})}, \tag{3.20}$$

where C_0 is the Curie constant, x the Mn concentration, T the temperature and $\Theta(\mathrm{x})$ the Curie-Weiss temperature. For temperatures below the dashed line in Figure3.8, HgMnTe is in the spin glass phase. The phase transition is accompanied by the appearance of a susceptibility kink. The spin glass can be defined as a random, mixed interacting, magnetic system characterised by a random, yet co-operative freezing of spins at a well-defined temperature T_f (the freezing temperature) below which a highly irreversible, metastable frozen state occurs without the usual long-range spatial magnetic order [Myd93].

A very simple picture which gives a first idea how a spin glass behaves or what glassy state means is the following: Randomly distributed local magnetic moments embedded in a jelly-like environment. This means that the spin and magnetic moment orientation, respectively, can change but with a certain temperature dependent resistance. Due to the antiferromagnetic exchange interaction of the Mn ions in a zinc blende crystal, parts of the spin glass may be “frustrated”. Imagine a triangle with a magnetic moment on every corner. When two moments align antiferromagnetic, the third will be frustrated because it is not possible for it to align antiferromagnetic with each other. This statement is true for all three moments.

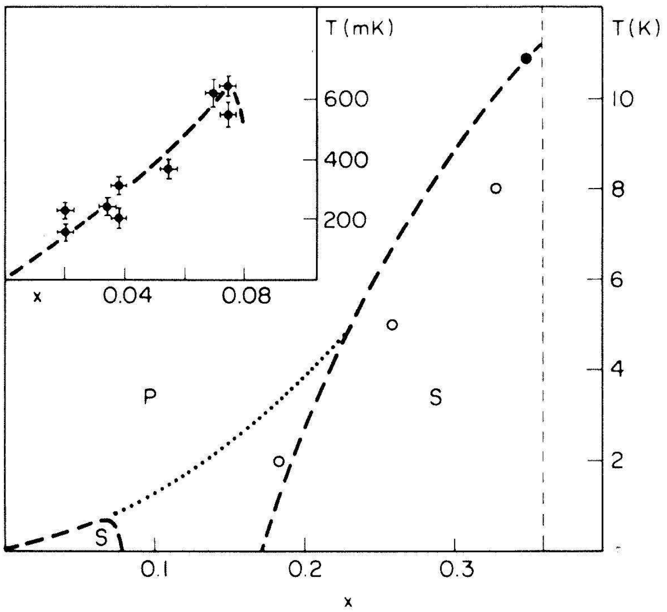

Figure 3.8: Phase diagram of $Hg_{1-x}Mn_xTe$: The magnetic ordering is plotted depending on the Mn content and temperature (from [BM84]). P is the paramagnetic and S the spin-glass phase. The inset shows the magnification of the low temperature part. The open circles are $Hg_{1-x}Mn_xSe$ data from [KAGK81]

For the magnetic exchange interactions several mechanism are known [Myd93]. Next neighbours can couple directly by an overlap of their electronic wave functions from the two sites. The Pauli exclusion principle favours an antiparallel configuration. But due to the exponential decrease of the wave functions with the distance, the exchange integral obtained from the overlap is very small. More important are the longer-range indirect-exchange interactions. The best known is the Ruderman-Kittel-Kasuya-Yosida (RKKY) interaction mediated by the conduction electrons. Embedding a magnetic impurity, i.e., a local magnetic moment, in a sea of conduction electrons with itinerant spin causes a damped oscillation in the susceptibility of the electrons, and thereby a coupling between the spins. The $1/r^3$ fall-off of the RKKY interaction is sufficiently long-ranged so that it can effectively reach a number of nearest-neighbour sites.

Another long-range interaction is the super-exchange [Myd93; Liu03]. In this case an intervening ligand or anion transfers an electron (usually in a p state) to the neighbouring magnetic atom. A sort of covalent mixing of the p and d wave functions occurs with spins pointing in the same direction. Because the two anion

p-spins must be opposite in direction (Pauli exclusive principle), they will cause antiparallel pairing with the d-electrons on the magnetic atoms to the left and to the right. This situation is shown in Figure 3.9 and leads to an antiferromagnetic coupling via the ligand situated between the two magnetic atoms.

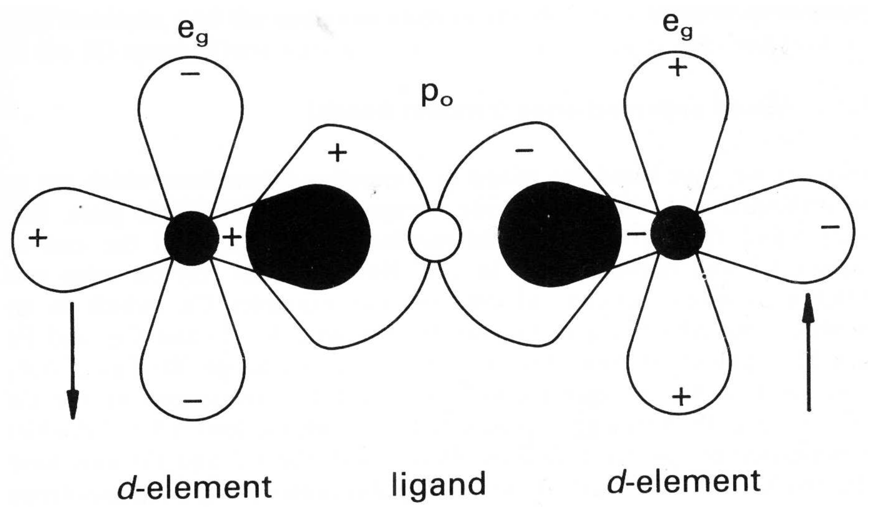

Figure 3.9: Super-exchange between two magnetic d-ions and a p-state ligand. The shaded regions represent the covalent mixing of the different wave functions (from [Myd93]).

The theory of spin glasses is still being developed. The model, which has been explored by Oppermann in the corresponding project (D5) of the centre of excellence (SFB 410)[4] at Würzburg University, is the replica-symmetry-breaking (RSB) or mean-field picture. The RSB picture is based on Parisi's solution [Par83] of the Sherrington-Kirkpatric model [SK75] and its interpretation in terms of a multitude of thermodynamics states [MPS$^+$84]. For further details the reader is referred to [Myd93; KR03] and the references therein.

In order to test models of spin glasses, Altshuler and Spivak [AS86] and Feng *et al.* [FBLM87] have suggested that the sensitivity of quantum interference of scattered electron waves to the instantaneous configuration of the localised spins in mesoscopic systems might serve as an important tool. In nanostructures of Cu:Mn de Vegvar *et al.* observed an unique magneto-fingerprint of the specific frozen spin configuration exploiting the broken time-reversal symmetry of the spin glass state. In particular, an antisymmetric term in the magnetoresistance tensor, generated by the frozen spins, persisted above T_f characteristic for the bulk material [dVLF91].

---

[4] Sonderforschungsbereich

This surprising observation, together with a visible reduction of the Kondo resistivity, was taken as indicative of the importance of magnetic inclusions, such as MnO [Wei92; dVL92].

In mesoscopic spin glasses, universal conductance fluctuations (UCF)[5] will be largely destroyed by spin-flip scattering in the paramagnetic phase above T_f. Below T_f, a dramatic slowing down of the spin glass dynamics should allow the experimental observation of a UCF signal [FBLM87]. In DMS the main coupling mechanism of the localised spins is the short-range antiferrromagnetic superexchange interaction illustrated in Figure 3.9. Nanostructures on HgMnTe therefore should be a suitable probe to examine the spin glass phase by the phenomena of coherent transport. Owing to a large difference between the relevant length scales, such samples are mesoscopic from the point of view of the electronic properties but macroscopic as far as the range of magnetic interactions is concerned. Measurements of a possible phase transition from the paramagnetic to the spin glass phase (Fig. 3.8) will be discussed in section 5.3. Performing measurements on 300 nm thick wires of several μm length on a 300 nm thick CdMnTe film, Jaroszynski *et al.* observed a strong increase of the amplitude of the UCF when the temperature and the magnetic field are reduced below the freezing temperature curve [JWK$^+$98].

3.6 Summary

Mercury based heterostructures exhibit unique properties in contrast to “classical” III-V semiconductors. In the beginning of this section the results of band structure calculations have been presented and the inverted band structure has been explained. The common description of a DMS with the Brillouin function has been introduced and the experiments to obtain the empiric parameters T_0 and S_0 have been presented. The Rashba spin-orbit splitting has been explained, which is at least four to five times larger in Hg-based material as in III-V semiconductors. Finally, the magnetic ordering of a spin glass and the relevant interacions therein have been discussed.

---

[5] introduced by Lee *et al.* [LS85; LSF87]

Chapter 4

Measurements of Nanostructures

As already mentioned in chapter 3, mercury based heterostructures are different from other semiconductor heterostructures. Another, not yet mentioned property of Hg samples is the comparatively low growth temperature of 180 °C. Hence, standard e-beam lithography techniques using polymethylmethacrylate (PMMA) as photo resist could not be applied and a new process had to be developed. This will be described in the initial section of this chapter. Then, experiments on cross-shaped nanostructures will be presented, in which the first ballistic transport in HgTe QWs has been demonstrated. Finally, recent experiments to account for spin-orbit Berry phase on ring shaped structures will be presented.

4.1 Process Development for Nanostructures on HgTe QWs

In standard nanostructuring lithographical processes, PMMA in conjunction with electron beam lithography is used to fabricate such structures. However, for epitaxially grown HgTe samples this is not possible due to the high bake-out temperature necessary for PMMA of about 200 °C. Temperatures exceeding 100 °C cause deterioration of the HgTe QW structures by interdiffusion of well and barrier materials. As an alternative, we have used the photo resist ARU 4060/3 (Allresist). This resist can be used not only for optical but also for electron beam lithographical pattern transfer. The advantage of this resist is the low bake-out temperature. For our samples a bake-out of 2 min at 80 °C was sufficient, which ensures that the sample structures remain unaffected.

The nanostructures have been written using an acceleration voltage of 2.5 kV. First attempts to use the photo resist as an etch mask failed. On the one hand side, dry etching with argon ions in a sputtering machine resulted in adhesion of the resist with the sample. The resist could not be removed, which is essential for the subsequent gate technology that we need for the experiments presented in section 4.3. Furthermore, the sputtering process modifies the underlying nanostructure such that it was not possible to perform transport experiment on these samples. The reason for this modification may be a local over heating which causes a detoriation of the QW as mentioned above. On the other hand side, wet-chemical etching with various etchants resulted in strong, not reproducible under-etching, that made it impossible to control the lateral size of the nanostructures. Therefore, an improved etch mask technology had to be developed. This consisted of titanium masks fabricated in a lift-off process as described in the following.

The positive resist was developed and Ti was evaporated onto the sample. After lift-off, the contact pads were fabricated in an optical lithography step with standard optical photo resist (Microresist ma-P215). Both optical and e-beam patterns were etched in a dilute solution of Br_2 in ethylene glycol at room temperature for 30 s. After etching about 150 nm into the CdTe buffer layer, the resist was removed with acetone and the Ti mask a 2:1 H_2O:HF(50%) solution for 10 s. Ohmic contacts were fabricated by thermal bonding with indium.

This newly developed procedure [DGG$^+$03] provided our first reproducible nanostructured samples on HgTe QWs. Different geometries have been realised, e.g., cross-shaped (sec. 4.2), ring-shaped (sec. 4.3), and micro Hall-bar structures (sec. 5.3). Comparative measurements of the carrier concentration and the carrier mobility on standard Hall-bars and the nanostructures assure us that the sample properties remain unaffected by the nanostructuring process.

4.2 Quasi-Ballistic Transport

HgTe QW structures offer interesting opportunities to study spin related transport effects. One goal is the exploration of the electronic spin behaviour in nanostructures in which transport is dominated by ballistic effects. However, up to now ballistic transport had not been demonstrated in HgTe QW structures, mainly due to specific material properties that prevent the application of well known and established nanostructuring technologies used for Si and GaAs based structures. Furthermore, high mobility HgTe QWs were previously not available. In the time span of this thesis the growth of HgTe QWs had been continously improved. In the beginning, a good sample had a mobility of about 2 to 5 $m^2/(Vs)$. For the samples presented in this section the mobility had already more than doubled. Nowadays, a mobility of 10 $m^2/(Vs)$ is almost standard and the best samples exhibit a value of more than 30 $m^2/(Vs)$.

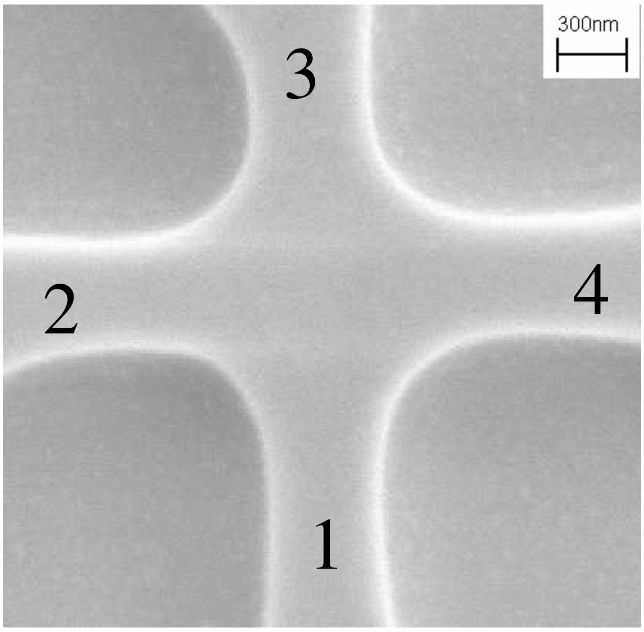

Figure 4.1: Scanning electron microscope photograph of a cross shaped structure with 0.45 μm wide leads

Initially, the designated sample, a n-type asymmetrically modulation doped HgTe QW in the form of a standard macroscopic Hall bar, was characterised in ac and dc measurements in a ^{4}He bath cryostat with a superconducting magnet and fields up to 7 T. A carrier concentration of $1.7 \times 10^{16} m^{-2}$ and a carrier mobility of

6.2 $\mathrm{m}^2/(\mathrm{Vs})$, which corresponds to a Fermi wave vector k_F of $3.27 \times 10^8 \mathrm{m}^{-1}$ and a transport mean free path l_{mfp} of 1.3×10^{-6}m, were used. Concluding from these results, it should be possible to observe ballistic transport effects in devices fabricated from this material with an active area L^2 of less than 1 $\mu\mathrm{m}^2$.

Therefore, nanostructured samples were fabricated which exhibit a cross-shape geometry with lead widths of $\sim$ 1.0 μm and $\sim$ 0.45 μm. A scanning electron microscope (SEM) image of the latter is shown in Fig. 4.1.

Quasi-dc, low frequency (13 Hz) ac measurements with an excitation voltage of 150 μV were carried out in a ^{4}He bath cryostat with a magnetic field perpendicular to the 2DEG using lock-in techniques. Various contact combinations have been used to characterise the sample after the etching process. In the Hall geometry (I: 1→3, V: 2→4, c.f. Fig. 4.1) the carrier concentration was found to be the same as that of macroscopic samples and therefore shows clearly, that the sample properties have not been changed by the fabrication process.

In order to demonstrate that the transport properties are dominated by ballistic effects we have performed non-local transport measurements in different contact arrangements, which previously have been demonstrated in high mobility GaAs nanostructures [MSB$^+$90; HBGM98]. One of the most prominent effects is the non-local *bend* resistance (NLR). This signal is measured by passing current through contacts 1 and 2, while the voltage is measured between contacts 3 and 4 (see Fig. 1.5 and Fig. 4.1). The bend resistance is obtained simply by dividing the voltage $V_{3,4}$ by the injected current $I_{1,2}$. If the transport were dominated by diffusive scattering, no voltage signal would be expected to appear between contacts 3 and 4 in this geometry, whereas in the ballistic regime, electrons injected from contact 1 into the cross reach the opposite channel before they are scattered. This leads to charge accumulation at contact area 3 and thus to the NLR signal. Applying a small magnetic field perpendicular to the 2DEG plane deflects the ballistic electrons and the voltage signal between 3 and 4 decreases.

The result for the 0.45 μm cross is shown in Fig. 4.2. The NLR signal is indeed observed, which is direct evidence of ballistic transport in this device. As expected, the signal exhibits a pronounced maximum around $B = 0$. With an applied field the signal decreases, exhibiting a large dip with a negative NLR signal before it approaches zero in the high field range ($B > 2$ T). This behaviour of the NLR signal can be qualitatively understood by applying the Landauer-Büttiker (LB) formalism. In our geometry the resulting NLR is derived according to

$$R_{12,34} = \frac{V_{34}}{I_{12}} = \frac{h}{2e^2} \frac{T^2 - t_r t_l}{(t_r + t_l)(2T^2 + 2(t_r + t_l)T + t_r^2 + t_l^2)}, \tag{4.1}$$

where T, t_l and t_r are the corresponding transmission probabilities as already defined in Equation (1.23).

Comparing the results of Eq. (4.1) with the data presented in Fig. 4.2, one can see that at zero magnetic field the NLR signal is dominated by electrons that travel

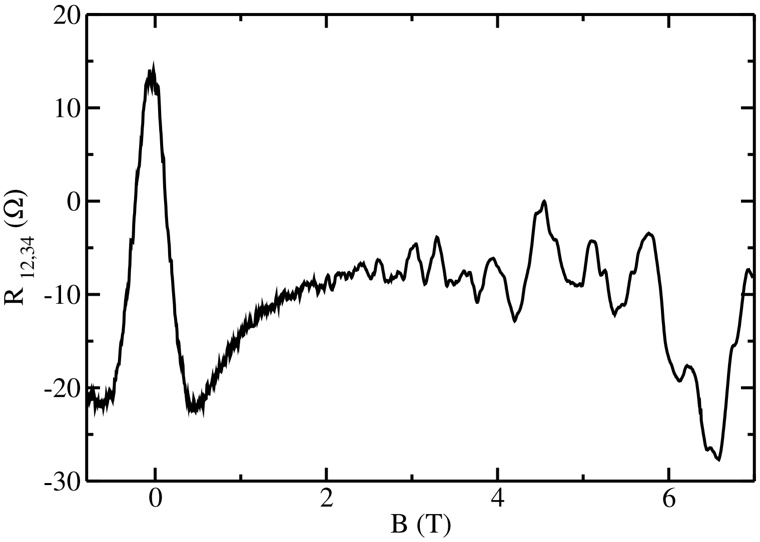

Figure 4.2: Non-local resistance signal $R_{12,34}$ for the structure with 0.45 μm wide leads.

ballistically from contact 1 to 3 (T^2, Eq.(4.1)). This signal is reduced by electrons which reach either the left or right contact ($t_r t_l$, Eq.(4.1)). At zero magnetic field this corresponds to electrons that are either injected outside the acceptance angle of contact 3 or are scattered by unintentional impurities. In a magnetic field the electrons are deflected due to the Lorentz force either toward the left or the right contact depending on the field direction, which implies that the NLR should decrease and approach zero, i.e., $T = 0$ and, either $t_l = 0$ or $t_r = 0$. However, due to the boundary scattering processes mentioned above, an intermediate field regime exists where the signal becomes negative. In this regime rebound trajectories (see Fig. 1.5, right) may cause the product $t_l t_r$ to exceed T^2 [HBGM98]. Enlarging the B field further will *guide* all electrons to only one contact ($T^2 \rightarrow 0$ and, either $t_r \rightarrow 0$ or $t_l \rightarrow 0$) and the NLR becomes zero.

In Fig. 4.2 one can see that in the regime where $R_{12,34}$ is expected to approach zero, Shubnikov-de Haas oscillations, which are not included in Eq. (4.1), are superimposed on the signal. However, the ratio of the absolute magnitude of the positive signal at $B = 0$ and the largest negative value is rather small compared to the published results for high mobility GaAs structures [MSB$^+$90; HBGM98; Tim92]. The main reason for this difference is the comparatively short mean free path, which is of the order of the device dimensions in the present case. Therefore, it is plausible that random scattering in the cross area increases the transmission probability to contacts 2 and 4, leading to a reduction in the NLR signal at zero

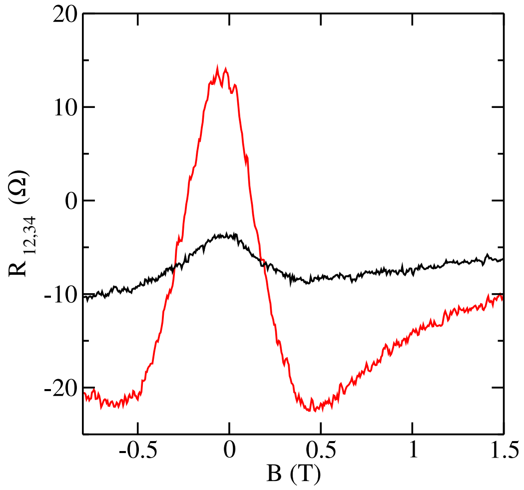

Figure 4.3: Non-local resistance signal (NLR) for structures with lead widths of 1.0 μm (black curve) and 0.45 μm (red curve). The red curve is part of the curve shown in Fig. 4.2.

magnetic field.

This effect is also observed, when the device size is increased; the NLR signal for the 1.0 μm structure is much smaller than that for the 0.45 μm structure, as shown in Fig. 4.3. In a first approximation the ratio of the signal for these two structures can be used to estimate the carrier mean free path in the cross area. The signal is proportional to the number of electrons that reach contact 3 ballistically ($\propto \exp(-L/l_{mfp})$) reduced by those electrons that are scattered into the contacts 2 and 4 ($\propto 1-\exp(-L/l_{mfp})$). Evaluating the values deduced from Fig. 4.3, $l_{mfp} \approx$ 1.2 μm is obtained which is in good agreement with the average mean-free path for the macroscopic sample.

Further evidence for transport in the ballistic regime provide the measurements in the three-terminal configuration and the Hall geometry as shown in Fig. 4.4. In the left part of the figure the resistance $R_{12,34}$ is plotted versus the perpendicularly applied magnetic field. The red curve shows the experimental data of a three-terminal configuration, which means that the setup is the same as described above, but contacts 2 and 4 are grounded, and therefore, their potentials are identical. The black curve shows again the four-terminal NLR data for comparison. As expected from Eq. (1.24), the three-terminal data show a pronounced maximum around $B=0$ and are always positive. The relatively large background of about 690 Ω could be a hint for enhanced scattering (not purely ballistic) effects discussed below. In the right part of Fig. 4.4 the resistance $R_{13,24}$ in the Hall geometry is shown. Hereby, the current is driven from contact 1 to 3 and the voltage is measured between contacts 2 and 4. As one can see, the experimental curve shows a clear deviation from a straight line, a phenomenon called the anomalous Hall effect. To emphasise this effect the difference between the measured Hall resistance and the straight

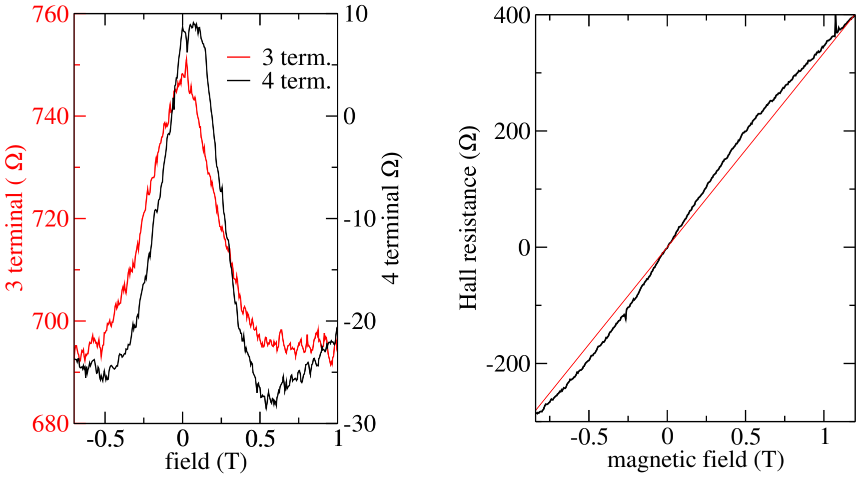

Figure 4.4: Left: Three-terminal measurement of the NLR (red curve) and corresponding four-terminal measurement (black curve). Right: Hall resistance measurement. The straight line (thin) is only a guide to the eye.

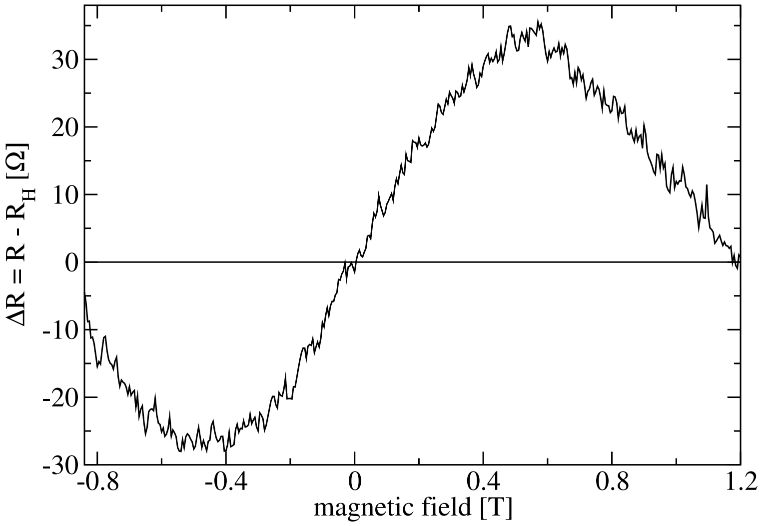

Figure 4.5: Anomalous Hall effect in the cross-shaped structure. From the measurement data in the right panel of Fig. 4.4, the straight Hall line is subtracted.

Hall line is shown in Figure 4.5. This deviation is largest in the regime where the transmission probabilities t_l and t_r are of the same order of magnitude as expected from Eq. (1.25). When t_l and t_r are similar, negative dips appear in the four-terminal NLR due to the rebound trajectories.

In order to put these considerations into a more quantitative basis we have used a MC simulation of the classical electron trajectories in which electrons with an arbitrary velocity distribution are injected from contact 1 into the cross. In this model the electrons are then specularly reflected at the sample boundaries. Hereby, the boundaries are assumed to have a graded potential $\propto \frac{1}{x}$. The boundary reflection is simulated as illustrated in Figure 4.6. The velocity component $v_\perp$ of the impinging electron perpendicular to the wall is decelerated between W_{min} and W_{max} to zero. Then the electron is specularly reflected, accelerated and leaves W_{min} with -$v_\perp$. The velocity component parallel to the wall remains unaffected. The slope of the potential allows electrons with the maximum $v_\perp$ to reach W_{max}. The electrons that reach the individual contacts are counted. This number is proportional to the corresponding transmission probability [HBGM98; BvH90].

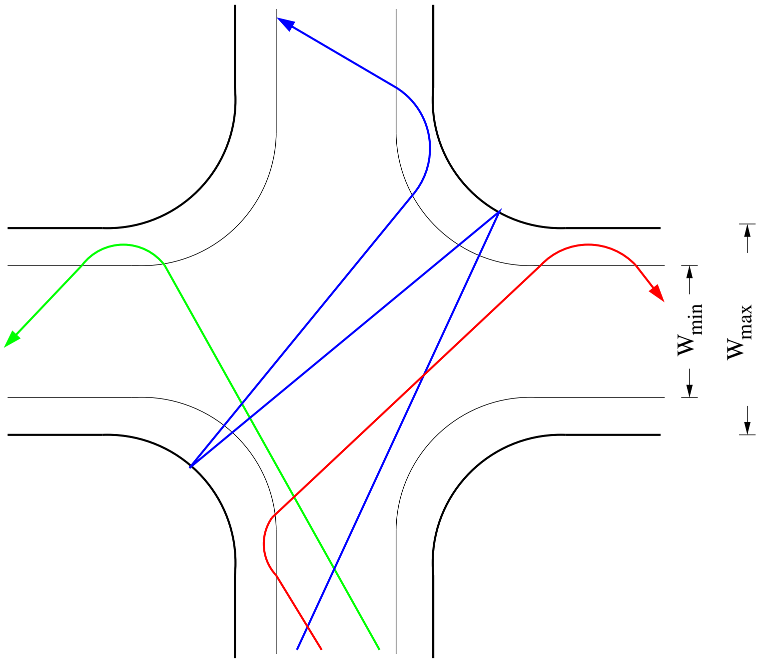

Figure 4.6: Classical MC simulation of electron trajectories.

Unfortunately, only a qualitative agreement with our measurement data could be achieved. Hence, we concluded that the experimental results can not be fully explained by purely ballistic transport and boundary scattering. From the measurements (Fig. 4.3) one observes that the signal exhibits additional fine structure which is not induced by electronic noise. This fine structure is fully reproducible and stable over time provided the sample is kept at low temperatures. We identify the fine structure as universal conductance fluctuation (UCF), which is caused by electronic interference effects due to the random distribution of scatterers within the cross area. Detailed temperature dependent studies of the UCF in these and other structures are presented in section 5.3.

Consequently, we have introduced randomly distributed, locally fixed scatterers with dimensions on the order of the Fermi wave length λ_F in the MC simulation. The scatterers are assumed to have a cone-shaped geometry with a $\frac{1}{x}$-flank and an outer and inner radius R and r, respectively. In the two-dimensional projection these are two concentric circles. The scattering event is simulated similar to the boundary scattering. The perpendicular velocity component of the impinging electron is decelerated to zero between R and r. After the reflection at the tangential plane of the inner radius, the electron leaves the outer radius again with the same magnitude as that of the incoming velocity. The scattering time τ, which is related to the transport mean free path, is used as an adjustable parameter. Examples of trajectories for three different τ are shown in the left part of Figure 4.7. In the right part of the same Figure two sets of simulated data are presented. In the upper panel of the figure the results for the three-terminal and in the lower panel for the four-terminal configuration are shown. The introduction of scatterers as described above leads to a significant reduction of the ratio R_{max}/R_{min}, but good quantitative agreement is still not achieved.

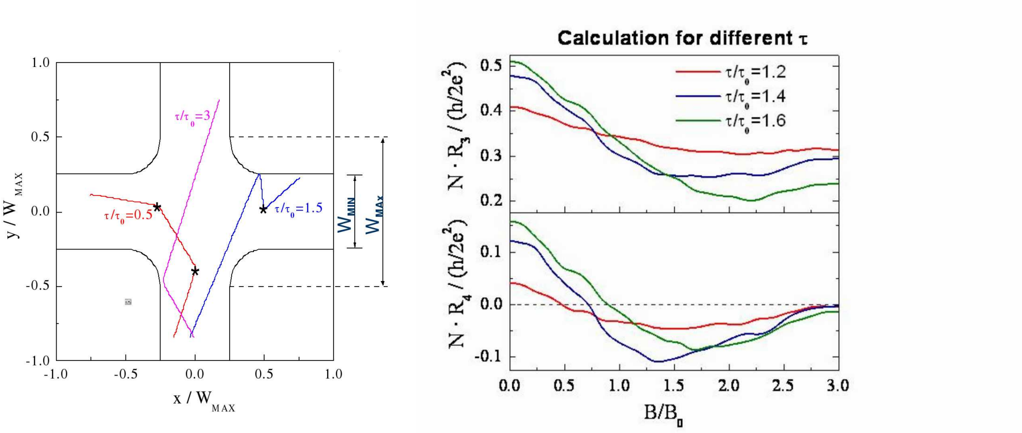

Figure 4.7: Left: Electron trajectories for different τ. Right: MC simulations with different scattering times τ for the three-terminal (upper panel) and the four-terminal configuration (lower panel).

Hence, we concluded that the scattering mechanisms are more complex. Electron-phonon scattering can be excluded due to the low temperatures at which the measurements are performed. According to the relatively high dislocation/stacking fault density in HgTe of about 10^6 cm^{-2} [Dau99], it is not possible to propose a discrete scatterer arrangement concerning locations and sizes as well as potential heights. Therefore, we have introduced a random scattering process, i.e., the ballistic propagation is altered randomly for electrons that dwell longer than the scattering time τ in the cross area. Whereas the experimental measurement is the realisation of one possible scatterer configuration, the MC simulation includes random scattering averages over all possible configurations. Thus, the experimental curve shows the characteristic UCF pattern and the simulated curve is smooth.

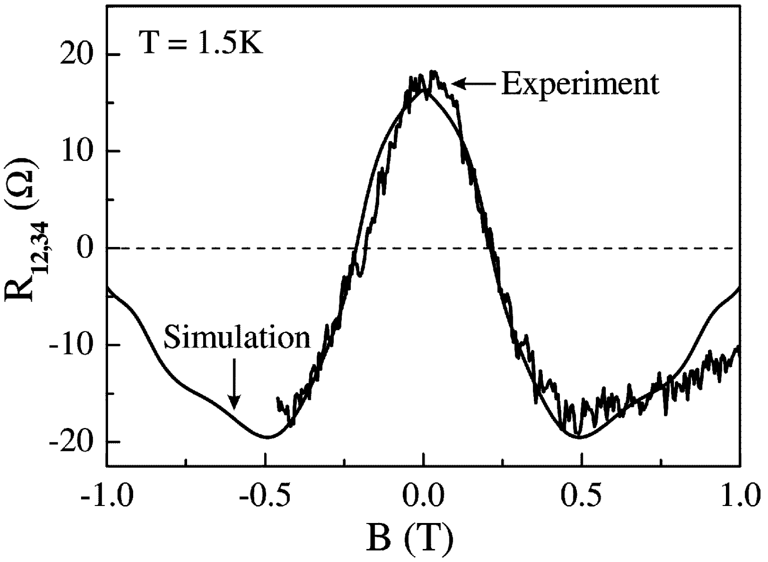

Figure 4.8: Experimental data for a 0.45 μm device together with the Monte Carlo simulation result (smooth curve) for a scattering time of $\tau = 1.1 \times 10^{-12}$ s.

Fig. 4.8 shows the resulting NLR curve. For a scattering time of $\tau = 1.1 \times 10^{-12}$ s good agreement with the experimental data is obtained. This value implies a mean free path of ≈ 0.9 μm and agrees well with the $\tau = 1.6 \times 10^{-12}$ s ($\Rightarrow l_{mfp} = 1.3$ μm), obtained from the macroscopic transport measurements and the value deduced from the peak height ($l_{mfp} = 1.2$ μm) discussed above. These results demonstrate that for the given device dimensions, electrons either reach the contacts ballistically or are scattered randomly. This implies that transport in these structures is in the transition regime between ballistic and diffusive transport, which is usually referred to as quasi-ballistic transport.

In Figure 4.9 the transmission probabilities T, t_l and t_r at $B = 0$ are plotted for different scattering times τ. For $\tau/\tau_0 < 1$, transport is in the diffusive regime where

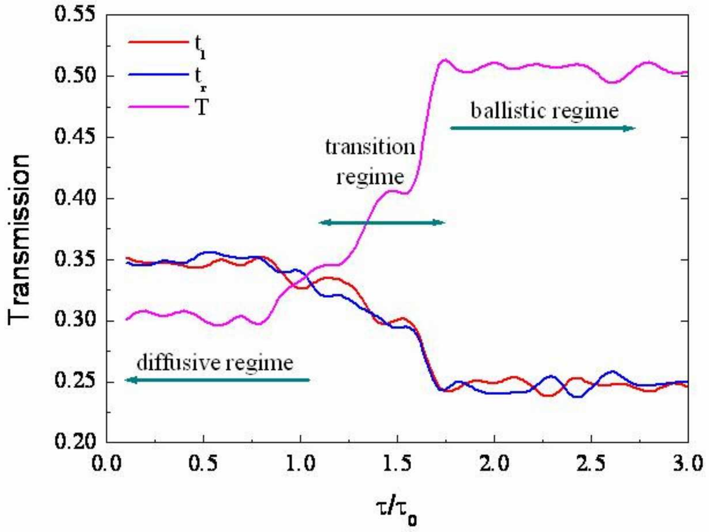

Figure 4.9: Transmission probabilities T, t_l and t_r at $B = 0$ for different scattering times τ. Two regions where the transmission probabilities are constant can be identified: $\tau/\tau_0 < 1$, the diffusive regime and $\tau/\tau_0 > 1.7$, the ballistic regime. The intermediate region is the transition regime between those two.

only 30% of the injected electrons reach contact 3 (T). With an increasing τ/τ_0 ratio more and more electrons reach contact 3 and for $\tau/\tau_0 > 1.7$ the transmission probability T saturates and the transport is purely ballistic. The initial parameter τ_0 is the maximum length in the cross area divided by the Fermi velocity. For the sample in question $\tau_0 \approx 7 \times 10^{-13}$ s was calculated. With the above introduced value of $\tau = 1.1 \times 10^{-12}$ s, the best agreement between experiment and simulation resulted in a ratio of $\tau/\tau_0 = 1.57$. This result shows again, that the transport is in the transition regime with a small diffusive component, i.e., quasi-ballistic transport.

In conclusion, we have presented evidence for quasi-ballistic transport in high mobility HgTe QW nanostructures which are fabricated with a technology that overcomes the specific problems of Hg containing devices [DGG^{+}03]. Furthermore, a quantitative analysis of the non-local resistance measurements revealed that the actual HgTe QW nanostructure samples permit a detailed study of the transition from a diffusive to a local ballistic transport regime.

4.3 Transport in Rings

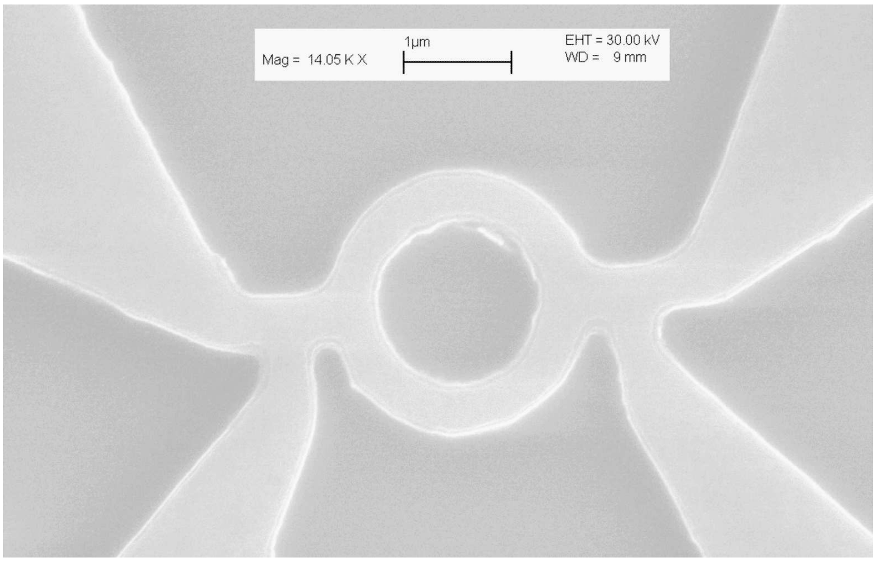

Figure 4.10: SEM photograph of a ring shaped structure with a radius of 1 μm

After the successful development of a fabrication process for nanostructures, which has been demonstrated in the last section with the cross shaped structure, more complex structures were the goal. As introduced in section 2.5, the theoretically predicted SO Berry phase has not been observed experimentally. One possible experimental setup, in which the SO Berry phase could be detected, are Aharonov-Bohm (AB) rings in semiconductors with a strong Rashba spin splitting [ALG93; EL00]. Hence, HgTe QWs with its large, tunable Rashba splitting are good candidates for the direct observation of the SO Berry phase. To resolve AB oscillations, ring shaped structures with a small radius r must be fabricated. The period of the oscillations as a function of the magnetic field can be calculated using Eq. (2.1). One full oscillation results, if the enclosed magnetic flux $\Phi = B \cdot \pi r^2$ is incremented by one magnetic flux quantum $\Phi_0 = h/e$. Thus, the condition of at least ten data points per oscillation in a magnet with steps width of 0.1 mT requires a radius of

$$r = \sqrt{\frac{h}{\pi e B}} = \sqrt{\frac{6.626 \times 10^{-34}\ \mathrm{Js}}{\pi \cdot 1.602 \times 10^{-19}\ \mathrm{As} \cdot 1 \times 10^{-3}\ \mathrm{T}}} = 1.15 \times 10^{-6}\ \mathrm{m}. \qquad (4.2)$$

The implementation of the nanofabrication process described above allowed us to define lateral structures with a width of some hundred nanometers with high reproducibility. The problem with the lithographic patterning of ring shaped structures with a radius of 1 μm was to remove the Ti inside the ring by the lift-off process. After many failures with partly removed or re-attached inner parts of the ring during the standard lift-off process, we succeeded with a short ultra sonic bath in acetone. The result is shown in the SEM photograph in Fig. 4.10. Here, a ring shaped structure with a radius of 1 μm and an arm width of 300 nm is shown. Low temperature (below 100 mK), four terminal resistance measurements exhibit clear AB oscillations as depicted in Fig. 4.11. For a radius of 1 μm a period of 1.3 mT can be calculated, which corresponds to a frequency f_0 of 760 T^{-1}. The period can be extracted directly from the oscillations in the left part of the Figure and the frequency can be found in the corresponding FFT in the right panel on side. The FFT exhibits additional smaller peaks around $2f_0$ and $3f_0$ which correspond to electrons that aquire $2\Phi_0$ and $3\Phi_0$, respectively. The $2f_0$ peak is from electrons that make one circuit of the ring and the $3f_0$ peak is from those which have made 1.5 circuits. The probability of coherent transport decreases with an increase in the path length which is reflected in the peak heights.

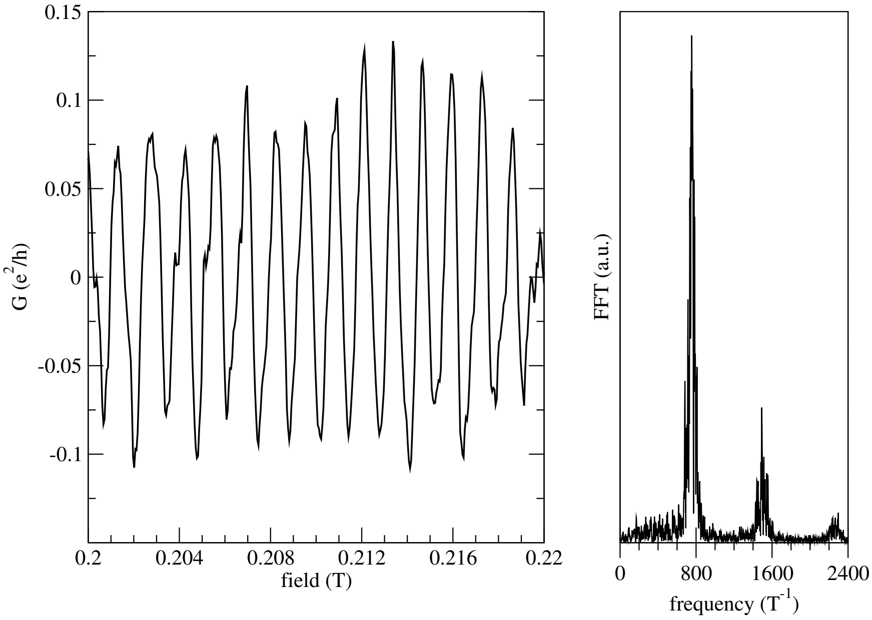

Figure 4.11: Left: Measurement of Aharonov-Bohm oscillations in a ring shaped structure with a radius of 1 μm. The conductance is plotted as a function of the magnetic field. Right: Corresponding FFT.

The fabrication of these structures was the first milestone in the search for the SO

Berry phase. Due to the Rashba effect, curves such as that depicted in Fig. 4.11 exhibit a SO Berry phase; however, proof requires that the contribution of the Rashba SO splitting has to be determined by varying its magnitude. Therefore an altered structure is needed. An additional Schottky gate on top of the ring is required in order to control the inversion asymmetry of the underlying heterostructure and hence, the Rashba splitting. Again the standard technology, which was improved for the fabrication of top gates on standard Hall bars, failed. Several adhesion and leak current problems had to be solved. We have developed a process with the recently acquired plasma enhanced chemical vapour deposition (PE-CVD) machine. In contrast to the previously used thermal evaporated insulator Al_2O_3, the compound materials SiO_2 and SiN in connection with a new deposition method were now available. The use of only one of these two materials resulted in adhesion problems due to stress originated cracks during the subsequent gate structuring process. This stress could be reduced by an alternating deposition of SiO_2 and SiN. Five double layers with a total thickness of 80 nm provided an insulator with leak currents of only some pA while applying a 10 V gate voltage. A fully processed ring shaped structure with PE-CVD multilayer insulator and thermal evaporated metal gate is shown in the optical micrograph in Fig. 4.12. The underlying ring structure with the leads is visible due to an enhanced height contrast.

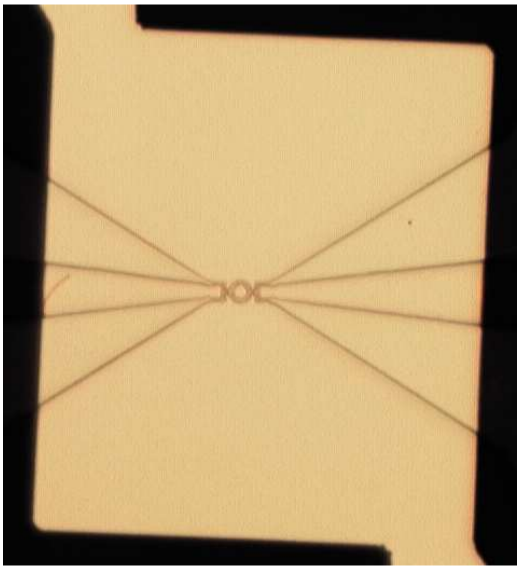

Figure 4.12: Optical microscope photograph of a ring shaped structure ($r = 1\ \mu$m) with gate on top. The underlying ring structure is visible due to an enhanced height contrast.

AB oscillations, identical to those depicted in Fig. 4.11, could be resolved also in this structure. The effect of the top gate is demonstrated on Aharonov-Casher (AC) oscillations (c.f. sec. 2.3). Analoguous to the AB effect, an applied perpendicular electric field leads to oscillations in the resistance. In Fig. 4.13 the conductance is plotted as a function of the gate voltage. The red and black curves represent two separate measurements which demonstrated the experimental reproducibility. The amplitude of the oscillations is on the order of one conductance quantum (e^2/h). The reduction of charge carriers with increasing gate voltage results in a decrease of the mean conductance. This is clear evidence of a successfully prepared sample

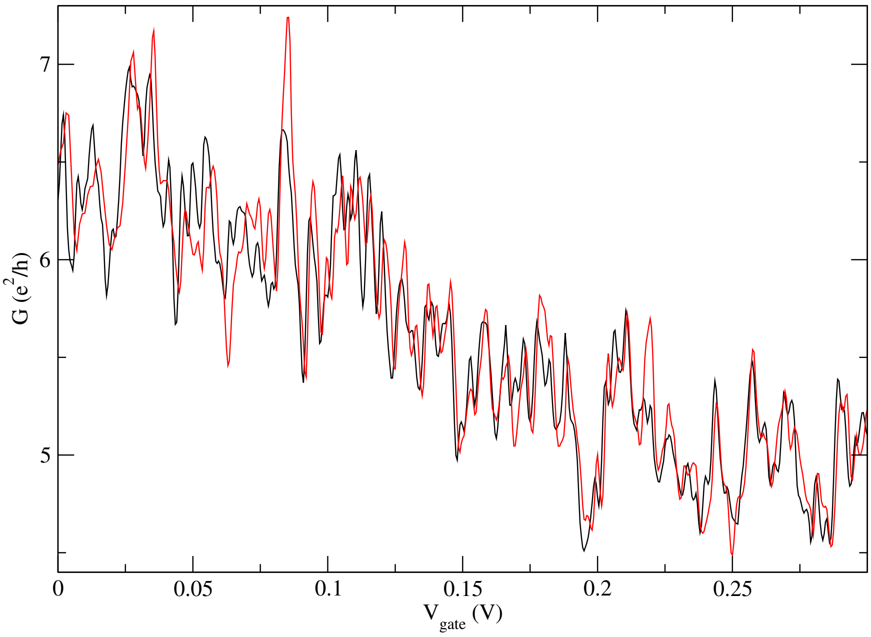

Figure 4.13: Measurement of Aharonov-Casher oscillations in a ring shaped structure with a radius of 1 μm by applying a gate voltage perpendicular to the plane of movement. The red curve is a repeat measurement of the black curve to show the reproducibility.

which permits us to search for the SO Berry phase. Hence, we measured the AB oscillations (as a function of magnetic field) for various gate voltages. The result is shown as a contour plot in Fig. 4.14. The magnetic field and the applied gate voltage are on the x-axis and y-axis, respectively. The maxima and minima of the oscillations are bright and dark, respectively. Cross section lines parallel to the x-axis are AB oscillations for one particular Rashba splitting. A comparison with the theoretical plot of the SO Berry phase in Fig. 2.4 suggests the assumption that this is the first direct observation of SO Berry phase. Also the experimental data exhibit a clear phase change from maximum to minimum and vice versa with increasing Rashba splitting (along the y-axis). Theoretical calculations of the SO Berry phase demonstrate that the adiabacity criterion has to be fulfilled [EL00], i.e., the Lamour

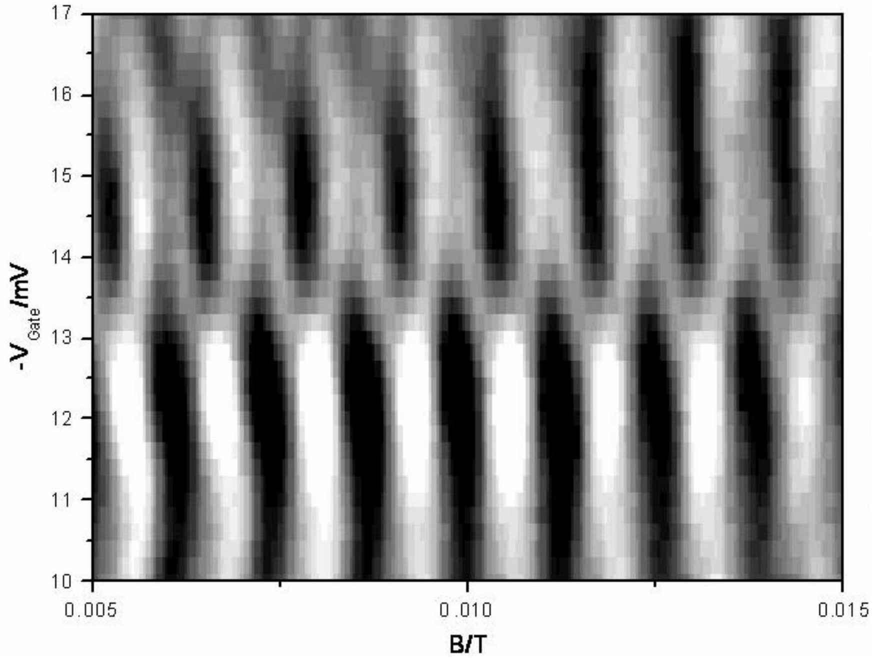

Figure 4.14: Contour plot of AB oscillations as a function of magnetic field (x-axis) and applied gate voltage (Rashba splitting, y-axis).

frequency ω_L of the spin precession must be much larger than the frequency ω_r of the cyclic movement in the ring. Using the corresponding equations in Ref. [EL00] leads to a value of the internal (Rashba induced) field of about 1 T. One may argue that the Rashba splitting even in this low gate voltage range is large enough, but to observe the phase change, the internal and external (magnetic) field must be of the same order. Therefore, measurements in an extended field range have been performed. In Fig. 4.15 a similar contour plot for magnetic field values of ~1 T is depicted. One can identify several, separated regions, where a phase change appears. The interpretation of this plot is quite complex. In contrast to the simplest case, depicted in Fig. 2.4, the heavy hole character of the charge carriers has to be taken into consideration. For $|\pm 3/2\rangle$ states, the SO Berry phase is $3\pi(1-\cos\Theta)$, which results in phase changes of an odd number of π[1]. The relation between the applied gate voltage and the Rashba splitting energy in the nanostructure could not be determined due to the lack of SdH oscillations even in high field measurements. Furthermore, transport in the described samples is a multi-mode transport which may result in many-particle interference effects.

Initiated through these promising, measurements numerical calculations which

---

[1] in contrast to $\pi(1-\cos\Theta)$ for $|\pm 1/2\rangle$ states, which results only in a phase change of π

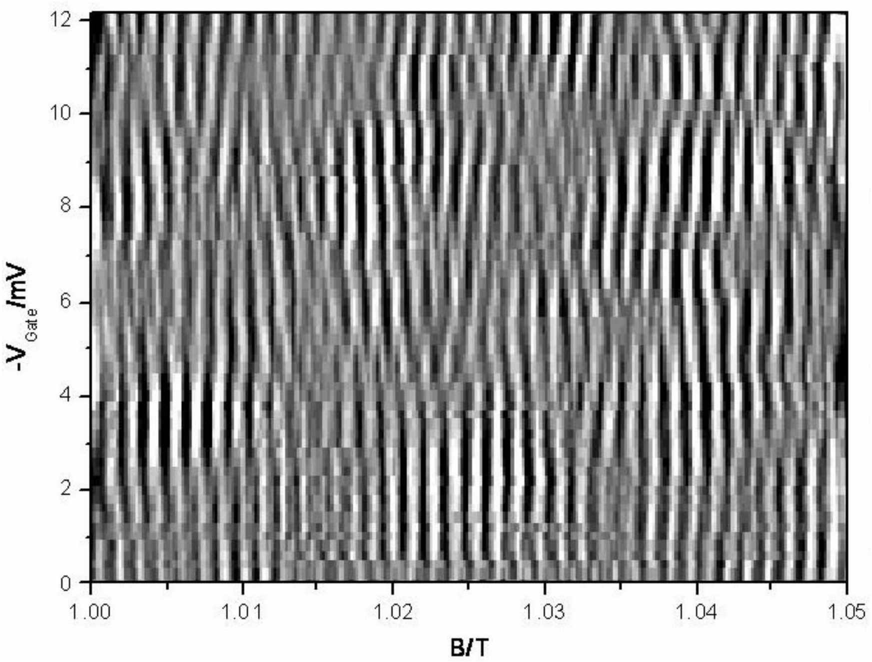

Figure 4.15: Contour plot of AB oscillations as a function of magnetic field (x-axis) and applied gate voltage (Rashba splitting, y-axis).

include sample specific parameters, e.g., band structure, have been initiated by means of a collaboration with the group of A.H. MacDonald in Austin, Texas. The results are still forthcoming and will be presented elsewhere. For future experiments, which exceed the scope of this thesis, new structures are suggested. To determine the Rashba splitting, a micro Hall bar should be connected on one side of the ring. Then it should be possible to resolve SdH oscillations in the longitudinal resistance of the Hall bar. The influence of the gate induced SIA, i.e., the Rashba splitting, can then be directly determined.

4.4 Summary

In this section, the development of nanostructures fabricated from HgTe QWs that overcome the Hg specific processing problems, was presented. In cross shaped structures with lead widths down to 0.45 μm, evidence for quasi-ballistic transport was demonstrated. Transport measurements in ring shaped structures exhibit clear Aharonov-Bohm oscillations. With an additionally developed gate technology applied on these rings, it was possible to account for the Aharonov-Casher effect. A first hint, that the previously not directly observed SO Berry phase could be experimentally verified in such structures was found. With the proof of phase coherent transport in the exceptional Hg based material a wide field of fundamental as well as spintronics relevant research has been opened. Further experiments on phase coherent transport in nanostructured HgTe and HgMnTe QWs will be given in section 5.3, where the universal conductance fluctuations will be analysed.

Chapter 5

Measurements on $Hg_{1-x}Mn_xTe$ Quantum Wells

In this chapter some unique features of HgMnTe QW samples will be described. First, the separate investigation of the Rashba and giant Zeeman splitting in one and the same sample will be demonstrated. The next section is dedicated to an extraordinary sample which exhibits the $\nu = 1$ quantum Hall plateau from below 1 T up to 28 T whose origin was unknown so far. In the last section of this chapter experiments are presented which open the possibility to use the magnetic 2DEG in these samples as a probe for the magnetic ordering in the sample. Evidence for a phase transition from the paramagnetic to the spin glass phase will be given.

5.1 Interplay of Rashba, Zeeman and Landau Splitting

After the assignation of the parameters S_0 and T_0 in the general chapter 3, that are essential for the description of the DMS HgMnTe, we can now focus on the investigation of a magnetic 2DEG formed by a HgMnTe QW. With the inclusion of Mn in a gated QW we are able to analyse two different effects in one sample independently [GBL$^+$04]: the (only) temperature dependent Zeeman effect caused by the strong $sp-d$ exchange interaction between the conduction electrons and the Mn ion spins [GLO$^+$01] and the (only) gate voltage dependent Rashba effect due to the structure inversion asymmetry (SIA) [ZPJO$^+$01; GLD$^+$02]. The giant Zeeman effect in these structures leads to spin splitting energies, ΔE_s, of tens of meV, which are comparable to or larger than the Landau level (LL) splitting, $\hbar\omega_c$, and also the Rashba SO splitting is of a similar magnitude.

A widely used tool to explore level splitting is the analysis of SdH oscillations as introduced in section 1.3. Level splitting causes a beating pattern in the SdH oscillations due to the existence of two closely spaced frequency components with similar amplitudes. These beating patterns show characteristic of both Zeeman splitting (dependence on temperature) and Rashba splitting (dependence on gate voltage). Magneto intersubband scattering (MIS) [RNSF01] can be excluded for our samples as discussed in section 3.4.

One of the main attentions in the analysis is focused on the modulation of the SdH amplitude

$$A \propto \cos(\pi\nu), \tag{5.1}$$

where ν is given by

$$\nu = \frac{\delta}{\hbar\omega_c}, \tag{5.2}$$

$\hbar\omega_c$ is the LL separation energy and δ is the splitting of each LL. Nodes in the in the beating pattern in the SdH oscillations will occur at half values of an odd integer of ν, where the amplitude A is zero. In Figure 5.1 SdH oscillations of the HgMnTe QW, Q1697, at a fixed gate voltage as a function of temperature are shown. On the right hand side of the same Figure the corresponding fast Fourier transformations (FFT) of the SdH oscillations as a function of $1/B$ are plotted. A double peak structure is clearly resolved in the FFT spectra. The two peaks correspond to the two spin-split components of the first conduction band $H1$. Depending on the gate voltage the total charge carrier concentration can be varied from 2.7 to 3.6×10^{12} cm^{-2}. A gate voltage of 2.0 V corresponds to a carrier concentration of 3.1×10^{12} cm^{-2}. Here, in the higher carrier concentration range, three nodes can be observed which are indicated with arrows. These nodes show a large temperature shift which is caused by the strong $sp-d$ exchange interaction discussed in the section above. The origin of the temperature dependence lies in the reduction in magnetisation of the Mn ions with increasing temperature. Similar

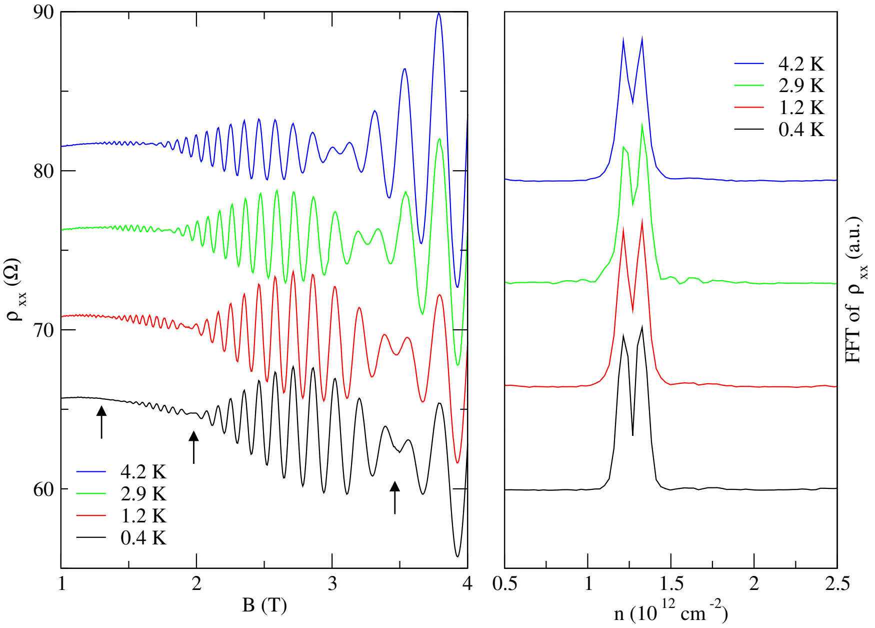

Figure 5.1: SdH oscillations of the HgMnTe QW, Q1697, at a fixed gate voltage as a function of temperature. Node positions in the beating patterns are indicated with arrows. On the left side the corresponding FFT of the SdH oscillations as a function of $1/B$ are shown. All traces are shifted vertically for clarity.

to the analysis of the node position introduced for HgMnTe bulk material in the section above, the Zeeman splitting energies are deduced here. In the phenomenological description of a DMS with the Brillouin function (c.f. sec. 3.2) the effective g-factor g^* can be expressed as

$$g^* = g_0 - \frac{(\Delta E)_{max}}{\mu_B B} B_{\frac{5}{2}} \left[\frac{5 g_{Mn} \mu_B B}{2 k_B (T + T_0)} \right], \tag{5.3}$$

where $(\Delta E)_{max}$ is the saturated spin splitting energy caused by the $sp-d$ exchange interaction and g_0 is the g-factor for a HgTe QW without the presence of Mn, i.e., $g_0 = -20$ [ZOPJ$^+$04]. The remaining parameters are already introduced in Equation (3.7).

An experimental estimate for $(\Delta E)_{max}$ can be obtained from the results displayed in Figure 5.2, where the differences in experimental level splitting energies, δ, between 0.38 K and temperature T are plotted versus the LL splitting energy, $\hbar\omega_c = \hbar(e/m^*)B$. The electron effective mass employed here has been determined by means of self-consistent Hartree calculations described in section 3.1. We find $m^* = 0.047$ to $0.051\, m_0$ for the carrier concentrations observed in the experiments,

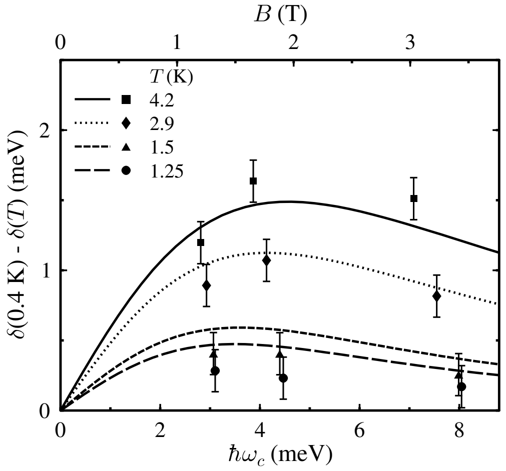

Figure 5.2: Experimental values of the difference in level splitting energies, δ, between 0.38 K and the temperature T versus the Landau level splitting energy with $V_g = 1.0$ V. The curves are the results of a least square fit of values of $g^* \mu_B B$ by means of Eq. (5.3)

i.e., the population of the first conduction band $H1$ is $n_{H1} = 2.2$ to 2.6×10^{12} cm^{-2} for V_g between -3.75 and $+4.75$ V. The curves in Fig. 5.2 are results of least square fits of Eq. (5.3) at the corresponding temperatures. The agreement is reasonable and results in $(\Delta E)_{max} = 4.3 \pm 0.5$ meV and $T_0 = 2.6 \pm 0.5$ K. In principle, these parameters depend only on the Mn composition.

However, the giant Zeeman effect can not explain why the observed nodes also shift with gate voltage, i.e., the asymmetry of the QW structure, as can be seen in Fig. 5.3. This behaviour is typical for level splitting due to the Rashba SO component, as was discussed for non-magnetic HgTe quantum wells by Zhang *et al.* [ZPJO$^+$01]. In the right part of Fig. 5.3 the corresponding FFT of the SdH oscillations as a function of $1/B$ are shown. Again, a double peak structure is resolved. As mentioned above, the carrier concentration of the spin-split $H1$ can be determined from the FFT spectra. The results are presented in Fig. 5.4. Here, the population difference $\Delta n_{H1}/n_{H1}$ is plotted versus the total carrier concentration. The line are the theoretical values obtained from self-consistent Hartree calculations. In the inset the corresponding Rashba SO splitting energies, Δ_R, which are extracted from the values of $\Delta n_{H1}/n_{H1}$ by means of band structure calculations, are shown.

While the carrier concentration of $H1$ changes only from 2.24 to 2.65×10^{12} cm^{-2} in the accessible gate voltage range, the node at the highest field in Fig. 5.3 shifts from 2.25 T ($V_g = -3.75$ V) to 3.72 T ($V_g = 4.75$ V). Concurrently the calculated Rashba SO splitting energies, Δ_R, change from 5 meV to 13 meV. Δ_R magnitudes of up to 13 meV are greater than that of Zeeman and Landau level splitting for magnetic fields up to approximately 4 to 5 T. Although, the sample was designed to be symmetrical, it was not possible within this voltage range to eliminate the inherent asymmetry, i.e., to tune the Rashba splitting to zero. One reason can be

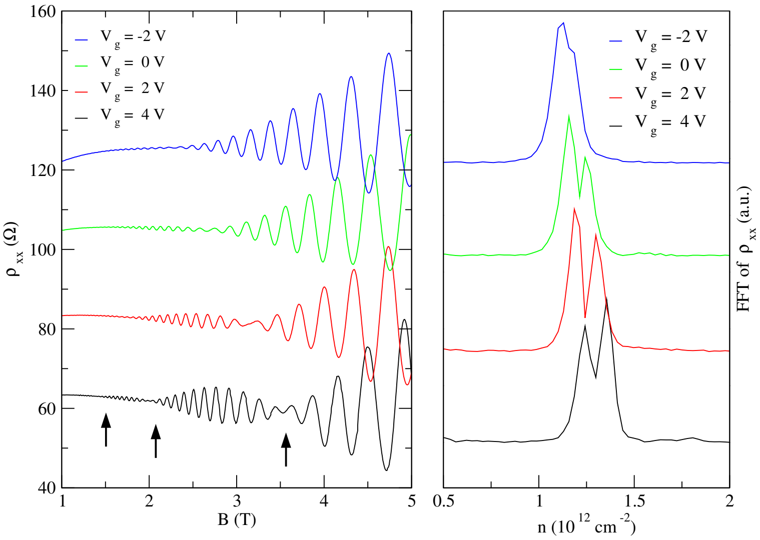

Figure 5.3: SdH oscillations of the HgMnTe QW, Q1697, at $T = 0.38$ K as a function of gate voltage. Node positions in the beating patterns are indicated with arrows. On the left side the corresponding FFT of the SdH oscillations as a function of $1/B$ are shown. All traces are shifted vertically for clarity.

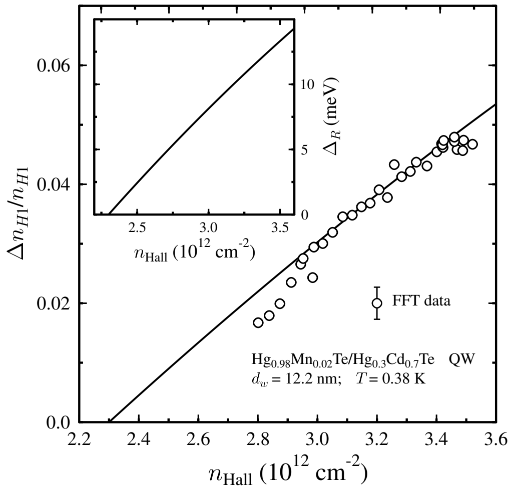

Figure 5.4: Population difference of the spin-split $H1$ as a function of the total carrier concentration. The circles are FFT data as shown in Fig. 5.3, the line are the theoretical values obtained from Hartree calculations. The inset shows the corresponding Rashba energies.

the processing of the sample with insulator and gate. According to our experience, a symmetric sample measured without assembled gate often exhibits with the gate a small asymmetrie. Usually a gate voltage less than ±1 V is sufficient to eliminate the asymmetrie. Therefore, it is more likely that during the growth the doping profiles below and above the QW have been different.

To ensure that the conclusions which we draw from the measurements are correct, another uncertainty of the epitaxial growth of the sample has to be ruled out. If the manganese concentration were not constant along the growth direction and the centre of the $H1-$ and $H1+$ wavefunctions would shift significantly with gate voltage, then $(\Delta E)_{max}$ would change, causing a shift in the node positions and the gate voltage dependence of the experimental node positions is caused by an inhomogeneous Mn distribution rather than the Rashba effect. The expected dependence

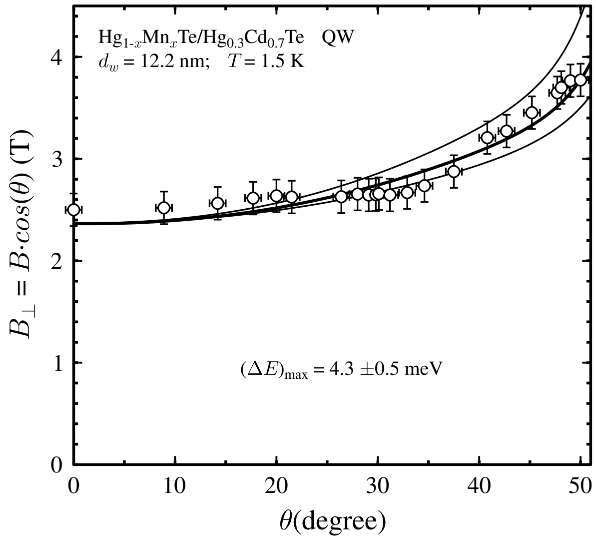

Figure 5.5: The perpendicular component of the magnetic field of the $\nu = 1.5$ node as a function of tilt angle, θ. Calculated values are also shown when $(\Delta E)_{max} = 4.3$ meV (thick line) is employed in Eq. (5.3) and a variation in $(\Delta E)_{max}$ of ±0.5 meV is allowed (thin lines).

on tilt angle, θ, for different values of $(\Delta E)_{max}$ can be calculated by combining Eqs. (5.2) and (5.3). As shown in Fig. 5.5, tilted magnetic field experiments have demonstrated that $B_\perp$ values for the $\nu = 1.5$ node follow the predicted dependence on θ when $(\Delta E)_{max} = 4.3$ meV. The results for a variation in $(\Delta E)_{max}$ of ±0.5 meV are also shown in Fig. 5.5. Hence the uncertainty in $(\Delta E)_{max}$ is $< \pm 0.5$ meV and the Mn distribution is homogeneous to better than ±10 % across the quantum well. The experimental differences in population between the two sub-levels of the first conduction subband have been accurately reproduced by self-consistent Hartree calculations as a function of the gate voltage or asymmetry of the QW. The carrier density maximum for $H1-$ and $H1+$ shifts a mere 2.4 and 1.1 monolayers, respectively, over the entire range of experimental gate voltages. Therefore a change in the saturation value of the exchange energy due to an inhomogeneous Mn distribution is inconceivable.

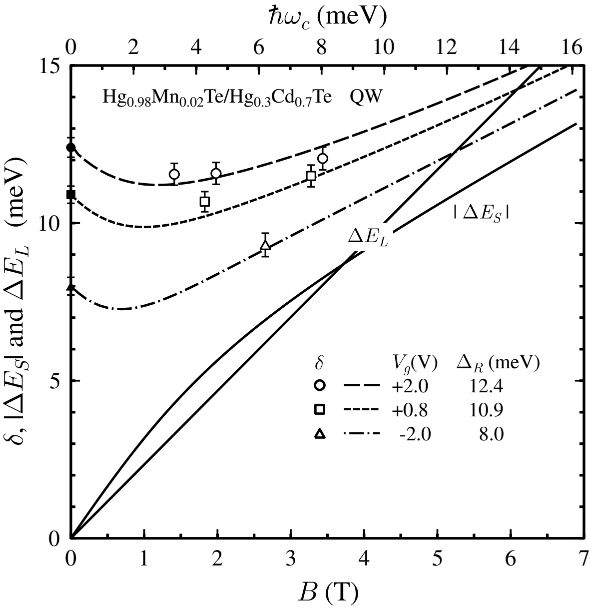

Figure 5.6: Experimental values (empty symbols) for the total level splitting energy, δ, versus B and the Landau level splitting, $\hbar\omega_c$ for Q1697 for three gate voltages at $T = 0.38$ K. The corresponding calculated Rashba s-o splitting energies are indicated by filled symbols. The curves are the results for δ via Eq. (5.4) at these three gate voltages, for $\Delta E_S = g^*\mu_B B$ using g^* from Eq. (5.3) and for $\Delta E_L = \hbar(e/m^*)B$.

Valuable insight into the relative importance of the various effects can be obtained from a simple model, which takes the Rashba effect and $sp-d$ exchange interaction into consideration, but neglects bulk inversion asymmetry and nonparabolicity. With this model the total level splitting energy for high Landau numbers can be expressed to a first approximation as a function of magnetic field according to [DDR90; Pfe97; PZ99]

$$\delta \approx \sqrt{(\hbar\omega_c - g^*\mu_B B)^2 + \Delta_R^2} - \hbar\omega_c. \tag{5.4}$$

In spite of their strong nonparabolic band structure, experimental and theoretical values of $\hbar\omega_c$ for HgTe QWs are nearly linear with magnetic field [PJ00]. Using the theoretical value of Δ_R and the values of the effective g factor according to Eq. (5.3), the total spin splitting energy, δ, has been calculated for three gate voltages and is plotted in Fig. 5.6 together with $g^*\mu_B B$ and $\hbar\omega_c$. The calculated values of Δ_R are also plotted in Fig. 5.6 at $B = 0$. At high magnetic fields, the exchange interaction tends to saturate and the Zeeman splitting, i.e., $g_0\mu_B B$, corresponds to the value for a HgTe QW without Mn. The experimental spin splitting energies from Eqs. (5.1) and (5.2) for three gate voltages are also plotted in Fig. 5.6 versus $\hbar\omega_c$. Obviously these values are in good agreement with the calculated values of $\delta(B)$.

To sum up, one can say that the Rashba effect and giant Zeeman spin splitting have been separately investigated in one and the same sample by varying the structure inversion asymmetry via a gate voltage and by changing the temperature of the Mn ions, respectively.

5.2 Filling factor $\nu = 1$

In the progress of this thesis one extraordinary sample arrested special attention: The 2% manganese containig HgMnTe quantum well Q1721. In transport measurements on a standard Hall bar this sample exhibits the $\nu = 1$ quantum Hall plateau from below 1 T up to the maximum at that time available field of 8 T. This behaviour is apriori astonishing because for HgMnTe samples one would expect the quantisation not below 2 T which corresponds to the observations made on such samples so far. Therefore a new phenomenon has to be taken into account. One possible explanation is the anomalous Hall effect (AHE) in paramagnetic two-dimensional systems which will be introduced in the following according to Ref. [CMN03].

When a nonferromagnetic metallic sample is exposed to a perpendicular external magnetic field, the Lorentz force acting on the current carriers gives rise to a transverse voltage in the plane of the sample. The transverse component of the resistivity ρ_{xy} depends on the magnetic field through

$$\rho_{xy} = R_0 B, \tag{5.5}$$

where $R_0 = 1/ne$ is known as the Hall coefficient. This phenomenon is known as ordinary Hall effect (OHE).

In many ferromagnets, however, the transverse resistivity acquires an additional term which is often seen to be proportional to the magnetisation of the sample, and becomes constant once the sample has reached its saturation magnetisation M_s. Empirically, one writes

$$\rho_{xy} = R_0 B + R_s M. \tag{5.6}$$

The effect is referred to as the anomalous Hall effect while the constant R_s is called the anamalous Hall coefficient. The effect was subsequently observed in a large number of bulk alloys and ferromagnetic semiconductors. Although the experimental evidence of the AHE was proved for a long time, the theoretical description has had a controversial history and the AHE remains a somewhat poorly understood phenomenon. For a review of the mechanisms that have been made accountable for the AHE the reader is referred to [CMN03]. The model applied here is based on a semiclassical analysis of wave packet motion in Bloch bands with a Berry phase correction to the carrier velocity as described in [CMN03]. This model provides a conceptual framework for the theoretical study of the AHE in magnetic QWs which have been realised among others in HgMnTe QWs. These structures constitute the simplest systems in which the Berry phase can be evaluated analytically from the Hamiltonian including the Rashba SO coupling.

The previously for $B = 0$ developed model has to be adapted as in the paramagnetic system the exchange field which causes the AHE can only be maintained by applying an external magnetic field. This causes two problems to observe the AHE: The Landau quantisation and the ordinary Hall effect. The first obstacle is circumvented by the presence of disorder in the sample, as impurity scattering causes the Landau levels to broaden so that for small enough magnetic fields they overlap. The impurity scattering is represented by a scattering time τ which is in the order of 1 ps (c.f. sec. 4.2). In small enough magnetic fields, where $\omega_c\tau < 1$, an overlap is ensured and the semiclassical approximation is valid. Here, in absence of quantum oscillations, the ordinary Hall contribution is given by the Drude formula (sec. 1.1). To ensure that the AHE is the dominant effect, we set

$$\sigma_{xy}^{OHE} < \sigma_{xy}^{AHE}. \tag{5.7}$$

The condition that the AHE is not completely overshaded by disorder requires that the exchange splitting h_0 must exceed the energy fluctuation due to disorder, $\hbar/\tau$. According to [CMN03] the condition for the observation of the AHE is now

$$\frac{2\pi n\hbar^2}{m^*}\omega_c\tau < \frac{\hbar}{\tau} < h_0. \tag{5.8}$$

To obtain the mentioned parameters intense measurements on the longitudinal and transversal resistance have been carried out. Because of the extraordinary behaviour of the sample to exhibit the $\nu = 1$ plateau from below 1 T up to 30 T, it was not possible to determine the carrier density until we found a small kink at 0.31 T in the Hall resistance with a corresponding small local minimum in the longitudinal resistance, which we could identify as a hint for the filling factor $\nu = 2$ plateau. The charge carrier density can therefore be calculated to be 1.5×10^{10} cm^{-2}. Hence, we obtain a mobility of $62.5 \times 10^3 \mathrm{cm}^2/(\mathrm{Vs})$. Introducing these values into Eq. (5.8) provide the condition that the anomalous Hall effect in this sample can if at all be observed in magnetic fields below 0.15 T. In such small fields a deviation from the ordinary Hall effect is not resolvable with our

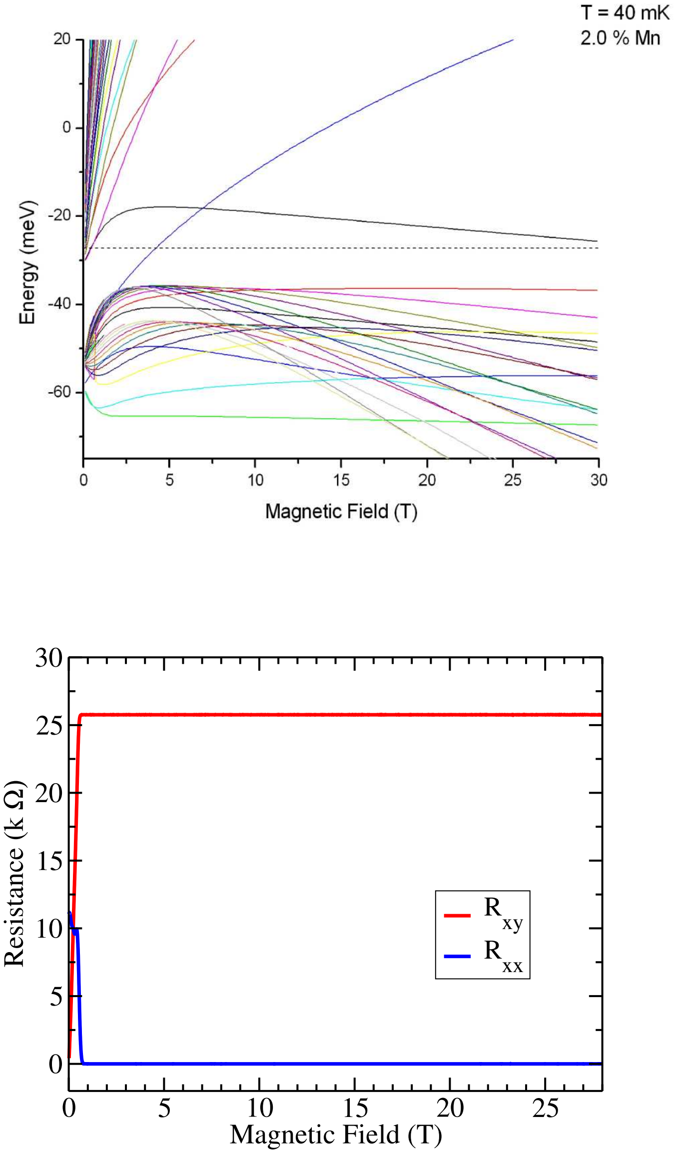

Figure 5.7: In the upper panel the calculated band structure of the 2% Mn containing QW Q1721 at 40 mK is shown. In the lower panel measurements of the longitudinal (blue) and transversal (red) resistance of this sample at the same temperature are plotted.

measurement setup. The origin of the extraordinary behaviour remains therefore unexplained. But the determination of the carrier density allows us now to calculate the correct band structure of the sample according to section 3.1. In the upper panel of figure 5.7 the calculated band structure (according to sec. 3.1) of the discussed sample is shown. One can see the extraordinary behaviour of the $H1$ band (black). For small magnetic fields it has a positive curvature but then changes to a negative curvature and remains above the Fermi energy (dotted line) until more than 30 T at a temperature of 40 mK. Hence, it is comprehensible that the sample remains in a conducting phase. The rising $H2$ band (blue) remains unoccupied due to different Bloch components. The consequence of this particular behaviour can be found in the lower panel of figure 5.7: The $\nu = 1$ quantum Hall plateau is maintained up to the highest accesible magnetic field at the Grenoble High Magnetic Field Laboratory of 28 T. If the temperature is increased, as shown in Fig. 5.8, the $H1$ band crosses the Fermi energy at lower fields (according to the band structure calculations not shown here) and the sample enters the isolating phase. This fact is observable in the measurement curves up to 20 K, where the $\nu = 1$ plateau is still obtained. In contrast to the afore presented measurement data, here, a rise in the resistance for fields above 25 T is observable.

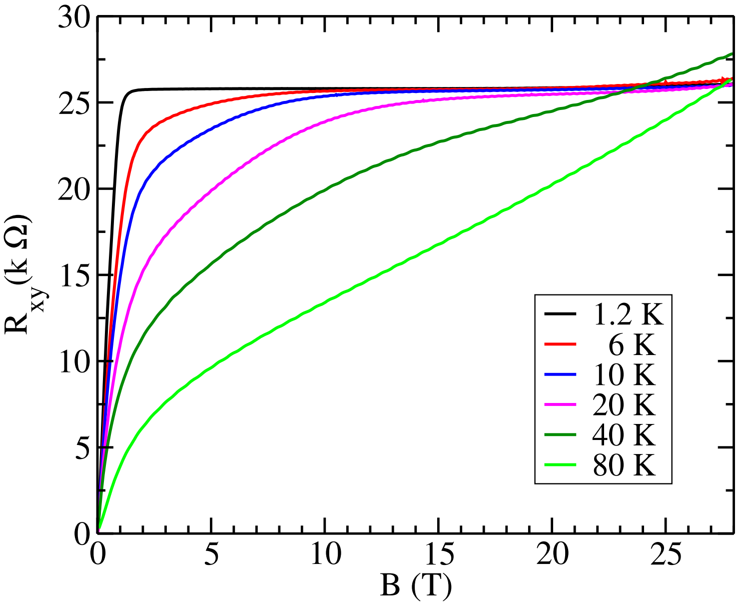

Figure 5.8: Hall effect data on Q1721 for various temperatures.

On the other hand Culcer *et al.* have calculated the condition for an observation of the anomalous Hall effect [CMN03]: For a manganese concentration of 2.2% and a carrier density of 1×10^{11} cm^{-2} they find, that the ordinary and the anomalous conductivities will be equal to just over 0.14 of the conductivity quantum, when applying the sufficient field of 130 mT according to Eq. (5.8). This can not explain a quantisation of $\nu = 1$.

To sum up, it is now possible to give a complete explanation of this extraordinary behaviour. The above mentioned band structure calculations can fully explain the experimental results.

5.3 Phase Transition into Spin-Glass Phase?

In section 4.2 we observed fluctuations in the NLR signal in the cross shaped sample structure which we identified as universal conductance fluctuations (UCF). Following the idea that the UCF signal is a “magneto-fingerprint” of the sample, as introduced in section 2.7, we expected to find a characteristic change therein, if a DMS sample is cooled down below the freezing curve for the spin glass phase (c.f. sec. 3.5). Initially we investigated the temperature dependence of the UCF in the nonmagnetic QW sample Q1819 with the cross shaped structure. In the second part of the section, UCF measurements of the 5% manganese containing QW Q1946 will be presented.

The proof that the fluctuations are not induced by electronic noise is given by repeating the measurement. In Fig. 5.9 part of the NLR signal is shown (black curve). The red curve is a repetition of the measurement. One can see clearly that the fine structure is fully reproducible. Measurements at various temperatures as shown in the left part of Fig. 5.10 indicate the dependence of the amplitude on the temperature. To extract the UCF signal from the large NLR signal, a 40 point average was subtracted as demonstrated in Fig. 5.10. The resulting UCF signal for temperatures from 1.4 K to 42 K are plotted in the left part of Fig. 5.11. One can see clearly a decrease of the amplitude with increasing Temperature. The reproducibility of the traces for two different temperatures is demonstrated in the right part of the same figure which shows an enlargement of the 1.4 K and 4.2 K measurements. A measure of the amplitude is the standard deviation $\sigma = \sqrt{\langle(\Delta R)^2\rangle}$ of the resistance R.

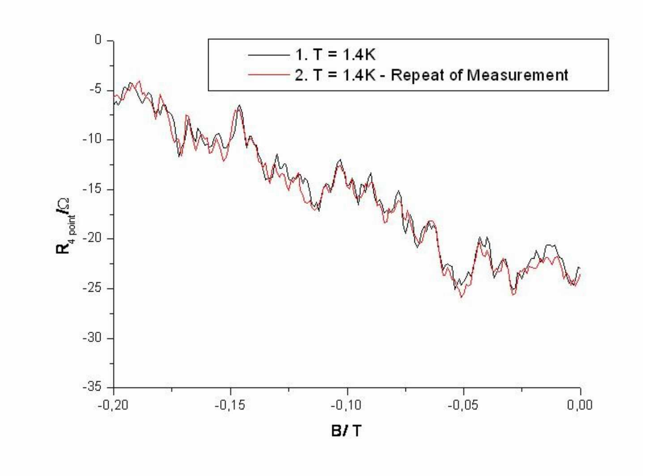

Figure 5.9: The repeatment (red curve) of a four terminal resistance measurement (black curve) demonstrates the reproducibility of the fine structure.

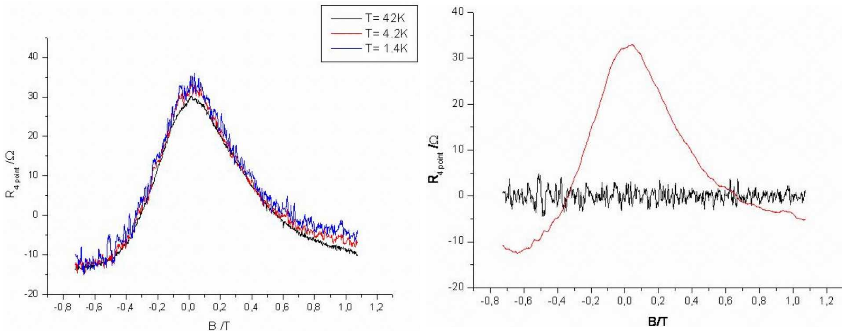

Figure 5.10: Left: Measured data of the NLR at various temperatures. Right: A 40 point average (red curve) was subtracted from the NLR data (left) which results in the UCF signal (black curve).

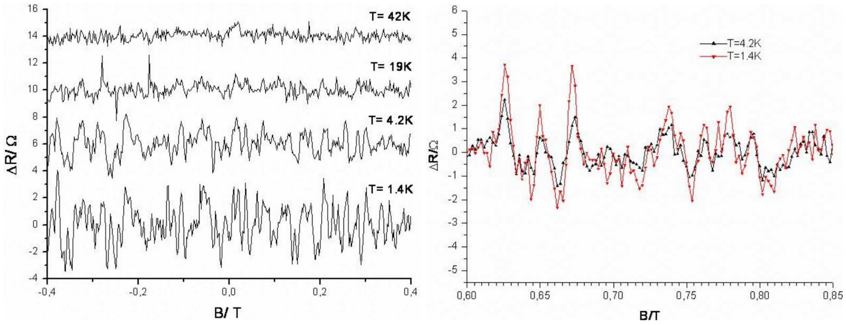

Figure 5.11: Left: Four point resistance (after background subtraction) for various temperatures. Right: Enlargement of the 1.4 K and 4.2 K measurements to demonstrate the reproducibility.

It should be noted that the standard deviation of R is the sum of the standard deviations of the signal and the noise. Therefore the standard deviation of the noise, which has been estimated to be 0.2 Ω, must be subtracted. This estimate has been determined from the difference of the two curves in Fig. 5.9 as well as an extrapolation to still higher temperatures where the phase coherence is destroyed and the fluctuations are only produced by noise. According to the UCF theory, the dependence of σ on temperature should be given by a power law, i.e., $\sigma(T) \propto T^b$, where $b \approx -0.5$ [LS85; LSF87]. In Fig. 5.12 the corresponding σ is plotted versus T with logarithmic axes. The red line represents the $Y = \text{const.} \cdot T^{-0.64}$ function. The temperatures have an error on the order of ±2 K for those temperatures greater than 4.2 K since at this point sample heating was required. Within this large error at high temperatures the experimental data agree very well with the least square fitted line representing a power law based on the theoretical description.

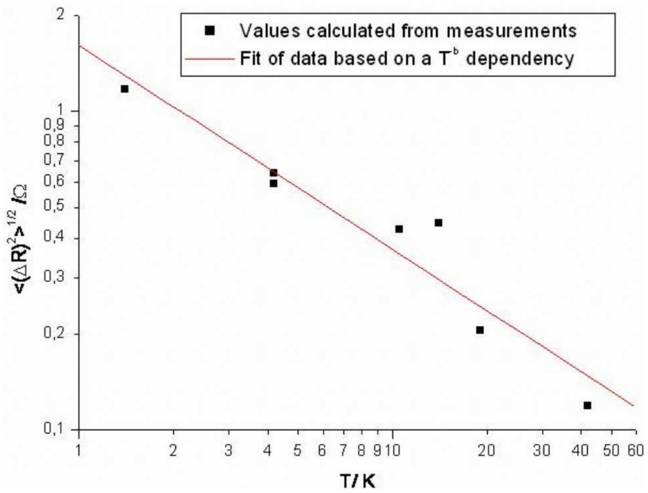

Figure 5.12: Standard deviation of four point resistance fluctuations (minus standard deviation of noise) as a function of temperature. The least square fitted (red) line has a temperature dependence of $T^{-0.64}$.

Because the UCF originate from randomly distributed imperfections in the periodic lattice potential, they are not expected to show any periodicity. In order to see if the UCF measurements exhibit periodicity, FFT spectra of the resistance curves in Fig. 5.11 have been performed. The raw data of the FFT, plotted in the left part of Fig. 5.13, show peaks at many frequencies. For a better comparison a ten point average (red curve) was taken and plotted for various temperatures in the right part of the same figure. Here, distinct peaks around 20 T^{-1}, 40 T^{-1} and 60 T^{-1} can be found. This peaks can be identified for all temperatures demonstrating a general structure in the smoothed FFT spectra. Such peaks at a given frequency in $1/B$ can be assigned to two different paths around a characteristic area acquiring an additional relative phase difference of 2π just as the two arms in the ring shaped structure which result in the Aharonov-Bohm effect (c.f. sec. 2.2). The corresponding area A can be calculated according to

$$A = \frac{\varphi_0}{\Delta B}, \tag{5.9}$$

where $\varphi_0 = h/e$ is the flux quantum and ΔB the field difference between two adjacent maxima of constructive interference. For the above mentioned peaks the corresponding areas are 0.83, 1.65 and 2.48×10^{-13} m^2, respectively. A rough estimate of the relevant area in the cross shaped structure with lead widths of 0.45 μm is (0.45×0.45) $\mu\mathrm{m}^2 = 2.03 \times 10^{-13}$ m^2, which is of the same order as the ones calculated from the FFT spectra. Therefore, it is plausible that the periodicity evident in the FFT of resistance fluctuations is caused by the specific geometry of

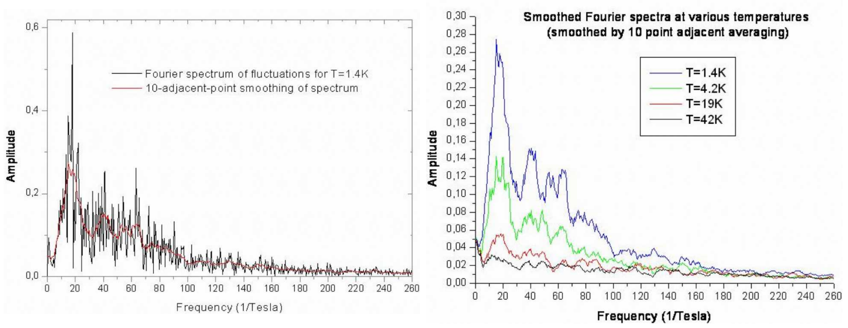

Figure 5.13: Left: FFT spectrum of the 1.4 K resistance measurement and the smoothed, 10 point average, curve (red). Right: Smoothed FFT spectra for various temperatures.

the sample. In contrast to a ring shaped structure the paths are geometrically less defined and may depend on the injecting angle and the degree of deflection of the electrons caused by the magnetic field. Hence, the peaks in the FFT spectra are smeared out around a central frequency.

As the coherence length becomes shorter with rising temperature, due to, e.g., phonon scattering, then the amplitude of the periodic contributions to the resistance fluctuation curve measured by varying the magnetic field, is expected to decrease. Although this can clearly be seen in Fig. 5.13, an additional plot of the amplitude of the first peak in the smoothed FFT spectra as a function of temperature, depicted in Fig. 5.14, reveals, that the temperature dependence is practically the same as that for the standard deviation of the fluctuations. That is to say, the amplitude of the contributions to the resistance fluctuations which are periodic in magnetic field also appears to be proportional to $\mathrm{T}^{-0.6}$. However, it should be noted that in the determination of the temperature dependence of the standard deviation of the fluctuations the result obtained is strongly influenced by the value attributed to noise and subsequently subtracted from the data. For example, if no value is subtracted then a fit of the data results in a $\mathrm{T}^{-0.4}$ dependence. The danger of inaccuracy by smoothing the FFT data is evident, but the comparison of raw data with the smoothed data in Fig. 5.13 and a similar comparison for the data at different temperatures (not shown), as well as the agreement of the temperature dependence $\sigma(T)$ and with that of the UCF theory strengthens this conclusion.

However, the agreement between the temperature dependence of the peak amplitude in the Fourier spectrum and the standard deviation of the resistance fluctuations is not surprising. The peak in the Fourier spectrum can be interpreted as being an averaged amplitude of contributions to fluctuations in the magneto-fingerprint, which are caused by the combined interference effect of those pairs of paths, which differ from each other by a certain reflection sequence on the cross walls. Since these particular pairs of paths are just a subset of all classically allowed paths, it is

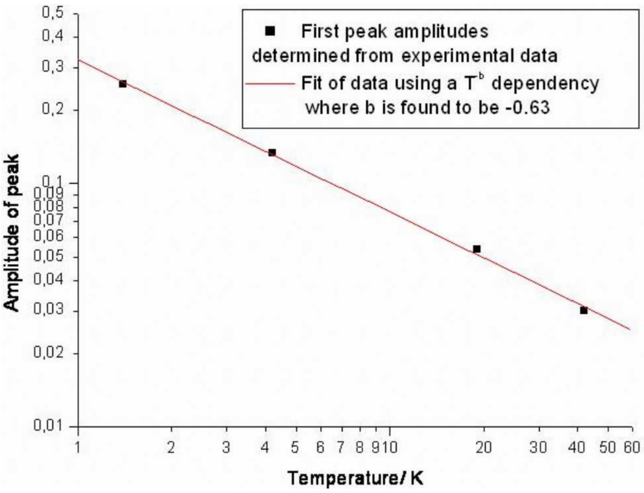

Figure 5.14: Amplitude of the first peak of the smoothed FFT in Fig. 5.13 as a function of temperature. The fitted (red) line has a temperature dependence of $T^{-0.63}$.

expected that the statistics for this subset will be the same as for the complete set of paths. This assumption explains the temperatur dependence of the FFT spectrum peak, since if the amplitude of the peak can be regarded as being the aforementioned averaged amplitude then this must be something like the standard deviation of a subset of fluctuations.

Encouraged by the matching results on the nonmagnetic sample, UCF measurements on the 5% Mn containing symmetric QW Q1946 have been performed. To avoid the problems with the specific sample geometry several simpler geometries have been realised. At first, a standard Hall bar was fabricated to determine the sample parameters. In a standard ^{4}He bath cryostat at 4.2 K a carrier concentration of 3.5×10^{11} cm^2 and a mobility of 20×10^3 cm^2/(Vs) have been obtained. Then, on one piece of the sample, 0.5 μm wide stripes with a distance between the voltage contacts of 1, 2, and 3 μm have been fabricated. Another piece of the sample has been patterned as a micro Hall bar with a width of 5 μm and a distance between the longitudinal voltage probes of 20 μm.

The stripe with the 1 μm separated voltage contacts was not measurable, possibly due to a large defect in the crystal structure directly below the nanostructure. The 2 μm long stripe exhibits resistance oscillations on the order of 1 MΩ, which is of the same order as vertical transport through the substrate would cause and remains therefore disregarded. Hence, only the results of the 3 μm long stripe will be discussed here. At that time the lowest temperature accessible at our laboratory was 300 mK in a single shot ^{3}He cryostat. Since the phase transition of a $Hg_{0.95}Mn_{0.05}Te$ sample between spin glass and paramagnetic phase occurs around

400 mK according to the phase diagram in Fig. 3.8, a characteristic change in the resistance behaviour should be measurable, even though fine tuning of the temperature in our single shot ^{3}He cryostat was impossible. In Figure 5.15 the four point resistance as a function of the magnetic field for temperatures from 0.3 K up to 40 K is shown. In the left part of the Figure, the corresponding FFTs are plotted. The curves of the longitudinal resistance exhibit a large fluctuation whose amplitude is strongly temperature dependent. The origin of this oscillation is apriori unclear. The curves below (0.3 K) and above (0.7 K) the phase transition line differ only slightly. A first weak hint for a phase transition may be the following: Whereas the amplitude decreases monotonously with increasing temperature for $T \geq 0.7$ K, the amplitude of the 0.7 K measurement is reproducible slightly larger then the one measured at 0.3 K. This fact is also evident in the FFT amplitude. In the FFT peaks at 4 T^{-1}, 7 T^{-1}, 11 T^{-1}, and a broad one around 17.5 T^{-1} are observed. Following the arguments above, the corresponding areas, calculated according to Eq. (5.9), are summarised in Table 5.1. In the last column the corresponding radii r, assuming an orbital area of $A = \pi r^2$, are given. Compared to the results obtained from the FFT analysis of the cross shaped structure whose areas and lengths are far from those of the sample geometry here. If any at all, only the broad peak near 17.5 T^{-1} can be attributed to a sample geometry induced pair of paths.

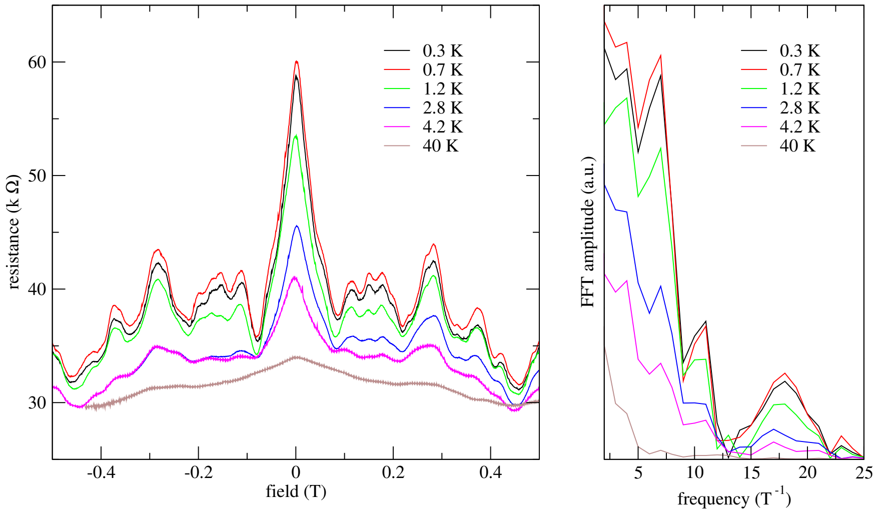

Figure 5.15: Left: Temperature dependent four point resistance of a 3 μm long, 0.5 μm wide stripe on a $Hg_{0.95}Mn_{0.05}Te$ sample as a function of magnetic field. Right: Corresponding FFT.

freq. (T^{-1})	ΔB (T)	A (m^2)	r (nm)
4	0.250	1.65×10^{-14}	72.6
7	0.143	2.90×10^{-14}	96.0
11	0.091	4.55×10^{-14}	120.3
17.5	0.057	7.24×10^{-14}	151.8

Table 5.1: Summary of parameters obtained by analysis of the FFT spectra in Fig. 5.15.

Unfortunately, it was not possible in the cryostat setup at that time to reduce the noise below 0.2% of the signal, which was 80 Ω. Therefore UCF induced resistance fluctuations which are on the order of several Ohms could not be resolved. The newly installed, shielded ^{3}He/^{4}He dilution refrigerator with automatic temperature control opens the possibility of low noise measurements in the temperature range from 10 mK up to 1 K. However, the discussed sample with the stripes did not survive the previous temperature cycles and transfer to the dilution refrigerator. A new sample had to be prepared and we decided to increase the dimensions further to avoid sample geometry specific features. For the new design, a micro Hall bar with a width of 5 μm and a distance between the longitudinal voltage contacts of 20 μm was chosen. A low resolution, high field measurement of the longitu-

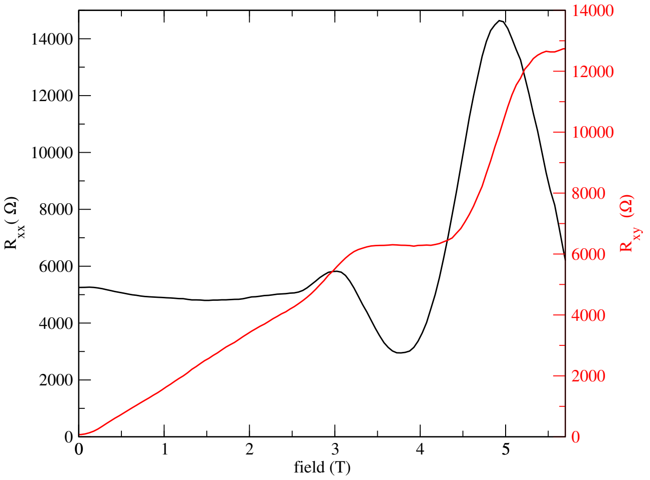

Figure 5.16: SdH oscillations (black) and quantum Hall effect (red) in a micro Hall bar on Q1946.

dinal (black curve) and Hall resistances (red curve), depicted in Fig. 5.16, shows that the sample parameter n and μ which have been derived to be 3.7×10^{11} cm^{-2} and 13×10^{3} cm^{2}/(Vs), respectively, have not been changed by the nanofabrication process. The small decrease in mobility is not surprising since restrictions of transport by a dislocation is more relevant in a structure with only 1/50 of the width of a standard Hall bar. High resolution measurements of the longitudinal resistance in small magnetic fields for various temperatures as well as the corresponding FFT are plotted in Fig. 5.17.

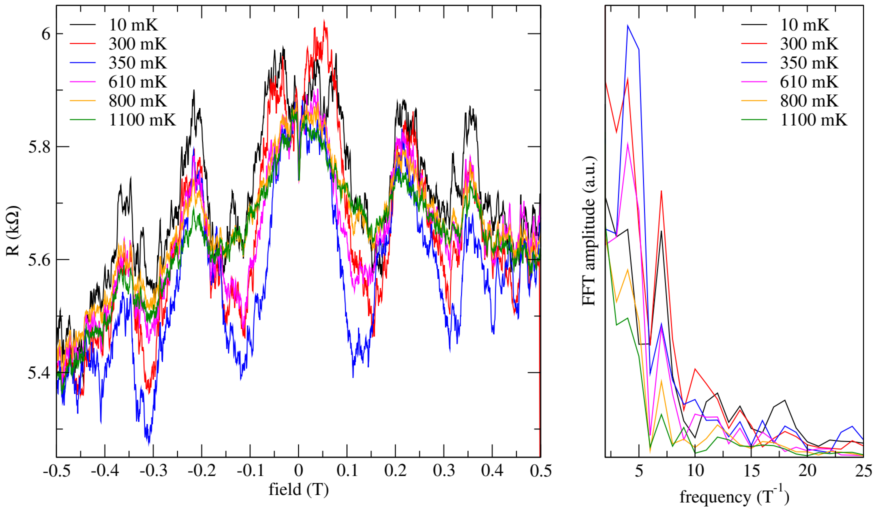

Figure 5.17: Left: Temperature dependent longitudinal resistance of a micro Hall bar on Q1946 as a function of magnetic field. Right: Corresponding FFT.

It has to be mentioned that sometimes between two measurement cycles, sudden resistance changes of 500 Ω occured independent of temperature. Thus, the total curve shifted 500 Ω. This happened randomly at different temperatures once or twice a day, likely caused by a point defect in the crystal structure which in some configuration reduces the mobility. But due to the long stabilising times only two or three different temperatures could be measured on one day. Hence, for a better comparison, the curves in Fig. 5.17 are shifted together to have the same value at $B = 0$. The resistance curves again exhibit a large fluctuation with amplitudes depending on temperature. But in contrast to the stripe patterned piece of the same sample, a tendency is clearly revealed. With increasing temperature the amplitude increases up to the one measured at 350 mK, then decreases monotonously with increasing temperature. To find the temperature with the maximum amplitude avoiding the aforementioned problems, measurements at a fixed magnetic field have been performed while the sample was heated up or cooled down within a time period of hours. Subtracting the values found at $B = 210$ mT (maximum) from those found at $B = 150$ mT (minimum), provides a measure of the amplitude as a function of temperature. The result is shown in Fig. 5.18. One can see clearly that the amplitude has a maximum at 420 mK, right at the temperature where the phase transition between spin glass and paramagnetic phase for a $Hg_{0.95}Mn_{0.05}Te$ sample is expected [BM84]. This is strong evidence that the large fluctuations are connected with the presence of manganese in the sample. Whereas the increase of the amplitude with decreasing temperature from 1 K down to 420 mK can be explained straight forward with an increasing phase coherence length, the inverse dependency for the temperatures below 420 mK requires the consideration of a different magnetic ordering. In the spin glass phase the antiferromagnetic exchange interaction is mediated by the charge carriers as well as other mechanism [Myd93]. During freeze out of the spin glass the carriers are more and more localised and can not contribute to phase coherence transport. Thus, the amplitude also decreases at lower temperatures.

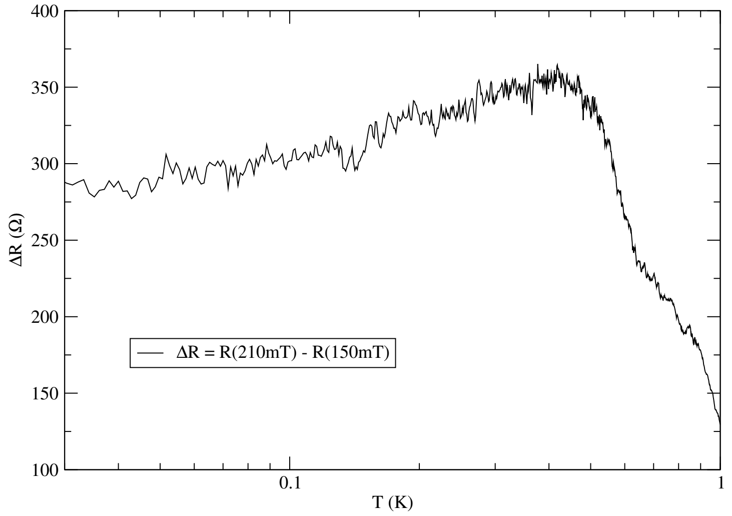

Figure 5.18: Difference of the resistance at $B = 210$ mT and $B = 150$ mT as a function of temperature.

Comparing the FFTs of the resistance in the stripe (Fig. 5.15) with those of the micro Hall bar measurements (Fig. 5.17), one can also find in the latter unambiguous peaks at 4 T^{-1} and 7 T^{-1} which are consequently independent of the particular sample geometry. The corresponding periods of 250 mT and 143 mT, respectively, can be identified with those of the large fluctuations. Hence, the lateral size of Mn cluster can be estimated to be $(1.65 \pm 0.21) \times 10^{-14}$ m^2 or $(2.90 \pm 0.21) \times 10^{-14}$ m^2. The uncertainty results from an error of ± 0.5 T^{-1} in the FFT. The latter corresponds to an area twice as large as that of the former which is synonymous to a dual circuit rather than one. As it is more plausible to consider a path with twofold circulation than two different cluster sizes with one twice as large as the other, the lateral size of the Mn cluster in Q1946 is found to be $(1.65 \pm 0.21) \times 10^{-14}$ m^2. Regardless of the fact that the geometric form of a Mn cluster is most probably not circular, for better comprehension the radius of such a circle would be given by $r = 72.6 \pm 4.5$ nm.

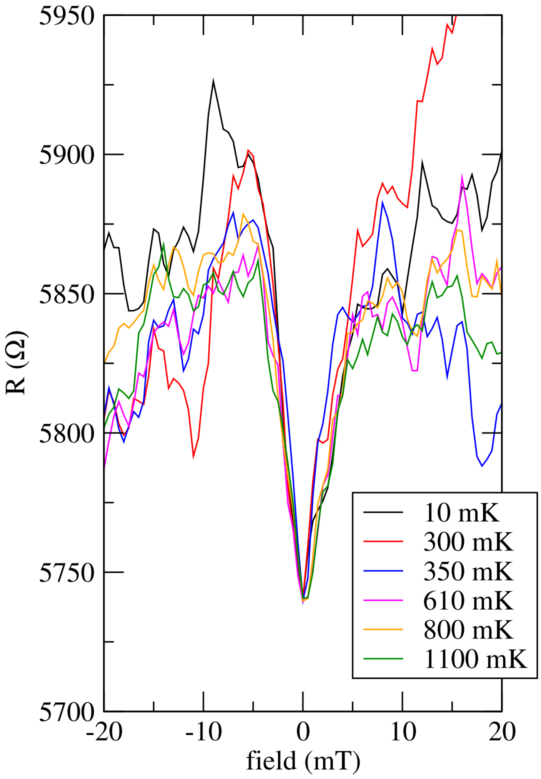

Figure 5.19: Enlargement of Fig. 5.17 around $B = 0$. A pronounced weak anti-localisation peak is resolved for all temperatures.

An enlargement of the measured curves in Fig. 5.17 reveals additional features. In Fig. 5.19 a pronounced minimum around $B = 0$ for all temperatures can be seen. We identify this minimum as the weak anti-localisation peak due to spin-orbit interaction [HLN80]. The curves for different temperatures differ only slightly and the relative peak height is almost constant. In HgMnTe samples the weak anti-localisation is caused by the Rashba SO coupling [Win03]. As the Rashba effect is nearly temperature independent, the weak anti-localisation is expected to be equally independent which is demonstrated in Fig. 5.19. Although the sample was designed to be symmetrical, possible differences in the doping profiles above and below the QW can introduce an asymmetry as discussed in detail in the last section.

In Fig. 5.20 one can see additional fine structure superimposed on the large fluctuations. Analogous to the analysis of the nonmagnetic sample, discussed in the first part of this section, the UCF have been studied for various temperatures. Therefore, a 20 point (ΔB =10 mT) average curve has been subtracted. The average of the curve together with the curve at 10 mK are represented in Fig. 5.20. The standard deviation σ of the resulting curves has been employed as a measure for the amplitude. In Fig. 5.21 the standard deviation of the UCF is plotted as a function of temperature. According to the results in the nonmagnetic sample, the data have been fitted with a $T^{-0.64}$ dependence. But only for data with $T > 400$ mK, in the paramagnetic phase is it possible to obtain reasonable results which are indicated by the red line. For temperatures below the freezing curve the amplitude of the

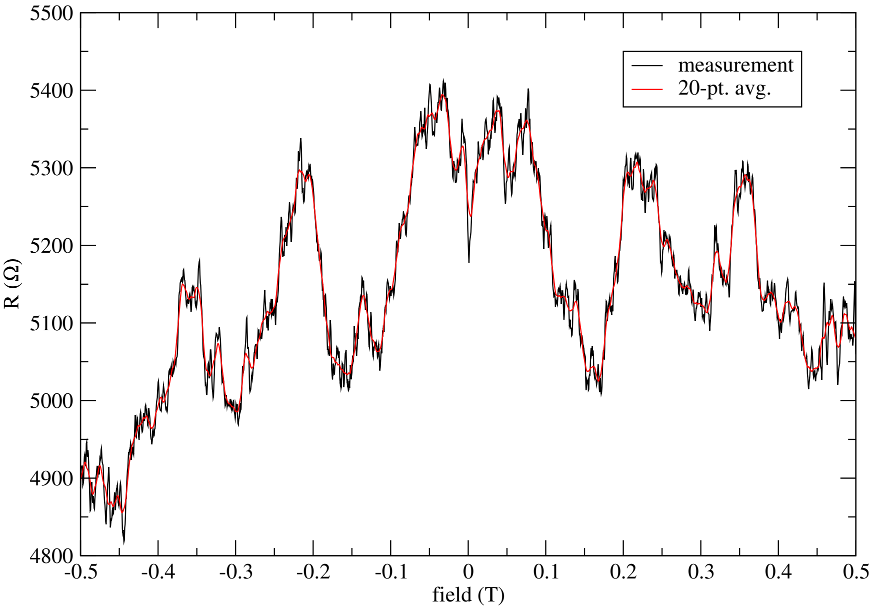

Figure 5.20: Longitudinal resistance as a function of magnetic field (black) at 10 mK and a 20 point average curve (red).

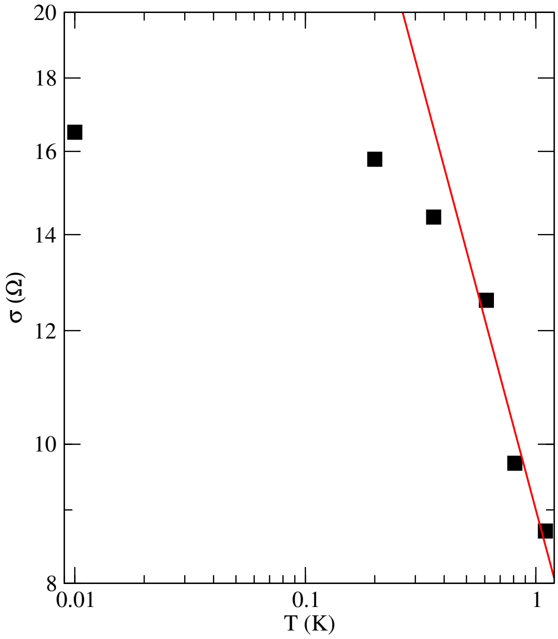

Figure 5.21: Standard deviation of the UCF as a function of temperature. The red line is a fit (Y = const. $\cdot T^{-0.64}$) of the data above the phase transition temperature.

UCF tends to saturate. To our knowledge this is the first time that a phase transition in the magnetic ordering has been investigated by transport measurements on a magnetic 2DEG. De Vegvar *et al.* have studied CuMn films and wires and could identify frozen spin configurations by exploiting the time reversal invariance of the Onsager-Büttiger relations [dVLF91; dVF93]. Their resistance amplitudes decrease monotonously with temperature when crossing the freezing curve. In thin epilayers of CdMnTe with various manganese content, Jaroszynski *et al.* found an increase in the fluctuation amplitude in the paramagnetic phase if they increased the applied magnetic field [JWK$^+$98]. In the spin glass phase they observed a decrease in the amplitude, whereas the noise increased. In their earlier paper, they reported on a monotonous increase of the resistance amplitude with decreasing temperature [JWS$^+$95]. Furthermore, Benoit *et al.* reported an increase of the amplitude with decreasing temperature in the spin glass phase [BMPN92].

Nevertheless, the subject of none of the aforementioned publications was a magnetic 2DEG. In this investigation we found clear evidence for a phase transition from the paramagnetic to the spin glass phase in a $\mathrm{Hg}_{0.95}\mathrm{Mn}_{0.05}\mathrm{Te}$ QW. The transition was observable in the irregular behaviour of the resistance fluctuations as well as in the deviation of the UCF amplitude from the theoretically expected behaviour, which is only expected for our sample in the paramagnetic phase.

5.4 Summary

In this chapter several aspects of the unique properties of $Hg_{1-x}Mn_xTe$ QWs have been analysed. In the first section it has been demonstrated that the Rashba and giant Zeeman splitting can be observed in one and the same sample. A method for separating these effects has been introduced. Whereas the Rashba effect can be identified by the solely dependency from the structure inversion asymmetry, varied by the applied gate voltage, the giant Zeeman splitting is extracted by its strong temperature dependency, while the Rashba splitting is kept constant. In the next section intense studies on the 2% Mn containing sample Q1721 have been presented. After two research stays at the Grenoble High Magnetic Field Laboratory an explanation of the extraordinary behaviour of this sample could be given. Finally clear evidence for a phase transition between the paramagnetic and spin glass phase in a 5% Mn containing sample has been found.

Summary and Outlook

Although spintronics has aroused increasing interest, much fundamental research has to be done. One important issue is the control over the electronic spin. Therefore, spin and phase coherent transport are very important phenomena. This thesis describes experiments with mercury based quantum well structures. This narrow gap material provides a very good template to study spin related effects. It exhibits large Zeeman spin splitting and Rashba spin-orbit splitting. The latter is at least four to five times larger than in III-V semiconductors.

Initially a short review on the transport theory was presented. The main focus was on quantisation effects that are important to understand the related experiments. Thus, Shubnikov-de Haas and the quantum Hall effect have been analysed. Due to the first fabrication of nanostructures on Hg-based quantum well samples, the observation of ballistic transport effects could be expected. Hence, the Landauer-Büttiker theory has been introduced which gives the theoretical background to understand such effects.

With respect to the main topic of this thesis, phase coherence has been introduced in detail. Experiments, where coherence effects could be observed, have been explained theoretically. Here, possible measurement setups have been discussed, e.g., a ring shaped structure to investigate the Aharonov-Bohm and related effects.

Due to the fact, that all experiments, described in this thesis, were performed on Hg-based samples, the exceptional position of such samples among the "classical" semiconductors has been clarified. $Hg_{1-x}Mn_xTe$ quantum wells are type-III QWs in contrast to the type-I QWs formed by e.g., GaAs/AlGaAs heterostructures. With a well width of more than 6 nm and a manganese content of less than 7% they exhibit an inverted band alignment. Band structure calculations based on self consistent Hartree calculations have been presented. The common description of a diluted magnetic semiconductor with the Brillouin function has been introduced and the experiments to obtain the empiric parameters T_0 and S_0 have been presented. Rashba spin-orbit splitting and giant Zeeman splitting have been explained theoretically and the magnetic ordering of a spin glass as well as the relevant interactions therein have been discussed.

The next chapter describes the first realisation of nanostructures on Hg-based heterostructures. Several material specific problems have been solved, but the unique features of this material system mentioned above justify the effort. Interesting new insight could be found and will be found with these structures. Onto a series of QW samples, cross-shaped structures with several lead widths have been patterned. With the non-local resistance measurement setup, evidence for quasi-ballistic transport was demonstrated in cross-shaped structures with lead widths down to 0.45 μm. The non-local *bend* resistance and a regime of rebound trajectories as well as the anomalous Hall effect could be identified. Monte-Carlo simulations of the classical electron trajectories have been performed. A good agreement with the experimental data has been achieved by taking a random scattering process into account.

Encouraged by this success the technology has been improved and ring-shaped structures with radii down to 1 μm have been fabricated. Low temperature (below 100 mK), four terminal resistance measurements exhibit clear Aharonov-Bohm oscillations. The period of the oscillations agrees very well with a calculation that takes only the sample geometry into account. One goal using such a structure is the experimental prove of the spin-orbit Berry phase. Therefore an additional Shottky gate on top of the ring was needed. With this structure evidence for the Aharonov-Casher effect was observed. Here, a perpendicular applied electric field causes analogous oscillations as does the magnetic field in the AB effect.

A subsequent change in the Rashba SO splitting due to several applied gate voltages while measuring the AB effect should reveal the SO Berry phase. Although initially evidence of a phase change was detected, a clear proof for the direct measurement of the SO Berry phase could not be found. In the future, with an advanced sample structure, e.g., with an additional Hall bar next to the ring, which permits a synchronous measurement of the Rashba splitting, it might be possible to measure the SO Berry phase directly.

In manganese doped HgTe QWs two different effects simultaneously cause spin splitting: the giant Zeeman and the Rashba effect. By analysing the Shubnikov-de Haas oscillations and the node positions of their beating pattern, it has been possible to separate these two effects. Whereas the Rashba effect can be identified by its dependence on the structure inversion asymmetry, varied by the applied gate voltage, the giant Zeeman splitting is extracted from its strong temperature dependence, because Rashba splitting is temperature independent. The analysis revealed, that the Rashba splitting is larger than or comparable to the giant Zeeman splitting even at moderately high magnetic fields.

In an extraordinary HgMnTe QW sample, that exhibits the $\nu = 1$ quantum Hall plateau from less than 1 T up to 28 T, the anomalous Hall effect could be excluded. Intense studies on the temperature dependence of the QHE as well as band structure calculations have revealed this extraordinary behaviour to be an ordinary band structure effect of this system.

In a series of mesoscopic structures on nonmagnetic and magnetic QWs, an investigation of the universal conductance fluctuations have been carried out. In the nonmagnetic case, the temperature dependence of the standard deviation of the resistance, which is a measure for the amplitude of the fluctuations, obeys a power law ($\propto T^{-0.64}$) in good agreement with the theory of Lee *et al.* In samples containing 5% manganese this agreement could only be found for temperatures above 400 mK. These samples exhibit an additional fluctuation with a period of 140 mT and an amplitude up to 200 Ω. This amplitude increases with decreasing temperatures down to 400 mK and decreases at lower temperatures again. A possible explanation has been found in the phase change from paramagnetic (T>400 mK) to the spin glass phase (T<400 mK), which explains the behaviour of the amplitude of the universal conductance fluctuations, too. With this identification a characteristic manganese cluster size has been determined to be on the order of 1.5×10^{-14} m^2 for this sample as described in detail in the text. Hence, a new method has been found to use a two-dimensional electron gas as a probe for the magnetic ordering.

This thesis introduced new methods and sample structures which can be employed to investigate phase coherent and spin dependent transport phenomena. New and known effects have been observed for the first time in Hg based heterostructures. As always, the unanswered questions increase faster than answers to previous questions. With an improved sample structure, as proposed in the text, the direct observation of the spin orbit Berry phase might be possible. The method which uses a 2DEG as a probe for the magnetic ordering can be applied to samples with different manganese content to finish the magnetic ordering phase diagram.

Zusammenfassung

Trotz des ständig steigenden Interesses an der Spintronik gibt es diesbezüglich noch viel an Grundlagenforschung zu leisten. Eine wichtige Aufgabe dabei ist es den Spin zu kontrollieren und gezielt zu beeinflussen. Aus diesem Grund ist es wichtig spin- und phasenkohärente Transportphänomene zu untersuchen und zu verstehen. Die vorliegende Arbeit befasst sich mit Experimenten an Quantentrogstrukturen auf der Basis quecksilberhaltiger Materialien. Dieser schmallückige Halbleiter ist ein ideales Versuchsobjekt zur Untersuchung von Effekten, die mit dem Spin zusammenhängen, denn er zeigt den riesigen Zeeman-Effekt sowie Rashba-Spin-Bahn-Aufspaltung. Letztere ist sogar vier- bis fünfmal so groß wie die in III-V Halbleitern.

Zu Beginn dieser Arbeit wurde ein kurzer Überblick über die Transporttheorie gegeben. Dabei lag das zentrale Interesse auf Quantisierungseffekten, welche zum Verständnis der nachfolgenden Experimente unabdingbar sind, insbesondere wurden der Shubnikov-de Haas und der Quanten-Hall-Effekt betrachtet. Da es im Rahmen dieser Arbeit erstmals gelungen ist, Nanostrukturen auf quecksilberhaltigen Quantentrögen herzustellen, war es zu erwarten, dass ballistische Transporteffekte beobachtet werden könnten. Daher wurde eine Einführung in die Landauer-Büttiker-Theorie gegeben, mit welcher es möglich ist solche ballistischen Effekte theoretisch zu beschreiben.

Das Hauptaugenmerk der vorliegenden Arbeit liegt auf Untersuchungen zur Phasenkohärenz. Deswegen wurde diese ausführlicher eingeführt. Dabei wurde die Theorie der Experimente, bei denen man Phasenkohärenz beobachten kann, dargestellt. Ebenso wurden mögliche experimentelle Aufbauten diskutiert, wie zum Beispiel eine ringförmige Struktur, an welcher man den Aharonov-Bohm, sowie damit verwandte Effekte untersuchen kann.

Quecksilberhaltige Heterostrukturen nehmen neben den “klassischen” Halbleitern eine Sonderstellung ein. Diese wurde im dritten Kapitel gewürdigt. Im Gegensatz zu den Typ-I Quantentrögen, z.B. gebildet aus einer GaAs/AlGaAs Heterostruktur, sind Quantentröge aus $\mathrm{Hg_{1-x}Mn_xTe/Hg_{0.3}Cd_{0.7}Te}$ vom Typ-III. Ist hierbei die Trogbreite größer als 6 nm und der Mangangehalt geringer als 7%, so weisen diese Tröge eine invertierte Bandstruktur auf. Hierzu wurden Bandstrukturberechnungen mittels selbstkonsistenter Hartree-Berechnungen dargestellt. Zur

Beschreibung verdünnt magnetischer Halbleiter wurde die dafür allgemein übliche Brillouin Funktion eingeführt. Die Experimente mit denen die dabei benötigten empirischen Parameter T_0 und S_0 gewonnen wurden, wurden an dieser Stelle präsentiert. Auch die Theorie der Rashba-Spin-Bahn-Aufspaltung sowie des riesigen Zeeman-Effekts wurden erklärt. Darüberhinaus wurde der magnetische Ordnungszustand "Spinglas" eingeführt, sowie die wichtigsten Wechselwirkungen darin dargestellt.

Im nächsten Kapitel wurde die erstmalige Realisierung von Nanostrukturen auf quecksilberhaltigen Heterostrukturen berichtet. Dafür mussten materialspezifische, technologische Probleme überwunden werden, aber die einzigartigen Eigenschaften dieses Materialsystems rechtfertigen den Aufwand. So konnten bereits und werden neue Einsichten gewonnen werden. Auf eine Serie von Quantentrogproben wurden Kreuzstrukturen mit unterschiedlichen Armdicken definiert. In diesen Strukturen konnte mit Hilfe der sogenannten Nichtlokalen Widerstandsmessung der Nachweis für quasiballistischen Transport erbracht werden. Der sogenannte Biegewiderstand, der Bereich der abprallenden Trajektorien sowie der anomale Hall-Effekt konnten identifiziert werden. Um diese Beobachtungen auch auf eine quantitative Beschreibung zurückzuführen, wurden Monte-Carlo-Simulationen der klassischen Trajektorien der Elektronen durchgeführt. Durch die Einführung eines zufälligen Streuprozessess konnte eine hervorragende Übereinstimmung mit den experimentellen Daten erzielt werden.

Ermutigt durch diesen Erfolg, wurde die Technologie weiter verbessert. So konnten ringförmige Strukturen mit Radii hinunter bis zu 1 μm hergestellt werden. Elektrische Vier-Punkt-Messungen bei niedrigsten Temperaturen (unter 100 mK) zeigen deutliche Aharonov-Bohm -Oszillationen. Die Periode dieser Oszillationen stimmt sehr gut mit der berechneten überein, die aus geometrischen Überlegungen zur Probe gewonnen wurde. Ein Ziel für die Verwendung solcher ringförmigen Strukturen ist der direkte experimentelle Nachweis der Spin-Bahn-Berry-Phase. Hierzu wird allerdings ein zusätzliches Shottky-Gatter auf der Oberseite des Rings benötigt. Mit einer solchen Struktur konnte der Aharonov-Casher-Effekt nachgewiesen werden. Dabei verursacht ein senkrecht anliegendes elektrisches Feld analoge Oszillationen wie das Magnetfeld im Aharonov-Bohm-Effekt.

Durch ein kontinuierliches Ändern der Rashba Spin-Bahn-Aufspaltung, hervorgerufen durch die Änderung der anliegenden Gatter-Spannung, während man den Aharonov-Bohm-Effekt misst, sollte die Spin-Bahn-Berry-Phase offenbaren. Obwohl zunächst ein Hinweis auf einen Phasenübergang gefunden werden konnte, war ein eindeutiger Nachweis für die direkte Messung der Berry-Phase nicht möglich. Zukünftige Messungen mit einer verbesserten Probenstruktur, z.B. einem zusätzlichen Hall-Streifen direkt neben dem Ring um gleichzeitig die Rashba-Aufspaltung messen zu können, werden möglicherweise diesen direkten Nachweis erbringen.

In mit Mangan dotierten HgTe Quantentrögen gibt es zwei unterschiedliche Effekte, die eine Spin-Aufspaltung hervorrufen: Der riesige Zeeman-Effekt und der

Rashba-Effekt. Durch die Analyse der Shubnikov-de Haas Oszillationen und der Knotenpositionen ihrer Schwebung, war es möglich, diese zwei Effekte zu trennen. Während der Rashba-Effekt durch seine Abhängigkeit von der Strukturinversionsasymmetrie, die durch Veränderung der anliegenden Gatter-Spannung variiert werden kann, identifiziert werden kann, erkennt man die riesige Zeeman-Aufspaltung durch ihre Temperaturabhängigkeit, da der Rashba-Effekt temperaturunabhängig ist. Diese Analyse konnte zeigen, dass die Rashba-Aufspaltung größer als oder mindestens vergleichbar der riesigen Zeeman-Aufspaltung ist, und das sogar bei mäßig hohen Magnetfeldern.

In einer außergewöhnlichen HgMnTe Quantentrogprobe, welche das $\nu = 1$ Quanten-Hall-Plateau von unter einem Tesla bis zu 28 Tesla aufweist, konnte der anomale Hall-Effekt als Ursache für dieses Verhalten ausgeschlossen werden. Intensive Untersuchungen der Temperaturabhängigkeit des Quanten-Hall-Effekts sowie Bandstrukturberechnungen konnten dieses außergewöhnliche Verhalten als einen gewöhnlichen Effekt der Bandstruktur in diesem System erklären.

An einer Serie von mesoskopischen Strukturen auf nichtmagnetischen und magnetischen Quantentrögen wurden universelle Leitwertfluktuationen untersucht. Im nichtmagnetischen Fall gehorchte die Temperaturabhängigkeit der Standardabweichung des Widerstands, die ein Maß für die Amplitude der Fluktuationen ist, einem Potenzgesetz ($\propto T^{-0.64}$) in guter Übereinstimmung mit der Theorie von Lee *et al.* . In Proben, die 5% Mangan enthielten, konnte diese Übereinstimmung nur im Temperaturbereich über 400 mK gefunden werden. Darüberhinaus wiesen diese Proben eine zusätzliche Fluktuation mit einer Periode von etwa 140 mT und einer Amplitude von 200 Ω auf. Diese Amplitude wächst mit sinkender Temperatur bis 400 mK und verkleinert sich wieder, wenn man die Temperatur weiter absenkt. Eine mögliche Erklärung konnte in einem Phasenübergang von der paramagnetischen (T>400 mK) zur Spinglas Phase (T<400 mK) gefunden werden, die ebenso das Verhalten der Amplitude der universellen Leitwertfluktuationen erklärt. Durch diese Identifikation lässt sich mittels einfacher geometrischer Überlegungen eine charakteristische Größe für Manganhäufungen (1.5×10^{-14} m^2) in dieser Probe geben. Mit diesen Experimenten konnte gezeigt werden, dass das zweidimensionale Elektronengas als Sensor für den magnetischen Ordnungszustand einer Probe verwendet werden kann.

Die vorliegende Arbeit hat neue Methoden und Probenstrukturen eingeführt, die zur Untersuchung von phasenkohärenten und spinabhängigen Transportphänomenen verwendet wurden. Erstmalig wurden neue und bekannte Effekte an quecksilberhaltigen Heterostrukturen beobachet. Wie immer, so auch hier wächst die Zahl der unbeatworteten Fragen schneller als die der beantworteten. Für zukünftige Arbeiten ergeben sich im direkten Anschluss an diese Arbeit neue, spannende Fragen. Mit einer verbesserten Probenstruktur, wie sie im Text vorgeschlagen wird, könnte eine direkte Beobachtung der Spin-Bahn-Berry-Phase möglich sein. Die Methode, ein zweidimensionales Elektronengas als Sensor für den magnetischen Ordnungszustand zu verwenden könnte auf Proben mit unterschiedlichem Mangangehalt angewendet werden um das Phasendiagramm der magnetischen Ordnung zu vervollständigen.

List of Figures

1.1 Landau quantisation in 3D 13
1.2 Comparison of Landau level spacing and broadening 14
1.3 Edge channels in a 2D sample 17
1.4 Sketch to explain LB theory 18
1.5 Sketch of NLR measurement setup and classical rebound trajectories 20
1.6 MC simulation of electron trajectories 21

2.1 Schematic setup of the AB effect 27
2.2 Parallel transport on a sphere 28
2.3 Setup for exploration of the SO Berry phase 30
2.4 Simulation of spin-orbit Berry phase 31

3.1 Band structure of HgTe quantum wells 36
3.2 Electron probability of the $H1$ subband 37
3.3 Energy-band structure of $\mathrm{Hg_{1-x}Mn_xTe}$ 38
3.4 Temperature dependent SdH oscillations on bulk HgMnTe 41
3.5 Temperature dependent node position 43
3.6 Comparison of calculated and measured SdH amplitudes 44
3.7 Zero field spin-orbit splitting 45
3.8 Phase diagram of $\mathrm{Hg_{1-x}Mn_xTe}$ 48
3.9 Superexchange between two magnetic atoms 49

4.1 SEM photograph of a cross shaped structure 55
4.2 Non-local resistance measurement 57
4.3 Non-local resistance measurement 58

4.4 NLR measurement (3 terminal) and Hall measurement 59
4.5 Anomalous Hall effect 59
4.6 MC simulation of electron trajectories 60
4.7 MC simulations of the NLR with different τ 61
4.8 NLR data and MC simulation 62
4.9 Transmission probabilities for differentτ 63
4.10 SEM photograph of a ring shaped structure 64
4.11 Measurement of AB-oscillations 65
4.12 Opt. microscope photograph of a ring with gate on top 66
4.13 Measurement of AC-oscillations 67
4.14 Contour plot of AB oscillations 68
4.15 Contour plot of AB oscillations 69

5.1 Temperature dependent SdH oscillations of a HgMnTe QW 75
5.2 Level splitting energy difference for different T 76
5.3 Gate voltage dependent SdH oscillations of a HgMnTe QW 77
5.4 Population difference of the spin-split $H1$ 77
5.5 Tilted field measurements 78
5.6 Interplay of Rashba, Zeeman and Landau splitting 79
5.7 Bandstructure and QHE measurement on Q1721 82
5.8 Temperature dependent measurement on Q1721 83
5.9 Reproducibility of UCF measurement 85
5.10 Extraction of the UCF signal 86
5.11 Temperature dependent UCF 86
5.12 Amplitude of UCF vs. T 87
5.13 FFT of UCF for various T 88
5.14 Amplitude of FFT peak vs. T 89
5.15 Resistance fluctuations in a 3 μm long, 0.5 μm wide stripe 90
5.16 SdH and QHE in a micro Hall bar 91
5.17 Resistance fluctuations in a micro Hall bar 92
5.18 Amplitude of large resistance fluctuations vs. T 93
5.19 Weak anti-localisation 94
5.20 Extracting UCF 95
5.21 σ(UCF) vs. T 96

Bibliography

[AA81] H. Aoki and T. Ando. Effect of localization on the Hall conductivity in the two-dimensional system in strong magnetic fields. *Sol. State Commun.*, **38**:1079, 1981.

[AA87] Y. Aharonov and J. Anandan. Phase change during a cyclic quantum evolution. *Phys. Rev. Lett.*, **58**:1593–1596, 1987.

[AAR79] P.W. Anderson, E. Abrahams, and T.V. Ramakrishnan. Possible explanation of nonlinear conductivity in thin-film metal wires. *Phys. Rev. Lett.*, **43**:718–720, 1979.

[AB59] Y. Aharonov and D. Bohm. Significance of electromagnetic potentials in the quantum theory. *Phys. Rev.*, **115**:485, 1959.

[AC84] Y. Aharonov and A. Casher. Topological quantum effects for neutral particles. *Phys. Rev. Lett.*, **53**:319–321, 1984.

[AFS82] T. Ando, A.B. Fowler, and F. Stern. Electronic properties of two-dimensional systems. *Rev. Mod. Phys.*, **54**(2):437, 1982.

[AH59] E.N. Adams and T.D. Holstein. Quantum theory of transverse galvanomagnetic phenomena. *J. Phys. Chem. Solids*, **10**:254, 1959.

[ALG93] A.G. Aronov and Y.B. Lyanda-Geller. Spin-Orbit Berry Phase in Conducting Rings. *Phys.Rev.Lett.*, **70**:343–346, 1993.

[AM76] N.W. Ashcroft and N.D. Mermin. *Solid State Physics*. W.B. Saunders Company, 1976.

[Aok77] H. Aoki. Computer simulations of two-dimensional disordered electron systems in strong magnetic fields. *J. Phys. C: Solid State Phys.*, **10**:2583, 1977.

[Aok87] H. Aoki. Quantised Hall Effect. *Rep. Prog. Phys.*, **50**, 1987.

[AS86] B.L. Altshuler and B.Z. Spivak. Variation of the random potential and the conductivity of samples of small dimensions. *JETP Lett.*, **42**:477, 1986.

[Ber83] G. Bergmann. Physical interpretation of weak localization: A time-of-flight experiment with conduction electrons. *Phys. Rev. B*, **28**:2914–2920, 1983.

[Ber84a] G. Bergmann. Weak localization in thin films: a time-of-flight experiment with conduction electrons. *Phys. Rep.*, **107**:1–58, 1984.

[Ber84b] M.V. Berry. Quantal phase factors accompanying adiabatic changes. *Proc. Roy. Soc. London*, **A 392**:45–57, 1984.

[BL80] G. Bastard and C.J. Lewiner. Magnetisation of $\mathrm{Hg_{1-x}Mn_xTe}$ alloys: a self consistent two-spin cluster model. *J. Phys. C*, **13**:1469–1479, 1980.

[BM84] N.B. Brandt and V.V. Moshchalkov. Semimagnetic Semiconductors. *Advances in Physics*, **33**:193–256, 1984.

[BMPN92] A. Benoit, D. Mailly, P. Perrier, and P. Nedellec. Effect of magnetic impurities on universal conductance fluctuations. *Superlattices Microstruct.*, **11**:313–316, 1992.

[BR84] Y. A. Bychkov and E.I. Rashba. Oscillatory effects and the magnetic susceptibility of carriers in inversion layers. *J. Phys. C*, **17**:6039–6045, 1984.

[BRG$^+$81] G. Bastard, C. Rigaux, Y. Guldner, A. Mycielski, J.K. Furdyna, and D.B. Mullin. Interband magnetoabsorbtion in semimagnetic semiconductor alloys $\mathrm{Hg_{1-k}Mn_kTe}$ with a positive energy gap. *Phys. Rev. B*, **24**:1961–1970, 1981.

[Buh04] H. Buhmann. Quantentransport in Nanostrukturen. Vorlesung an der Universität Würzburg, 2004.

[BvH89] C.W.J. Beenakker and H. van Houten. Billiard model of a ballistic multiprobe conductor. *Phys. Rev. Lett.*, **63**:1857–1860, 1989.

[BvH90] C.W.J. Beenakker and H. van Houten. *Electronic Properties of Multilayers and Low-Dimensional Semiconductor Structures*. Plenum, 1990.

[BvH91] C.W.J. Beenakker and H. van Houten. *Quantum Transport in Semiconductor Nanostructures*, volume **44** of *Solid State Physics*. Academic Press, 1991.

[Büt86] M. Büttiker. Four-Terminal Phase-Coherent Conductance. *Phys. Rev. Lett.*, **57**:1761–1764, 1986.

[Büt88] M. Büttiker. Absence of backscattering in the quantum Hall effect in multiprobe conductors. *Phys. Rev. B*, **38**:9375–9389, 1988.

[CBD95] M. Cieplak, B.R. Bulka, and T. Dietl. Magnetoconductance fluctuations in mesoscopic spin glasses. *Phys. Rev. B*, **51**:8939–8945, 1995.

[Cha60] R.G. Chambers. Shift of an electron interference pattern by enclosed magnetic flux. *Phys. Rev. Lett.*, **5**:3, 1960.

[CMN03] D. Culcer, A.H. MacDonald, and Q. Niu. Anomalous Hall effect in paramagnetic two-dimensional systems. *Phys. Rev. B*, **68**:045327, 2003.

[COK$^+$89] A. Cimmino, G.I. Opat, A.G. Klein, S.A. Werner, M. Arif, and R. Clothier. Observation of the topological Aharonov-Casher phase shift by neutron interferometry. *Phys. Rev. Lett.*, **63**:380–383, 1989.

[CYRK97] T. Choi, S. Young, C.-M. Ryu, and C.K. Kim. Quantum transport by nonadiabatic Aharonov-Casher phase in mesoscopic rings. *Phys. Rev. B*, **56**:4825–4829, 1997.

[dAeSlRB97] E.A. de Andrada e Silva, G.C. la Rocca, and F. Bassani. Spin-orbit splitting of electronic states in semiconductor asymmetric quantum wells. *Phys. Rev. B*, **55**:16293–16299, 1997.

[Dat95] S. Datta. *Electronic Transport in Mesoscopic Systems*. Cambridge University Press, 1995.

[Dau99] V. Daumer. Charakterisierung von CdZnTe-Heterostrukturen mit dem Rasterkraftmikroskop zur Optimierung des MBE-Pozesses. Master's thesis, Universität Würzburg, 1999.

[Dav98] J.H. Davies. *The Physics of Low-Dimensional Semiconductors*. Cambridge University Press, 1998.

[DDR90] B. Das, S. Datta, and R. Reifenberger. Zero-field spin splitting in a two-dimensional electron gas. *Phys. Rev. B*, **41**:8278–8287, 1990.

[DGG$^+$03] V. Daumer, I. Golombek, M. Gbordzoe, E.G. Novik, V. Hock, C.R. Becker, H. Buhmann, and L.W. Molenkamp. Quasiballistic transport in HgTe quantum-well nanostructures. *Appl. Phys. Lett.*, **83**:1376–1378, 2003.

[Dre55] G. Dresselhaus. Spin-Orbit Coupling Effects in Zinc Blende Structures. *Phys. Rev.*, **100**:580–586, 1955.

[Dru00a] P. Drude. Zur Elektronentheorie der Metalle; I. Teil. *Ann. d. Phys*, **1**:566, 1900.

[Dru00b] P. Drude. Zur Elektronentheorie der Metalle; II. Teil. *Ann. d. Phys*, **3**:24, 1900.

[dVF93] P.G.N. de Vegvar and T.A. Fulton. Internal Field Distributions of Mesoscopic Spin Glasses. *Phys. Rev. Lett.*, **71**:3537–3540, 1993.

[dVL92] P.G.N. de Vegvar and L. P. Levy. Reply. *Phys. Rev. Lett.*, **68**:3485, 1992.

[dVLF91] P.G.N. de Vegvar, L.P. Levy, and T.A. Fulton. Conductance fluctuations of mesoscopic spin glasses. *Phys. Rev. Lett.*, **66**:2380–2383, 1991.

[EL00] H.-A. Engel and D. Loss. Conductance fluctuations in diffusive rings: Berry phase effects and criteria for adiabacity. *Phys. Rev. B*, **62**:10238–10254, 2000.

[ES49] W. Ehrenberg and R.E. Siday. The refractive index in electron optics and the principle of dynamics. *Proc. Roy. Soc. London*, **B62**:8–21, 1949.

[FBLM87] S. Feng, A.J. Bray, P.A. Lee, and M.A. Moore. Universal conductance fluctuations as a probe of chaotic behavior in mesoscopic spin glasses. *Phys. Rev. B*, **36**:5624–5627, 1987.

[FH65] R.P. Feynman and A.R. Hibbs. *Quantum mechanics and path integral.* McGraw-Hill, 1965.

[FKH$^+$91] P.F. Fontein, J.A. Kleinen, P. Hendriks, F.A.P. Blom, J.H. Wolter, H.G.M. Lochs, F.A.J.M. Driessen, L.J. Giling, and C.W.J. Beenaker. Spatial potential distribution in GaAs/Al$_x$Ga$_{1-x}$As heterostructures under quantum Hall conditions studied with linear electro-optic effect. *Phys. Rev. B*, **43**:12090–12093, 1991.

[Fum76] F.G. Fumi, editor. Proceedings of the 13th International Conference on the Physics of Semiconductors, North-Holland, 1976.

[Fur88] J.K. Furdyna. Diluted magnetic semiconductors. *J. Appl. Phys.*, **64**:R29, 1988.

[GBD$^+$04] Y.S. Gui, C.R. Becker, N. Dai, J. Liu, E.G. Novik, M. Schäfer, X.Z. Shu, J.H. Chu, H. Buhmann, and L.W. Molenkamp. Giant spin-orbit splitting in a HgTe quantum well. *Phys. Rev. B*, **70**:115328, 2004.

[GBL$^+$04] Y.S. Gui, C.R. Becker, J. Liu, V. Daumer, V. Hock, H. Buhmann, and L.W. Molenkamp. Interplay of Rashba, Zeeman and Landau splitting in a magnetic two-dimensional electron gas. *Europhys. Lett.*, **65**:393–399, 2004.

[Ger97] J. Gerschütz. *Magnetotransportuntersuchungen an II-VI-Halbleiter-Heterostrukturen*. PhD thesis, Universität Würzburg, 1997.

[Ger00] R.R. Gerhardts. Private communication, 2000.

[GLD$^+$02] Y.S. Gui, J. Liu, V. Daumer, C.R. Becker, H. Buhmann, and L.W. Molenkamp. Large Rashba spin-orbit splitting in gate controlled n-type modulation doped HgTe/$\mathrm{Hg_{0.3}Cd_{0.7-x}Mn_xTe}$ quantum wells. *Physica E*, **12**:416–419, 2002.

[GLK79] L.P. Gor'kov, A.I. Larkin, and D.E. Khmel'nitski. Particle conductivity in a two-dimensional random potential. *JETP Lett.*, **30**:228, 1979.

[GLO$^+$01] Y.S. Gui, J. Liu, K. Ortner, V. Daumer, C.R. Becker, H. Buhmann, and L.W. Molenkamp. Antiferromagnetic temperature and effective spin in n-type $\mathrm{hg_{1-x}mn_xte}$. *Appl. Phys. Lett.*, **79**:1321–1323, 2001.

[Gru00] D. Grundler. Large Rashba Splitting in InAs Quantum Wells due to Electron Wave Function Penetration into Barrier Layers. *Phys. Rev. Lett.*, **84**:6074–6077, 2000.

[GSW95] A. Görlitz, B. Schuh, and A. Weis. Measurement of the Aharonov-Casher phase of aligned Rb atoms. *Phys. Rev. A*, **51**:4305–4308, 1995.

[HBGM98] A.S.D. Heindrichs, H. Buhmann, S.F. Godijn, and L.W. Molenkamp. Classical rebound trajectories in nonlocal ballistic electron transport. *Phys. Rev. B*, **57**:3961–3965, 1998.

[Hel88] K.-H. Hellwege. *Einführung in die Festkörperphysik*. Springer-Verlag, 1988.

[HLN80] S. Hikami, A.I. Larkin, and Y. Nagaoka. Spin-orbit interaction and magnetoresistance in the two dimensional random system. *Prog. Theor. Phys.*, **63**:707–710, 1980.

[Jai92] J.K. Jain. Microscopic theory of the fractional quantum Hall effect. *Adv. in Phys.*, **41**:105–145, 1992.

[JWK$^+$98] J. Jaroszynski, J. Wrobel, G. Karczewski, T. Wojtowicz, and T. Dietl. Magnetoconductance noise and irreversibilities in submicron wires of spin-glass n^+-$\mathrm{Cd_{1-x}Mn_xTe}$. *Phys. Rev. Lett.*, **80**:5635–5638, 1998.

[JWS$^+$95] J. Jaroszynski, J. Wrobel, M. Sawicki, E. Kaminska, T. Skoskiewicz, G. Karczewski, T. Wojtowicz, A. Potrowska,

J. Kossut, and T. Dietl. Influence of $s-d$ Exchange Interaction on Universal Conductance Fluctuations in $\mathrm{Cd_{1-x}Mn_xTe:In}$. *Phys. Rev. Lett.*, **75**:3170–3173, 1995.

[KAGK81] G.D. Khattak, C.D. Amarasekara, R.R. Galazka, and P.H. Keesom. Specific heat, magnetic susceptibility, and the spin-glass transition in $\mathrm{Hg_{1-x}Mn_xSe}$. *Phys. Rev. B*, **23**:3553–3554, 1981.

[KR03] N. Kawashima and H. Rieger. Recent Progress in Spin Glasses. *arXiv:cond-mat/0312432*, 2003.

[Lan30] L. Landau. Diamagnetismus der Metalle. *Z. Physik*, **64**:629, 1930.

[Lan57] R. Landauer. Spatial Variation of Currents and Fields Due to Localized Scatterers in Metallic Conduction. *IBM J. Res. Dev.*, **1**:223–231, 1957.

[Lan03] G. Landwehr. 25 Years quantum Hall effect: how it came all about. *Physica E*, **20**:1–13, 2003.

[Las85] R. Lassnig. $k \cdot p$ theory, effective-mass approach, and spin splitting for two-dimensional electrons in GaAs-GaAlAs heterostructures. *Phys. Rev. B*, **31**:8076–8086, 1985.

[Lau81] R.B. Laughlin. Quantized Hall conductivity in two dimensions. *Phys. Rev. B*, **23**:5632, 1981.

[Lau83] R.B. Laughlin. Anomalous Quantum Hall Effect: An Incompressible Quantum Fluid with Fractionally Charged Excitations. *Phys. Rev. Lett.*, **50**:1395–1398, 1983.

[LGB90] D. Loss, P. Goldbart, and A.V. Balatsky. Berry's phase and persistent charge and spin currents in textured mesoscopic rings. *Phys. Rev. Lett.*, **65**:1655–1658, 1990.

[LHEC88] B.E. Larson, K.C. Hass, H. Ehrenreich, and A.E. Carlsson. Theory of exchange interactions and chemical trends in diluted magnetic semiconductors. *Phys. Rev. B*, **37**:4137, 1988.

[Liu03] J. Liu. *Magnetotransport in Hg-Based Narrow-Gap Magnetic Semiconductor Structures*. PhD thesis, Universität Würzburg, 2003.

[LS85] P.A. Lee and A.D. Stone. Universal conductace fluctuations in metals. *Phys. Rev. Lett.*, **55**:1622–1625, 1985.

[LSF87] P.A. Lee, A.D. Stone, and H. Fukuyama. Universal conductance fluctuations in metals: effects of finite temperature, interactions, and magnetic field. *Phys. Rev. B*, **35**:1039–1070, 1987.

[Mes69] A. Messiah. *Quantum Mechanics*, volume **1**. North-Holland, 1969.

[Mes70] A. Messiah. *Quantum Mechanics*, volume **2**. North-Holland, 1970.

[MHK+98] A.F. Morpurgo, J.P. Heida, T.M. Klapwijk, B.J. van Wees, and G. Borghs. Ensemble-average spectrum of Aharonov-Bohm conductance oscillations: evidence for spin-orbit-induced Berry's phase. *Phys. Rev. Lett.*, **80**:1050–1053, 1998.

[MPS+84] M. Mezard, G. Parisi, N. Sourlas, G. Toulouse, and M. Virasoro. Nature of the Spin-Glass Phase. *Phys. Rev. Lett.*, **52**:1156–1159, 1984.

[MSB+90] L.W. Molenkamp, A.A.M. Staring, C.W.J. Beenakker, R. Eppenga, C.E. Timmering, J.G. Williamson, C.J.P.M. Harmans, and C.T. Foxon. Electron-beam collimation with a quantum point contact. *Phys. Rev. B*, **41**:1274–1277, 1990.

[Myd93] J.A. Mydosh. *Spin glasses: an experimental introduction*. Taylor & Francis, 1993.

[NKT02] J. Nitta, T. Koga, and H. Takayanagi. Interference of Aharonov-Bohm ring structures affected by spin-orbit interaction. *Physica E*, **12**:753–757, 2002.

[NPJJ+04] E.G. Novik, A. Pfeuffer-Jeschke, T. Jungwirth, V. Latussek, C.R. Becker, H. Buhmann, and L.W. Molenkamp. Band structure of semimagnetic $Hg_{1-y}Mn_yTe$ quantum wells. *arXiv:cond-mat/0409392*, 2004.

[NRGA+80] S. Nagata, D.P. Mullin R.R. Galazka, M. Akbarzadeh, G.D. Khattak, J.K. Furdyna, and P.H. Keesom. Magnetic susceptibility, specific heat, and the spin-glass transition in $\mathrm{Hg_{1-x}Mn_xTe}$. *Phys. Rev. B*, **22**:3331–3343, 1980.

[OU74] F.J. Ohkawa and Y. Uemura. Quantized Surface States of a Narrow-Gap Semiconductor. *J. Phys. Soc. Jpn.*, **37**:1325–1333, 1974.

[Par83] G. Parisi. Order Parameter for Spin-Glasses. *Phys. Rev. Lett.*, **50**:1946–1948, 1983.

[Pfe97] P. Pfeffer. Spin splitting of conduction energies in $\mathrm{GaAs - Ga_{0.7}Al_{0.3}As}$ heterojunctions at B=0 and B≠0 due to inversion asymmetry. *Phys. Rev. B*, **55**:R7359–R7362, 1997.

[PJ00] A. Pfeuffer-Jeschke. *Bandstruktur und Landau-Niveaus quecksilberhaltiger II-VI-Heterostrukturen*. PhD thesis, Universität Würzburg, 2000.

[PZ99] P. Pfeffer and W. Zawadzki. Spin splitting of conduction subbands in III-V heterostructures due to inversion asymmetry. *Phys. Rev. B*, **59**:R5312–R5315, 1999.

[QS94] T.-Z. Qian and Z.-B. Su. Spin-orbit interaction and Aharonov-Anandan phase in mesoscopic rings. *Phys. Rev. Lett.*, **72**:2311–2315, 1994.

[RA66] L.M. Roth and P.N. Argyres. *Magnetic Quantum Effects*, volume **1** of *Semiconductor and Semimetals*. Academic Press, 1966.

[Res00] R. Resta. Manifestations of Berry's phase in molecules and condensed matter. *J. Phys.: Condens. Matter*, **12**:R107–R143, 2000.

[RML89] U. Rössler, F. Malcher, and G. Lommer. Spin-Splitting in Structured Semiconductors. *Springer Series in Solid-State Sciences*, **87**:376–385, 1989.

[RNSF01] A.C.H. Rowe, J. Nehls, R.A. Stradling, and R.S. Ferguson. Origin of beat patterns in the quantum magnetoresistance of gated InAs/GaSb and InAs/AlSb quantum wells. *Phys. Rev. B*, **63**:201307–201310, 2001.

[Sak95] J.J. Sakurai. *Modern quantum mechanics*. Addison-Wesley, 1995.

[See91] K. Seeger. *Semiconductor Physics: An Introduction*, volume **40** of *Springer Series in Solid-State Sciences*. Springer-Verlag, 1991.

[SK75] D. Sherrington and S. Kirkpatric. Solvable Model of a Spin-Glass. *Phys. Rev. Lett.*, **35**:1792, 1975.

[SS91] D.G. Seiler and A.E. Stephens. *The Shubnikov-de Haas effect in semiconductors: A comprehensive review of experimental aspects*, volume **27.2** of *Modern Problems in Condensed Matter Sciences*. North-Holland, 1991.

[SSC$^+$83] H.L. Störmer, Z. Schlesinger, A. Chang, D.C. Tsui, A.C. Gossard, and W. Wiegmann. Energy Structure and Quantized Hall Effect of Two-Dimensional Holes. *Phys. Rev. Lett.*, **51**:126, 1983.

[SvKW83] D. Stein, K. v. Klitzing, and G. Weimann. Electron Spin Resonance on $\mathrm{GaAs} - \mathrm{Al_xGa_{1-x}As}$ Heterostructures. *Phys. Rev. Lett.*, **51**:130, 1983.

[Tim92] G. Timp. *When Does a Wire Become an Electron Waveguide*, volume **35** of *Semiconductor and Semimetals*. Academic Press, London, 1992.

[TSG82] D.C. Tsui, H.L. Störmer, and A.C. Gossard. Two-Dimensional Magnetotransport in the Extreme Quantum Limit. *Phys. Rev. Lett.*, **48**:1559, 1982.

[vKDP80] K. v. Klitzing, G. Dorda, and M. Pepper. New Method for High-Accuracy Determination of the Fine Structure Constant Based on Quantized Hall Resistance. *Phys. Rev. Lett.*, **45**:494, 1980.

[Wei92] M.B. Weissman. Comment on "Conductance Fluctuations of Mesoscopic Spin Glasses". *Phys. Rev. Lett.*, **68**:3484, 1992.

[Win00] R. Winkler. Rashba spin splitting in two-dimensional electron and hole systems. *Phys. Rev. B*, **62**:4245–4248, 2000.

[Win03] R. Winkler. *Spin Orbit Coupling Effects in Two-Dimensional Electron and Hole Systems*. Springer, Berlin, Heidelberg, 2003.

[WR93] R. Winkler and U. Rössler. General approach to the envelope-function approximation base on a quadrature method. *Phys. Rev. B*, **48**:8918–8927, 1993.

[YPS02] J.-B. Yau, E.P. Poortere, and M. Shayegan. Aharonov-Bohm oscillations with spin: Evidence for Berry's phase. *Phys. Rev. Lett.*, **88**, 2002.

[Zha01] X. Zhang. *Magnetotransport investigations of type III HgTe/HgCdTe single quantum wells*. PhD thesis, Universität Würzburg, 2001.

[ZOPJ$^+$04] X.C. Zhang, K. Ortner, A. Pfeuffer-Jeschke, C.R. Becker, and G. Landwehr. Effective g factor in $\mathrm{HgTe/Hg_{1-x}Cd_xTe}$ single quantum wells. *Phys. Rev. B.*, **69**:115340, 2004.

[ZPJO$^+$01] X.C. Zhang, A. Pfeuffer-Jeschke, K. Ortner, V. Hock, H. Buhmann, C.R. Becker, and G. Landwehr. Rashba splitting in n-type modulation doped HgTe quantum wells with an inverted band structure. *Phys. Rev. B*, **63**:245305, 2001.

[ZPJO$^+$02] X.C. Zhang, A. Pfeuffer-Jeschke, K. Ortner, C.R. Becker, and G. Landwehr. Absence of magneto-intersubband scattering in n-type HgTe quantum wells. *Phys. Rev. B*, **65**:045324, 2002.

[ZZRH95] K. Zeiske, G. Zinner, F. Riehle, and J. Helmcke. Atom interferometry in a static electric field: measurement of the Aharonov-Casher phase. *Appl. Phys. B*, **60**:205–209, 1995.

List of Publications

C.R. Becker, A. Pfeuffer-Jeschke, V. Latussek, M. Li, K. Ortner, V. Daumer, S. Oehling, W. Tang, and G. Landwehr. Growth and optical properties of (112)B HgTe/$Hg_{1-x}Cd_xTe$ superlattices. *J. Cryst. Growth*, **185**:1185-1189, 1998.

Y.S. Gui, J. Liu, K. Ortner, V. Daumer, C.R. Becker, H. Buhmann, and L.W. Molenkamp. Antiferromagnetic temperature and effective spin in *n*-type $Hg_{1-x}Mn_xTe$. *Appl. Phys. Lett.*, **79**:1321-1323, 2001.

C.R. Becker, Y.S. Gui, J. Liu, V. Daumer, K. Ortner, V. Hock, A. Pfeuffer-Jeschke, H. Buhmann, and L.W. Molenkamp. Growth and magneto-transport of gate controlled *n*-type HgTe/$Hg_{0.3}Cd_{0.7}Te$ quantum wells with the inclusion of Mn. *phys. stat. sol. (b)*, **229**(2):775-779, 2002.

Y.S. Gui, J. Liu, V. Daumer, C.R. Becker, H. Buhmann, and L.W. Molenkamp. Large Rashba spin-orbit splitting in gate controlled *n*-type modulation doped HgTe/$Hg_{0.3}Cd_{0.7-x}Mn_xTe$ quantum wells. *Physica E*, **12**:416-419, 2002.

C.R. Becker, X.C. Zhang, K. Ortner, J. Schmidt, A. Pfeuffer-Jeschke, V. Latussek, Y.S. Gui, V. Daumer, J. Liu, H. Buhmann, G. Landwehr and L.W. Molenkamp. MBE growth and characterization of Hg based compounds and heterostructures. *Thin solid films*, **412** (1-2):129-138, 2002.

J. Liu, V. Daumer, Y.S. Gui, V. Hock, C.R. Becker, H. Buhmann, and L.W. Molenkamp. Competition between Rashba effect and exchange interaction in a $Hg_{0.98}Mn_{0.02}Te$ magnetic 2DEG. *J. Supercond.*, **16** (2):365-368, 2003.

V. Daumer, I. Golombek, M. Gbordzoe, E.G. Novik, V. Hock, C.R. Becker, H. Buhmann, and L.W. Molenkamp. Quasiballistic transport in HgTe quantum-well nanostructures. *Appl. Phys. Lett.*, **83**:1376-1378, 2003.

C.R. Becker, K. Ortner, X.C. Zhang, A. Pfeuffer-Jeschke, V. Latussek, Y.S. Gui, V. Daumer, H. Buhmann, G. Landwehr and L.W. Molenkamp. Growth and studies of $Hg_{1-x}Cd_xTe$ based low dimensional structures. *Physica E*, **20**:436-443, 2004.

Y.S. Gui, C.R. Becker, J. Liu, V. Daumer, V. Hock, H. Buhmann, and L.W. Molenkamp. Interplay of Rashba, Zeeman and Landau splitting in a magnetic two-dimensional electron gas. *Europhys. Lett.*, **65**:393-399, 2004.

C.R. Becker, X.C. Zhang, K. Ortner, A. Pfeuffer-Jeschke, V. Latussek, V. Daumer, G. Landwehr and L.W. Molenkamp. MBE growth and characterization of HgTe based quantum wells and superlattices. *J. Alloy Compd.*, **371**:6-9, 2004.

Y.S. Gui, C.R. Becker, J. Liu, M. König, V. Daumer, M.N. Kiselev, H. Buhmann, and L.W. Molenkamp. Current heating of a magnetic two-dimensional electron gas in $\mathrm{Hg_{1-x}Mn_xTe/Hg_{0.3}Cd_{0.7}Te}$ quantum wells. *Phys. Rev. B*, **70**:195328, 2004.

H. Buhmann, E.G. Novik, V. Daumer, J. Liu, Y.S. Gui, C.R. Becker, and L.W. Molenkamp. Odd filling factor quantum Hall sequence in magnetic type-III quantum wells. *Appl. Phys. Lett.*, **86**:212104, 2005.

Acknowledgements

Obtaining scientific results such as those presented in this thesis, can not be the work of one isolated person. Many people made specific contribution to the success of this work.

A prerequisite for this thesis was the offer of PD Dr. Hartmut Buhmann to work in his quantum transport group. I wish to thank him, not only for this possibility but also for his personal encouragement during the progress of this work. With his presence in the laboratory and together with his group in the beergarden he formed a good collaborating team. Also unforgettable were the night shifts at the GHMFL which were spent together.

The basis for such experiments is an well equipped laboratory. Hence, many thanks go to Prof. Dr. Gottfried Landwehr and Prof. Dr. Laurens W. Molenkamp who succeeded to provide almost unique possibilities for a rapid realisation of new scientific ideas beginning with crystal growth through lithographic patterning up to low temperature, high magnetic field characterisation. Furthermore I am indebted to them for their scientific interest and suggestions, as well as for many fruitful discussions with them.

It was a great pleasure to work and discuss with the colleagues of the quantum transport group. With this good team the day-by-day challenges were solved quickly and successfully. Furthermore I gratefully acknowledge the numerous fruitful discussions and the scientific exchange.

Sharing a room with Dr. Charles R. Becker resulted in a successful friendship. His experience in epitaxial crystal growth and the band structure specific to Hg based heterostructures were very important for the progress of this work. Also many thanks for critically reading this thesis.

In particular the development of nanostructures would not have been possible without the help of Volkmar Hock. With his patience, endurance and many hours in the yellow room we finally overcame the technological problems with this material.

Many thanks go to Anita Gebhardt and Petra Wolf-Müller for their assistance in the MBE laboratory. With their perfect sample preparation they made good epitaxial growth possible.

Essentially for all mechanical problems, modifying sample holders, repairing and building up new cryostats, supporting in low temperature and vacuum technology problems were Roland Ebert and Alfred Schönteich. Many thanks to them.

Thanks also for the supply of liquid Helium to Gerd, we have always enough LHe for everyone, Manger.

I would like to thank the good spirit of the chair, Anja Brück-Poirer. With her good organisation, the administrative stuff was easy to solve.

During my time in the EP3 chair I met new friends. Spending my free time with Armin Bader and Claus Schumacher involving several activities gave me the strength to carry on even in the case of setbacks. Unfortunately Armin died unexpectedly two years ago. But he is still on my mind.

Thanks for the recreative lunch breaks to the mensa/coffee group. I will miss the amusing talks.

Finally I have to thank all the present and former members of EP3, who are not mentioned here by name. If I would try to write down every specific situation, this would fill another book. Thank you all!

Last but not least the background of my family must be acknowledged. Their support during my entire live and personal development was essentially to bring me to this point of my life.